University of Bath

PHD

Pyroelectric Structures and Devices for Thermal Energy Harvesting

Zabek, Daniel Adam

Award date:
2016

Awarding institution:
University of Bath

Link to publication

Alternative formats
If you require this document in an alternative format, please contact:
openaccess@bath.ac.uk

Copyright of this thesis rests with the author. Access is subject to the above licence, if given. If no licence is specified above, original content in this thesis is licensed under the terms of the Creative Commons Attribution-NonCommercial 4.0 International (CC BY-NC-ND 4.0) Licence (https://creativecommons.org/licenses/by-nc-nd/4.0/). Any third-party copyright material present remains the property of its respective owner(s) and is licensed under its existing terms.

Take down policy
If you consider content within Bath's Research Portal to be in breach of UK law, please contact: openaccess@bath.ac.uk with the details. Your claim will be investigated and, where appropriate, the item will be removed from public view as soon as possible.

Download date: 05. May. 2023

Pyroelectric Structures and Devices for Thermal Energy Harvesting

Daniel Adam Zabek

Department of Mechanical Engineering
University of Bath

This dissertation is submitted for the degree of
Doctor of Philosophy

Bath October 2016

I would like to dedicate this thesis to my loving family.

Declaration

I hereby declare that except where specific reference is made to the work of others, the contents of this dissertation are original and have not been submitted in whole or in part for consideration for any other degree or qualification in this, or any other university. This dissertation is my own work and contains nothing which is the outcome of work done in collaboration with others, except as specified in the text and acknowledgements. This dissertation contains over 40,000 words including appendices, references, tables and equations.

Daniel Adam Zabek
October 2016

Acknowledgements

This project started by emailing Prof. Chris Bowen with regards to the NEMESIS advanced fellowship on transforming mechanical vibrations and thermal fluctuations into electrical energy. To make a long story short, I sincerely thank Chris for the best time of my life and for the outstanding guidance he provided and the scientific progress we made.

Most importantly, I thank my colleagues Dr. Emmanuel Le Boulbar for strengthening my scientific confidence and communication skills and Dr. Vincent Ayel for providing access to his lab at the Pprime institute CNRS - ENSMA in Potiers (France). I also thank Prof. Sidney Lang for being so encouraging about my work and to all the technicians who were invaluable during my research, especially Dr. Stephen W., Dr. Siva S., Claire and Matthew B., Vijay R., Colin B., Steve C., and Dr. John M. Finally, I thank Vana, Mike, Tony, Peter, Nick, Andrew, James, Kate, Marcin, David and Mengying for making it extremely enjoyable to work at Bath.

Lastly, I would like to acknowledge the European Research Council (ERC) under the European Union's Seventh Framework Programme (FP/2007–2013)/Grant Agreement no. 320963 on Novel Energy Materials, Engineering Science and Integrated Systems (NEMESIS) for funding this research entirely and the support from the Engineering, Physical Science Research Council (EPSRC) under grant number EP/K040324/1 for the use of the Heidelberg μP101 laser writer.

Abstract

Our daily infrastructure, safety, health and comfort relies on a continuous availability of electricity. Due to the volatile nature of electricity and the limited ability of storing electrical energy, it is challenging to implement changes and improve energy efficiency, conversion effectiveness and generator size and weight. In this regard, a wide range of sufficiently high, but currently unused, energy sources are available. Harvesting unexplored waste heat or abundantly available thermal energy sources such as industrial, solar, and geothermal waste heat and abundantly available heat from friction or the human body enables local powering of electronic device, extension of battery lifetime, and even provides accumulated base load power supplies, resulting in the recovery of otherwise unused thermal energy. For this reason, solid-state thermal to electrical energy conversion utilising the pyroelectric effect provides a convenient and direct way of converting temperature fluctuations into an electrical potential difference available for discharge.

In this thesis, the nature and the principles of pyroelectric energy harvesting are presented in a complete review of materials, structures and devices for thermal energy harvesting applications, followed by a detailed experimental set-up providing reproducible experimental results under constant laboratory test conditions. Introducing contactless and harmonic temperature oscillations using a radiative heating lamp allows examination of energy harvesting devices and helps to develop an geometrical optimisation approach.

For radiative heating, a meshed micro- size electrode structure on polyvinylidene difluoride (PVDF) improves the pyroelectric conversion efficiency. The here presented photolithographic manufacturing technique on a flexible substrate provides new device architectures resulting in a 1050 % higher energy trade off. Further electrode modifications involve a graphene-ink based black body radiation absorber on flexible PVDF. With graphene-ink, a laminate structure introduces piezoelectric activity in response to the change in temperature.

The inherent need of temperature oscillations for pyroelectric energy harvesting requires an alternating heat flow. By linking the subject fields of heat transfer in oscillating heat pipes (OHPs) for high performance cooling, together with a pyroelectric energy harvesting device, the experimental system exploits a heat induced liquid-vapour transition of a working fluid as a primary driver for a pyroelectric generator.

Table of contents

List of figures

List of tables

Nomenclature

Roman symbols

A	$[m^2]$	Area
Bo	$[-]$	Bond number
C	$[F]$	Capacitance
C_{ijk}	$[Nm^{-2}]$	Mechanical elasticity
c	$[ms^{-1}]$	Speed of light
c_E	$[Jm^{-3}K^{-1}]$	Volumetric heat capacity
c_p	$[Jg^{-1}K^{-1}]$	Mass heat capacity
D_{ij}	$[Cm^{-2}]$	Electric displacement
D_{piezo}	$[m]$	Piezoelectric displacement
D_n	$[m]$	Diameter
d	$[m]$	Thickness
d_{piezo}	$[CN^{-1}]$	Piezoelectric charge coefficient
E	$[Vm^{-1}]$	Electric field strength
E_c	$[Vm^{-1}]$	Coercive electric field
$E_{electric}$	$[gm^2s^{-2}]$	Electric energy
e	$[\Delta LL^{-1}]$	Strain
e_{ijk}	$[CN^{-1}]$	Piezoelectric charge coefficient
FOM	$[-]$	Figure of merit
FOM_I	$[-]$	Current figure of merit
FOM_V	$[-]$	Voltage figure of merit
f	$[Hz]$	Frequency
g	$[ms^{-2}]$	Gravitational acceleration
h	$[Wm^{-2}K^{-1}]$	Surface conduction coefficient
h_c	$[Js]$	Planck's constant
I	$[A]$	Electric current

k	$[Wm^{-1}K^{-1}]$	Thermal conductivity
k^2	$[-]$	Electromechanical coupling coefficient
k_{33}	$[-]$	Coupling coefficient
k_B	$[Js^{-1}m^{-2}K^{-4}]$	Bolzmann constant
m	$[g]$	Mass
n	$[-]$	Number
P	$[Cm^{-2}]$	Polarisation
$P_{electric}$	$[W]$	Electric power
P_s	$[Cm^{-2}]$	Remnant polarisation
$p*$	$[Cm^{-2}K^{-1}]$	Pyroelectric charge coefficient
Q	$[J]$	Energy
q	$[Wm^{-3}]$	Heat flow through a solid
S	$[JK^{-1}g^{-1}]$	Entropy
T	$[K]$	Temperature
T_{Curie}	$[K]$	Curie temperature
t	$[sec.]$	Time
U	$[gm^{-1}s^{-2}]$	Spectral energy density
V	$[V]$	Voltage
W	$[W]$	Heat flow
x	$[m]$	Distance
Z	$[Ohm]$	Impedance

Greek symbols

α	$[m^2 s^{-1}]$	Diffusivity
α_V	$[\Delta L L^{-1}]$	Thermal expansion coefficient
ε	$[F m^{-1}]$	Effective permittivity
ε_0	$[F m^{-1}]$	Vacuum permittivity
ε_r	$[-]$	Relative permittivity
η	$[-]$	Efficiency
λ	$[m]$	Wavelength
ρ	$[g m^{-3}]$	Density
τ	$[N m^{-1}]$	Surface tension
σ	$[N m^{-2}]$	Mechanical stress
Ω	$[Ohm]$	Resistance

Chapter 1

Introduction

Despite differences in economies and the development of countries, the nature and the side effects of primary energy sources in combination with the unequal geological distribution of fossil fuels affects everybody's life. The European Commission (28 countries) together with the General Assembly of the International Renewable Energy Agency (IRENA) representing 144 States, are pursuing a technically feasible and economic viable transition into sustainable energy with a global annual investment of USD 900 billion per year by 2030 [1]. This enormous market will be dominated by all aspects of renewable energy such as energy-generation, transformation, transportation, and storage. Today, conventional chemical fuels account for 44% of heat and electric power and are the source of the majority of environmental issues [2]. At the same time, the volatile nature of heat and electricity and the limited ability of storage make it the most challenging sector to implements changes. One way towards a decarbonisation of the energy consumption and towards potentially free electric energy is the recovery of unused, or currently wasted, heat. The recovery of low grade heat or waste heat in order to reduced the primary energy source consumption is the driving force of this work aiming for a novel, sustainable and renewable thermal to electrical energy conversion technology. A possible way to harvesting widely available industrial, solar, and geothermal waste heat as well as abundantly available heat from friction or the human body is to utilise the pyroelectric effect. This effect was discovered over 24 centuries ago and allows solid pyroelectric materials to directly convert thermal energy into electrical energy [3]. This work follows a practical approach of transforming low temperature heat directly into electricity with pyroelectric materials, demonstrating the capability of this technology. Energy conversion measurements for different pyroelectric materials are presented in Chapter 3, mapping a wide range of materials and the effectiveness of this technology with respect to various generator applications. Since low temperature heat at elevated temperatures is the driving force of the energy conversion, Chapter 4 presents a heat

transfer enhancement by the introduction of a micro-sized electrode structures. The complex study of this multiphysics phenomenon is supported by conducting a numerical finite element analysis in Chapter 5, revealing an inherent interaction between material dimensions and properties and presenting the benefits for pyroelectric energy harvesting. After successfully demonstrating the enhanced performance of the energy conversion with micro-structured pyroelectric devices, a comparative study for meshed electrodes and graphene-ink electrodes is completed by harvesting thermal energy with pyroelectrics in Chapter 6. Addressing the transient nature of pyroelectric energy generation, a self-sustaining generator without mechanical motion in the form of a combined pyroelectric - oscillating heat pipe assembly is presented in Chapter 7. While the emphasis in this thesis is very much on the applied research, fundamental conclusions are drawn for a better understanding of the nature of the problem. Finally, this work provides an outlook for the pyrolelectric - oscillating heat pipes devices for the conversion of small quantities of thermal energy into more desirable electricity in the nW to mW range and provides an alternative to currently used batteries or centralised energy generation.

Build almost exclusively on three peer reviewed journal articles and two conference proceedings, this work also contributed to three co-authored peer reviewed journal articles. Sections of the presented work are protected by an international patent application GB1603373. The author's complete list of communications is presented in Appendix A.

Chapter 2

Pyroelectric energy harvesting

2.1 Introduction

Chapter 2 reviews the need for energy harvesting technologies and compares unexplored ambient energy sources available for energy harvesting with ferroelectric materials. Utilising the pyroelectric effect for thermal to electrical energy conversion, this chapter derives the fundamentals of pyroelectricity with an emphasis on optimisation and critical design parameters for effective pyroelectric energy harvesting systems. The most attractive material identified for pyroelectric energy harvester applications on a device level is considered to be polyviniludene-difluoride (PVDF), due to the unique properties of flexibility, high performance and low cost.

2.2 Waste heat recovery and energy harvesting

According to the United Nations (UN), the estimated number of people living on the planet will exceed 10 billion by 2060. Consequently, this constant growth in population is followed by an increasing demand in electrical energy, since our health, safety, and comfort relies on a continuous generation and distribution of electric power. On a large scale, changes towards a decentralised generation (distributive generation) are made with modular and flexible energy generators constantly adjusting to the demand, which leads to a large number of units of equipment and infrastructure being installed. However, scaling issues lead to limitations of small scale energy generation promoting the use of chemical, mechanical and electrical energy storage in batteries, flywheels or hydrogen, which are currently the only industrially available solutions. In addition, the nature of the energy consumption has changed, since it continues to rise along with the increasing number of interconnected electronic device (eg.

internet of the things sensors, sensor networks, antennas, active control devices), hand-held devices (eg. phones, tablets, watches) or medical devices (eg. pacemakers, hearing aids, drug-delivery). Technology business estimates expect this market to grow from USD 0.7 billion in 2012 to USD 5 billion by 2020, with additional 250 million new sensors devices in operation [4]; this leads to an increased demand for electricity. In a broader context, solutions for accessible, affordable and reliable electrical energy need to be found to enable the production of battery independent autonomous devices and self-sustaining device operation. Therefore, alternatives need to be found for the current centralised energy generation in form of small scale energy generators supplying power in the range of nW to mW, capable of converting small quantities of energy into more desirable electricity. Certainly, very small power supplies are not going to power the world's energy demand, but are capable of supplying the increasing number of modern CMOS electronic devices replacing mechanical or electric technologies currently used.

At the same time, a vast number of different energy sources are being wasted. Waste energy, if it can be capture or harvested, is energy which is currently unused and available for co-generation or energy scavenging in order to be locally transformed into electricity and made available for discharge [5]. Different types of unexplored waste energy sources, or unexplored ambient energy sources include mechanical, thermal, or radiation sources in the near infra red (IR) as well as the radio frequency (RF) range, and biochemical sources [6]. When harvested, this wide array of sources has the potential to decrease our energy consumption, improve energy availability and reduce operational costs. With respect to the fundamental law of energy conservation, the low conversion efficiency of the potential energy sources above is a limiting factor when recovering waste energy. In this regard, a wide range of sufficiently high, but currently unused energy sources is unexplored, which can be converted into electrical energy and locally power electronic devices, extend battery life, or even provide accumulated base load power supplies. Utilising this approach allows the recovery of otherwise unused energy where needed. Taking the long term view, this approach will lead to clean, green and sustainable energy. With the accumulated power, it is then possible to replace existing energy transformation and transportation infrastructure, avoid energy storage and reduce peak load demand on a large scale, which will eventually lead to a significant economic benefit [7]. However, in the field of waste energy recovery and energy harvesting the focus is currently set on the effectiveness rather than on the economic benefit of a system, since most waste energy sources are considered free. Therefore, sources with a high specific energy density, defined by the available energy per unit area or unit volume, need to be identified.

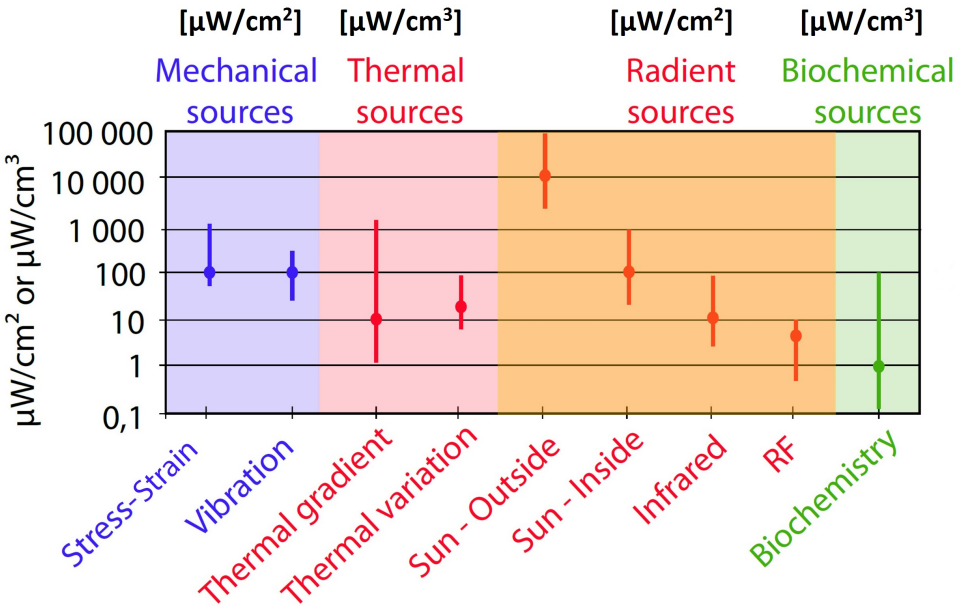

Fig. 2.1 Available ambient energy source for waste energy recovery and energy harvesting when using pyroelectric and ferroelectric materials [6].

According to Figure 2.1 [6], the available ambient mechanical sources such as stress and strain (eg. airflow) as well as ambient mechanical vibrations (eg. ocean waves, construction environment) provide kinetic energy for mechanical waste energy recovery or energy harvesting. Employing the principle of electromagnetic induction [8], or the piezoelectric effect [9], for energy harvesting, abundantly available mechanical energy sources can be utilised and converted into electricity [10]. In contrast, triboelectric generators harvest surface charge from surface friction between two dissimilar materials, indirectly utilising kinetic energy [11]. Other technologies such as electrostatic systems, changing the electrostatic force by mechanical motion, have a significant drawback in terms of synchronising the mechanical and electrical energy flows [12]. With an average mechanical energy density of over 100 $\mu W cm^{-2}$, the recovery of stress and strain energy or vibration energy is sufficiently high in order to power μW electrical energy consumers, when the generator is designed large enough.

Ambient thermal energy sources provide heat as potential energy, since heat travels from hot to cold regions. With the natural environment providing solid (eg. ground heat), liquid (eg. hot springs) and gaseous (eg. airflow) heat sources, the spatial temperature gradient can be utilised for thermal to electrical energy conversion. Thermoelectric generators (TEG) based on the Seebeck effect, where electrons carry heat between two reservoirs, provide a

continuous electric energy supply [13]. A different route for heat recovery from a thermal gradient is the transformation of heat into mechanical energy in order to transform mechanical into electrical energy [14]. Temperature sensitive memory-alloys (ferro-magnetic shape memory or a thermo-mechanical phase transition) coupled with electromagnetic induction or piezoelectrics have been employed to recover heat from comparably small temperature differences [15]. However, apart from relatively rare geothermal sources, most natural temperature gradients are small and difficult to recover, with average energy densities of approximately 10 $\mu W cm^{-2}$.

In contrast, thermal variations (eg. day-night temperature changes) can be harvested and converted into electricity. Alternating changes in temperature due to a change in heat flow can be absorbed by a parafin-wax phase change material. When heated, the volumetric expansion is transformed into mechanical motion energy, available for mechanical to electricity energy conversion [16]. The relatively narrow operation range of this technology makes it suitable for thermal energy harvesting from small temperature fluctuations at low temperatures. Solid state energy conversion from temperature oscillations can also be realised using pyroelectric materials. Pyroelectric materials produce electricity from temperature fluctuations, which is a direct analogy to the way in which piezoelectric systems operate [17]. However, despite the nominal higher energy density compared to thermal ambient gradients, the frequencies of thermal variations are slow and require faster thermal cycling.

With an energy density of nearly 1 kWm^{-2} (Figure 2.1), solar radiation is the most powerful and freely available energy source. Multiple breakthroughs in photovoltaic cells have led to low cost and highly efficient devices [18]. In particular ferroelectric materials for solar cells, a subclass for pyro- and piezo-electric materials, have experienced rapid progress in terms of cost and performance improvements [19]. On the other hand, the wide spectrum of electromagnetic solar radiation around the near IR wavelength can be utilised for many other types of thermal energy converter when transformed into a thermal gradient or converted into temperature fluctuations. If we consider electromagnetic wave sources higher up the electromagnetic wavelength spectrum, ambient electromagnetic waves at the RF or even low energy THz wave lengths can also be converted into electricity [20]. In the field of wireless power transmission, RF induction suffers from low energy densities between 0.1 – 100 $\mu W cm^{-2}$ when harvesting ambient sources, which makes it difficult to recover meaningful power [21]. Compared to well established RF energy transmission, the field of bio-self powered devices that harvest waste chemical energy from ambient chemical potentials is fairly new. Oxygen sensitive enzyme fuel cells can generate an electrical potential difference available for discharge [22]. In addition, by oxygen treatment, so far unexplored for energy harvesting, is the effect of ferroelectric switching induced by

biochemical sources [23]. However, ambient biochemical sources account for the smallest available energy density, as can be seen in Figure 2.1.

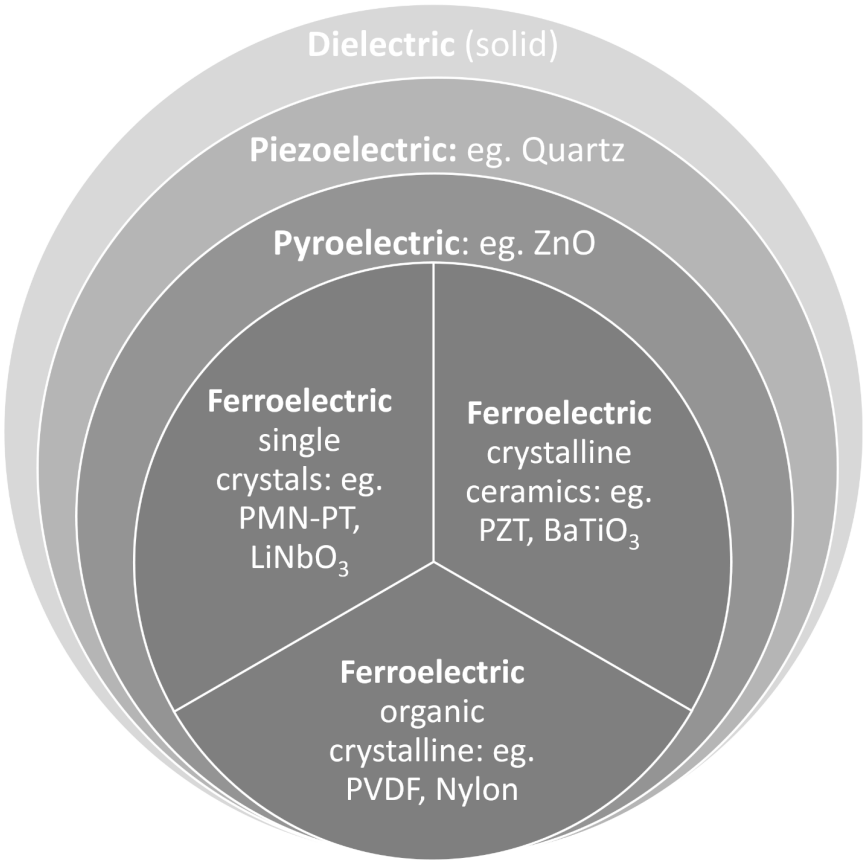

Fig. 2.2 Ferroelectric materials as a subgroup of pyro-, piezo- and dielectric-materials.

Since the different ambient energy source densities vary as much as the different energy harvesting technologies, there is a need for coherence in an approach. One technology capable of recovering mechanical, thermal, radiation and bio-chemical sources, and therefore capturing most of the available ambient sources, is the utilisation of ferroelectric materials. Mechanical vibration can be harvested with ferroelectrics, since all ferroelectrics materials are also piezoelectric [24]. Thermal fluctuations can also be harvested with ferroelectrics, since all ferroelectric are also pyroelectric [25]. Ferroelectric solar cells, harvesting solar radiation, are the most advanced energy harvesting technology in terms of power. Photochemical activity (ferroelectric switching by photochemical effects) with certain ferroelectrics can be used to harvested other specific radiation wavelengths [26]. As a subgroup of solid dielectric materials, Figure 2.2 presents different ferroelectric materials for energy harvesting, capable of harvesting a number of ambient energy sources. The co-existence of ferroelectricity and magnetism in ferroic materials (exhibiting ferroelectric, ferromagnetic and ferroelastic

behaviour) makes it a fascinating material class to study which is crucial from a theoretical as well as technological progress [27]. With over 100 characterised ferroelectric materials available, potentially another 1000 undiscovered materials exhibit ferroelectric behaviour. In particular, the non-volatile and reversible nature of ferroeletrics is capable of converting various energy sources into electricity using only one type of material.

2.3 Pyroelectric effect

In modern science it was not until the invention of the potentiometer capable of measuring voltage, where Vallasek observed high pyroelectric activity in Rochelle Salt in 1920 [3]. Pyro (Greek: 'fire') -electric materials, which are also termed electro-active polar dielectric materials or non-center symmetric dielectric materials, experience a temperature dependent change in spontaneous polarisation P_s, or remnant polarisation, which appears below the material's Curie Temperature (T_c) [28]. On a macroscopic level, this change in spontaneous polarisation, dP_s, due to a change in temperature, dT, is followed by an electric response [29]. When heated uniformly under constant stress (σ), there is a linear relationship between an electric field E and the bulk induced change in polarisation P_{ij} in a solid dielectric volume. Since all pyroelectric materials belong to a non-centersymmetric crystal lattice systems (hexagonal, tetragonal, rhombohedral, orthorhombic, monoclinic or triclinic), crystal symmetry is assumed where the positive electric displacement vector D_{ij} points from a negative to a positive charge. With the corresponding external electrical field E_{ij} applied, the displacement vector sum is defined as [30]:

$$D_{ij} = \varepsilon.E_{ij} + (P_{ij} + Ps_{ij}) \tag{2.1}$$

employing the materials effective electrical permittivity $\varepsilon = \varepsilon_0.\varepsilon_r$, ε_r = relative permittivity and the permittivity of free space ε_0 =8.85 $10^{-12} Fm^{-1}$. The magnitude and orientation of the temperature sensitive polarity Ps_{ij} depends on the thermal and electrical polarisation history. When externally poled, the orientation is defined by the applied electrical field E_{ij}. The temperature induced changes in remnant polarisation Ps_{ij} are defined by the pyroelectric charge coefficient as a one dimensional vector field $p*$:

$$\frac{dPs_{ij}}{dT} = \frac{dPs_{ij}}{dT} dT = p*.dT \tag{2.2}$$

As a subgroup of piezoelectric materials, all pyroelectric materials are also piezoelectric, experiencing a change in dPs_{ij} when exposed to mechanical stress (σ) and strain (e) or due to non-uniform heating changes in thermal expansion, which affect the spontaneous

polarisation moment specified as primary effect $p*$ (equation 2.2) and secondary contribution $(d_{ij}.c_{ijk}.\alpha_i)$ [31]:

$$\frac{dPs_{ij}}{dT} = (p* + d_{ij}.c_{ijk}.\alpha_i)dT \tag{2.3}$$

normal to the polar axis, taking into account the materials piezoelectric coefficient d_{ij}, the elastic stiffness c_{ijk} and the thermal expansion α_i. On a macroscopic level, the reversible

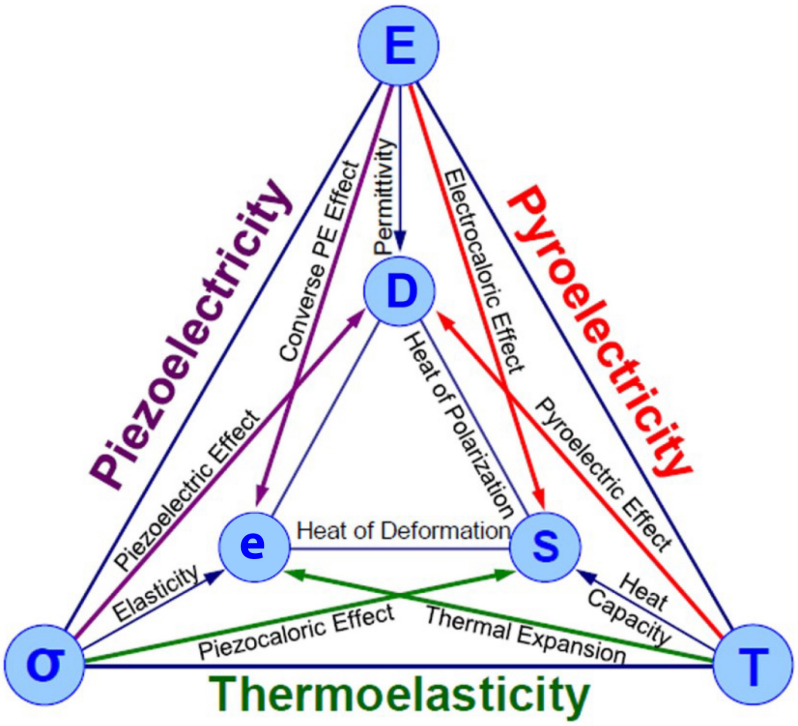

Fig. 2.3 Thermal (T), electrical (E), and mechanical (σ) energy states of a crystal for the corresponding energy conversion fundamentals electric displacement (D), entropy (S) and strain (e) [30].

thermodynamic energy exchanged between thermal (T), mechanical (σ) and electrical (E) energy from equation 2.1, 2.2, and 2.3 is presented in Figure 2.3.

The outer triangle in Figure 2.3 [30] shows that the energy exchange between energy states T, σ, and E is based on the constitutive effects of entropy (S), strain (e) and electric displacement (D). Consequently, the energetic equilibrium of the material is achieved through the inner triangle, where one form of energy (T, σ, and E) cannot be directly converted into the other. Following the path of pyroelectricty in Figure 2.3, the direct pyroelectric effect affects the electric displacement vector D inducing an electric potential difference E. The converse pyroelectric effect, also termed the electro-caloric effect, initiates a reverse electrical-thermal behaviour showing a change in temperature in response to a change in applied electric

field. Therefore, the pyroelectric effect can be treated individually under certain boundary conditions but is usually a combination of the piezo- and the pyro-electric activity in a crystal, due to the thermal expansion when heated [30]. Most importantly, Figure 2.3 shows that the transport properties of thermal (heat capacity) and electrical (permittivity) conductivity and mechanical compliance (elasticity) are important in determining whether it is possible to exchange one form of energy directly into another. Since piezo-, pyro- and ferro-electric materials are frequently used for piezoelectric actuators [32], pyroelectric sensors [33] and non-volatile memories [34], a detailed analysis of crystal physics has been conducted by Nye (1984) [30] and Lang (1974) [31]. Following the in depth analysis, the coupled piezoelectric contribution in the pyroelectric effect usually accounts for 1 % of the total change in polarisation.

Since most pyroelectric materials used for pyroelectric energy harvesting also exhibit ferroelectric behaviour, the polarisation orientation (P_{ij}) is reversible when an external electric field E is applied. According to Figure 2.4, this ferroelectric switching behaviour can be experimentally analysed in order to determine the level of remnant polarisation (here: $P_s = 6.78 \mu C m^{-2}$) and the required coercive electric field (here: $E_c = 776 kV m^{-1}$) for an externally applied electric field with ferroelectric polyvinylidende-difluoride (PVDF) forming a $P-E$ hysteresis loop. This polarisations P electric-field E switching behaviour reorientates the dipole moment leading the remnant polarisation or spontaneous polarisation P_s at zero applied electric field. The developed charge, and therefore the electric energy consumption of the material, indicates the energy conversion characteristics for pyroelectric energy harvesting. In addition, this switching behaviour extends the use of ferroelectric materials into the field of non-volatile memory applications (FeRam - Ferroelectric Random Access Memory).

According to Figure 2.5, a simplified image of pyroelectric energy harvesting is the utilisation of the ionic free energy due to a thermal change in the crystallography as an effect of the thermal transition [5]. When a poled pyroelectric materials is exposed to a heat flow Q, a direct increase in temperature dT follows. With electrodes attached perpendicular to the poling direction P, a change in polarisation dP due to the change in temperature dT repels or attracts surface bound charge. This behaviour is quantified by the pyroelectric charge coefficient (equation 2.2). When the surface bound charge becomes free due to a change in temperature, the surplus of electrons on one side in conjunction with the positive ions on the other side introduce an electrical potential. When the surface electrodes are under open circuit conditions, the change in polarisation translates into an electric potential difference V. Assuming the electrodes are under closed-circuited conditions, a current I flows accross an external electrical load. For a fully poled and electroded material of constant thickness d and constant surface electrode area A, the corresponding change in electrical

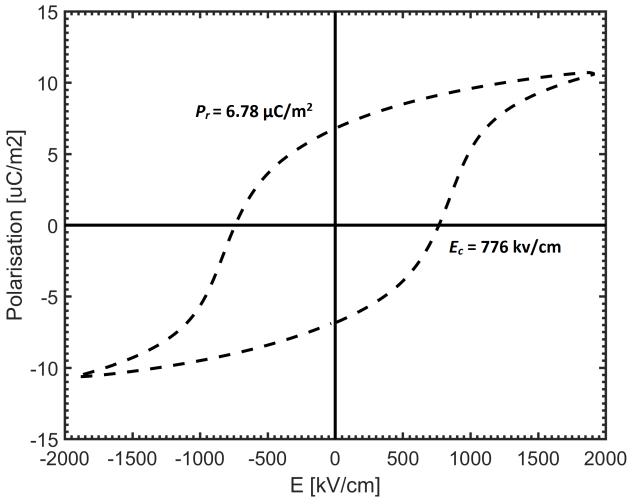

Fig. 2.4 Ferroelectric switching behaviour showing a polarisation P applied electric field E hysteresis for PVDF [115].

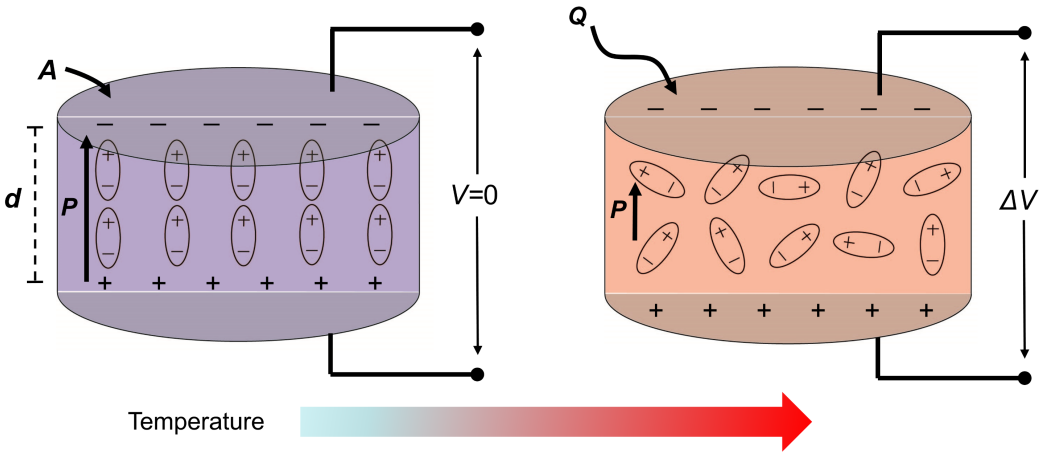

Fig. 2.5 Simplified image of pyroelectric energy harvesting [165].

potential difference ΔV is induced by a change in temperature ΔT is [35]:

$$\Delta V = \frac{p*}{\varepsilon} d.\Delta T \tag{2.4}$$

and under closed circuit condition the corresponding current I for the heating time increment dt follows:

$$I = p*.A\frac{\Delta T}{dt} \tag{2.5}$$

For cyclic heating ($+\Delta T$) and cooling ($-\Delta T$), the transient pyroelectric response translates into an alternating current (AC). At this stage, the interacting electrostatic, van der Waals and other forces arising from the overlap of electrons are neglected, reducing the pyroelectric effect to the dipole interaction [36]. The heat Q, requited to initiate the change in temperature ΔT, is the driving force of the thermal to electrical conversion process. When the pyroelectric element is used as a generator and connected across an external load, the potential difference V is utilised as a non-ideal pyroelectric energy source. Therefore, this work has a strong emphasis on the available electrical energy converted from the induced change in temperature and available from the external heat flow Q. In this work, a pyroelectric energy harvester is used as a synonym for a thermal to electrical energy converter or widely referred to as an electric generator.

2.4 Harvesting pyroelectric energy

Since the availability of energy is vital to our society, energy harvesting technologies have the potential to aid the problems associated with energy supply. When harvesting an available heat flow with pyroelectric materials, the aim is to maximise the energy conversion of a pyroelectric system and fully utilise the available ambient heat flow. Before testing the performance of an energy harvester, critical parameters need to be assessed in order to design a viable, integrated, and potentially highly efficient device [37]. Since pyroelectric systems require positive or negative changes in temperature dT/dt in order to continuously generate electricity, sequential heating and cooling is required. Based on the idealised assumption of perfect thermal-conduction, -convection or -radiation, the change in temperature dT for a constant heat flow W over the period of time dt is defined by (1^{st} law of thermodynamics):

$$dT = \frac{W.dt}{c_E.d} = \frac{W.dt}{c_p.\rho.h} \tag{2.6}$$

and dominated by the materials volumetric- (E) or mass- (ρ) and specific heat capacity $c_{p,E}$. As illustrated in Figure 2.5, the absorbed heat energy (Q) over the duration of heating (dt)

changes the temperature of the pyroelectric material. Consequently, the induced change is temperature dT translates into the change in polarisation in a pyroelectric material (equation 2.3). For a pyroelectric material of constant volume, equation 2.4 defines the generated pyroelectric voltage utilising the pyroelectric coefficient in equation 2.3. Since the developed electric potential V is equivalent to the converted thermal energy, the change in electrical potential dV in response to the absorbed quantity of thermal energy $Q = W.dt$ is defined as:

$$dV = \frac{p*}{c_E.\varepsilon} Q.dt \tag{2.7}$$

To account for the electrical energy stored in the potential difference, the charge density resulting from the change in polarisation needs to be determined. As a close geometrical approximation of the pyroelectric element in Figure 2.5, the equivalent architecture of a parallel plate capacitor matches the dielectric geometry of the pyroelectric material:

$$C = \varepsilon \frac{A}{d} \tag{2.8}$$

providing the available energy storage capacitance C for a particular geometry (A/d). To account for the total electrical energy $E_{electric}$ available for discharge, the parallel plate capacitor energy relationship:

$$E_{electric} = \frac{1}{2} C.V^2 \tag{2.9}$$

is employed in order to determine the transformed electrical energy in response to a change in temperature (equation 2.6) [38]:

$$E_{electric} = \frac{1}{2} \frac{p*^2}{\varepsilon} A.d.dT^2 \tag{2.10}$$

where the electrical energy is proportional to the induced change in temperature dT ($E \propto dT^2$).

2.5 Figures of merit (FOM)

When designing pyroelectric energy harvesting systems, the heat source is considered constant and determines the available heat flow. Therefore, optimisation of energy harvesting systems is limited to the geometrical harvester design, conditioning circuit, device positioning and material selection. The selection of the appropriate pyroelectric material during the design stage is a critical process. Therefore, figures of merit (FOM) are defined in order to rank potential or available materials and to obtain the best device performance for the available heat source. Derived from pyroelectric sensors applications, the optimisation of the

open circuit voltage (equation 2.4) and the closed circuit current (equation 2.5) provides a high voltage signal response [39]:

$$FOM_V = \frac{p*}{c_E.\varepsilon_r} = \frac{p*}{c_p.\rho.\varepsilon_r} \tag{2.11}$$

or a high current signal:

$$FOM_I = \frac{p*}{c_E} = \frac{p*}{c_p.\rho} \tag{2.12}$$

taking into account the volume (c_E)- or mass (c_p)- heat capacity times density (ρ), the relative permittivity (ε_r) and the pyroelectric coefficient ($p*$) of each material considered. However, according to equation 2.10, a high signal response for sensors does not necessarily translate into a high energy conversion with pyroelectric energy harvesting system. For this reason, and in order to add more information to the material selection process, an electro-thermal coupling coefficient k has been proposed taking into account the available heat source temperature T_{hot} [40]:

$$k^2 = \frac{p*^2.T_{hot}}{c_E.\varepsilon_r} = \frac{p*^2.T_{hot}}{c_p.\rho.\varepsilon_r} \tag{2.13}$$

and indicating the effectiveness of a pyroelectric energy harvesting system. Alternatively, the following FOM based on equation 2.10:

$$FOM = \frac{p*^2}{\varepsilon_r} \tag{2.14}$$

concentrates on the pyroelectric coefficient employing a squared relationship between the pyroelectric coefficient $p*$ and the permittivity ε, since the change in polarisation with temperature is usually low with pyroelectrics in comparison to the change in relative permittivity with temperature [41]. According to the proposed FOM in equation 2.14, the comparison of different materials for pyroelectric energy harvesting enables a simple performance estimate utilising standardised and widely available material specific coefficients. Scaling issues associated with the design of harvesters have been analysed by taking into account the electroded area A and thickness d of the pyroelectric material [42]:

$$P_{electric} = \frac{p*^2 \Delta T \frac{dT}{dt}}{\varepsilon} A.d \tag{2.15}$$

comparing the instantaneous power developed by the pyroelectric harvester. At this early stage of materials selection, the actual heating rate (ΔT times dT/dt) is difficult to estimate. However, based on the previous assumption of perfect thermal conduction, convection and radiation, the available heat and electrical energy density can be compared. When

substituting dT in equation 2.10 with dT from equation 2.6, the change in electrical energy density associated with the available heat power (W) required, can be compared:

$$dE = \frac{1}{2}\frac{p*^2}{\varepsilon_r c_E^2}\frac{A}{d}W.dt^2 \tag{2.16}$$

providing the increase in electrical energy density (dE) for the available heating period dt. When operating between two specific temperatures, the FOM provided in equation 2.14 defines the potentially best material. However, for the more likely condition of a constant energy source Q, Bowen et *al.* proposed a new FOM, defined as:

$$FOM = \frac{p*^2}{\varepsilon_0.c_E^2} \tag{2.17}$$

This pyroelectric energy harvesting FOM indicates that the pyroelectric material operating under constant heat source conditions should have a high pyroelectric coefficient $p*$ as well as a low heat capacity in order to maximise the energy density to achieve high changes in from from low energy inputs. For the idealised assumption of perfect heat transfer in combination with the assumption of infinite time, this static FOM provides a good first design approach for building a pyroelectric energy harvesting systems. However, the dynamic nature of pyroelectric energy conversion requires a constant change temperature $\pm dT$ driven by the available heat input ($+dT$) and the required heat removal ($-dT$) from the material. In particular, the thermal diffusion through the pyroelectric volume (A times d) is the limiting factor when sequentially inducing and removing heat from and to the system, since the temperature cannot rise infinitely.

2.6 Pyroelectric active materials

According to Figure 2.2, most pyroelectric materials belong to the subclass of ferroelectrics. A historical insight into ferroelectrics has been presented by Martiensse et *al.*, and the number of characterised materials is constantly increasing [43]. Materials for pyroelectric as well as electrocaloric applications were comprehensively reviewed by Li et *al.* [44]. Compared to pure pyroelectric materials exhibiting spontaneous polarisation in only one direction, ferroelectric materials exhibit a reversible switching polarisation of the dipole orientation when an electric field is applied. When used in energy harvesting systems, these materials need to be stable over many thermal cycles, capable of absorbing and ejecting heat rapidly, and operating below the Curie temperature (T_c) where the pyroelectric materials exhibit the required spontaneous polarisation. The wide use of pyroelectric active materials for IR and

heat sensing applications [33], thermal imaging [35], fire alarms, gas analysis and pollution monitors lead to a number of reviews on pyroelectric- [45] and ferroelectric-materials [46]. Since the subgroup of ferroelectrics exhibits strong pyroelectric activity, which are desired for pyroelectric energy harvesting systems (equation 2.16), this section reviews popular materials already used for pyroelectric energy harvesting and subdivides them into advanced single crystal ferroelectrics, crystalline ceramic ferroelectrics and organic ferroelectrics (Figure 2.2). According to figure 2.6 [35], the spontaneous polarisation-temperature slope is

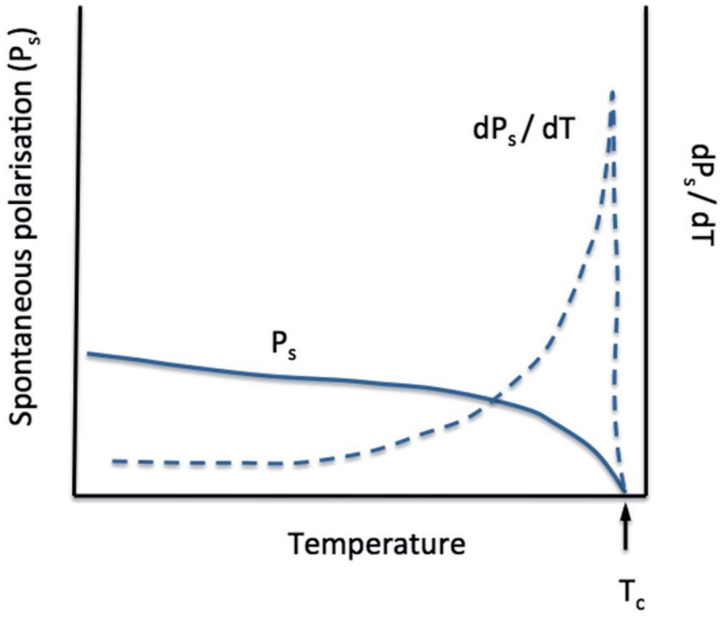

Fig. 2.6 Temperature dependence of spontaneous polarisation Ps and pyroelectric coefficient dPs/dT of a ferroelectric [17].

represented by the pyroelectric coefficient in equation 2.3. Most pyroelectric and ferroelectric materials experience a diminishing spontaneous polarisation with increasing temperatures. Close to the Curie temperature of the material, a rapid decline to zero in spontaneous polarisation takes place due to a crystallographic phase transition of the material, as shown in figure 2.6 [17]. Once the T_c is exceeded, the material looses pyroelectric activity and needs to be re-poled in order to exhibit spontaneous polarisation below T_c again. In the literature, the critical material specific parameters of pyroelectric coefficient $p*$ (equation 2.3), relative permittivity ε_r (equation 2.8) and heat capacity $c_{p,E}$ (equation 2.17), required for a comparative study and identified for the design of a viable energy harvesting systems, are reported as temperature independent constants. However, on a pyroelectric device level, specific performance improvements were obtained due to nano-scale engineering leading to pyroelectric materials with fewer defects [47], improved aspect ratios [48], enhanced

material processing with a higher grade of material purity (eg. higher T_c with PZT), and alternations in materials architecture or composite materials [49], which have unique combined properties (e.g. polymer-ceramic composite systems) [50]. All of these actions enhance the performance of pyroelectric energy harvesting devices. Therefore, only ferroelectric materials already used for pyroelectric energy harvesting are discussed here. Non-ferroelectric pyroelectric active materials such as aluminium nitride (AlN) [51], gallium nitride (GaN), cadmium sulphide (CdS), cellulose (CHO) and zinc oxide (ZnO) exhibit low pyroelectric activity and are therefore rarely used for pyroelectric energy harvesting systems. Table 2.1 compares popular pyroelectrics based on their FOM from equation 2.17 along with some uncommon biological pyroelectrics such as bone material [52]. For pyroelectric energy harvesting, most pyroelectric materials employed belong to the class of single crystals or crystalline ceramics. Similar to pyroelectric media, electrets also develop a voltage when heated. The only difference from a true pyroelectric material is that the polarisation of an electret is induced by an external electric/thermal treatment and eventually decays and disappears, in contrast to the thermal/electrical history of a pyroelectric materials where remnant polarisation remains quasi constant with time [53].

Table 2.1 Pyroelectric materials for energy harvesting [17].

Material	class	$p*$	c_E	k	ε_0	T_{Curie}	FOM	[Ref.]
	-	$\mu Cm^{-2}K^{-1}$	$kJkg^{-1}K^{-1}$	$Wm^{-1}K^{-1}$	-	$^{\circ}C$	-	-
Triglycine sulphoide SC (TGS)	organic/ceramic	-280	2.3	0.65	38	49	390	[35, 89]
PMN-0.25PT <111>	single crystal	-1790	2.5	2.5	2100	121	244	[186]
MN : BNT-BT <111>	single crystal	-588	2.89	-	279	-	148	[187]
Strontium barium niobate (BNT)	ceramic	-550	2.3	0.6	400	125	142	[35, 188]
Lithium tantalate ($LiTaO_3$)	ceramic	-175	3.2	3.9	47	665	63	[33, 89]
PMN-0.25PT	ceramic	-746	2.5	-	2100	-	42	[79]
Lead zirconate titanate (PZT)	ceramic	-380	2.5	0.8	290	200	79	[35, 189]
PZFNTU	ceramic	-380	-	1.25	290	100	-	[174]
Sodium nitride ($NaNO_2$)	ceramic	-40	2.2	2.2	4	164	82	[35]
Mn : MNT-BT <110>	single crystal	-513	2.89	2.89	535	-	58	[190]
CSBN x = 0.15	ceramic	-361	2.1	2.1	972	-	30	[191]
Mn : MNT-BT <001>	single crystal	-380	2.89	2.89	835	-	20	[190]
PVDF-TrFE (80/20)	organic	31	2.3	0.19	7	135	25	[192]
BNLKBT	ceramic	-360	2.83	-	858	-	18	[31, 33]
BNKBT	ceramic	-325	2.88	-	858	-	14	[35]
PVDF-TrFE (50/50)	organic	40	2.3	0.14	18	49	16	[192]
PVDF	organic	33	2.3	0.14	11	200	18	[38, 95]
KNN-LT	ceramic	-165	2.63	-	1230	-	3.2	[193]
KNN-LTS	ceramic	-190	4.48	-	1520	-	1.1	[193]
Lithium niobate	ceramic	-83	2.32	-	1210	-	1.0	[3, 44, 194]
$BaTiO_3$	ceramic	-210	2.5	2.60	1200	120	5.8	[3]
Nylon	organic	-5	1.8	0.25	31	-	0.2	[195]
Bone	ceramic	-7	5.0	0.53	200	-	0.0	[52]

2.6.1 Single crystals

Recent progress on atomic level engineering has enabled a controlled vapour growth of single crystal lead (Pb) magnesium (Mg), niobate (Nb) – lead (Pb) titanate (Ti) (PMN-PT), exhibiting enormous electromechanical coupling and pyroelectric activity. Colossal (French: 'huge') pyroelectric activity of $\sim 1500\ \mu Cm^{-2}K^{-1}$ with single-crystal PMN-PT pyroelectric materials has been measured when cut along the crystallographic [111] plane and poled normal to the plane [41]. With a phase transition temperature of 120 ºC, PMN-PT is limited to low temperature pyroelectric energy harvesting applications, experiencing a rapid depolarisation when exceeding T_c [54]. On the other hand, lithium niobiate ($LiNbO_3$) as well as lithium tantalate ($LiTaO_3$) have a high T_c of over 1120 ºC and 665 ºC respectively, but suffer of low pyroelectric activity for pyroelectric energy conversion of 20 $\mu Cm^{-2}K^{-1}$ at lower temperatures [55] or high at temperatures [56] with relatively low 0.0083 $\mu Cm^{-2}K^{-1}$ [57].

2.6.2 Crystalline ceramics

Most industrially used piezo-, pyro and ferro-electric ceramic materials belong to the group of lead (Pb) zirconate (Zr) titanate (Ti) oxides – PZT; this is a polycrystalline ferroelectric with high pyroelectric activity ranging from 250 $\mu Cm^{-2}K^{-1}$ for soft PZT and up to 550 $\mu Cm^{-2}K^{-1}$ for hard PZT [38]. The polycrystalline nature, the industrial scale of production and the in-depth characterisation of PZT makes this material widely used in industrial, defence and commercial applications. However, according to the EU regulation on Restrictions of Hazardous Substances directive (2003) (RoHS), the use of materials containing lead is restricted. In addition, perovskites are not ideal for certain applications due to their instability (reactive oxygen oxides), especially under high temperatures. Among a large number of lead free ferroelectric materials, new classes of ceramics are frequently used for energy harvesting purposes. Potassium (K) sodium (Na) niobium (Nb) oxides - KNN meet the design specifications of PZT, which can directly replace lead materials on a large scale on a device level [58]. Other popular groups of lead free materials are bismuth (Bi) sodium (Na) titanate (Ti) oxides – BNT [59] or more recently, barium (Ba) strontium (Sr) titanate (Ti) oxides - BST materials [60]. However, due to the conductive nature and dielectric losses of these materials, BNT ceramics are difficult to pole. Therefore, additives or dopants are added. As in PZT, where dopants change the crystallographic phase, modified ionic bonding in KNN, BST and BNT improve remnant polarisation and the pyroelectric activity for energy harvesting. Tailored compositions with maganese (Mn), nickel (Ni), antimony (Sb), tin (Sn) or tantalum (Ta) (among the rest of the chemical periodic table), lead to a modified crystal lattice with a higher pyroelectric activity of 350 $\mu Cm^{-2}K^{-1}$ instead 180 $\mu Cm^{-2}K^{-1}$ with a

mixing ratio of 0.5% (*mol*) Mn dopant with BST [61]. However, from a structural material engineering point of view, all single crystal and polycrystalline ceramics are hard, brittle, high density and expensive to manufacture.

2.6.3 Organic crystalline materials

Compared to ceramics, polymers exhibit a low change in polarisation magnitude with change in temperature. Reviews on organic pyroelectric materials including Das-Gupta in 1991 [62] and more recently by Horiuchi and Tokura [63], report a high pyroelectric activity in organic molecular carbon (C), hydrogen (H) and fluoride (F) based materials which experience a strong bonding with a relatively high pyroelectric activity and in organic-inorganic compounds such as triglycine sulphate (TGS). The ferroelectric γ- and β-phase chains in Polyvilylidene Difluoride (PVDF) polymer films exhibit a defined crystalline lattice with low permittivity. The change in polarisation, and therefore the hydrogen and fluoride orientation with respect carbon backbone as shown in Figure 2.7 [28], introduces a ferroelectric dipole moment. First reported by Kawai in 1969, the strong piezo- and ferroelectric active β-phase PVDF has isotropic pyro-electric properties with a pyroelectric coefficient ranging from 20 to 40 $\mu Cm^{-2}K^{-1}$ [64]. In contrast to the amorphous and non-ferroelectric α-phase, mechanical stretching aligns the molecules. The desired change in remnant polarisation can be induced by nucleation or by an externally applied electrical field [65]. Unlike single crystals, there is no classic binary switching of domains in polymer chains so that the level of polarisation is defined by the chain orientation, which makes PVDF exhibiting a 'ferroelectric-like' behaviour, but no ferroelectric binary state switching. However, since the material is defect free, ferroelectric polymers are of excellent use for non-volatile memories. Similar to ceramics, co-polymer dopants enhance the pyroelectric activity of pure PVDF. With 70 % PVDF and 30 % trifluoroethylene (TrFE) or chlorotrifluoroethylene (CTGE) or hexafluorpropylene (HFP), the pyroelectric coefficient improves up to 68 $\mu Cm^{-2}K^{-1}$ [66]. Therefore, PVDF and PVDF-copolymers derivatives (PVDF-TrFE or PVDF-TrFE-CFE) are an attractive material for pyroelectric energy harvesting because they provide a high toughness, high strain to failure, flexibility, low density, good bio-compatibility, scalability, transparency, and low cost [67]. Despite the high chemical stability, PVDF has glass transition temperature of -39 ºC, a low melting temperature of 80 ºC and an extrapolated T_c of 220 ºC limiting the range of applications [68]. Nevertheless, for pyroelectric energy harvesting the use of relatively low pyroelectric active PVDF will lead to a low energy efficiency, but high power factors (equation 2.15), since energy harvesters can be designed large, light, and cheap while the supplied thermal energy is considered free. In addition, PVDF is of particular interest for combined pyro-and piezoelectric energy harvesting applications since it has an extremely

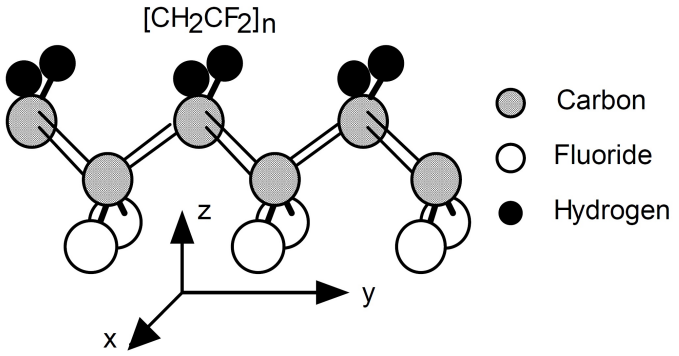

Fig. 2.7 Molecular bonding of β phase polyvinylidene-difluoride (PVDF) [28].

large stress range (from *kPa* to *GPa*) and sufficiently high thermal stability, is resistant to harsh chemicals as well as to energetic UV environments. The long life stability is proven on an industry scale in roof paints, pharmaceutical and chemical condensers, and in the packaging industry. Electro-active polymers can be can be produced in very thin transparent layers, films, and wires. When employed as a current source for energy harvesting, the linear piezo- and pyroelectric energy conversion properties of PVDF make this multifunctional material ideal for large scale energy harvesting systems. Other organic ferroelectrics such as Nylon have a pyroelectric coefficient in the range of 5 $\mu Cm^{-2}K^{-1}$ and therefore lack interest among the pyroelectric energy harvesting community.

2.7 Pyroelectric energy harvesting principles

In an effort to recover waste heat and achieve thermal energy harvesting, most of the available heat sources are low in temperature but large in heat flow. In order to fully exploit the available thermal energy flow and therefore maximise the transformed energy, the available temperature gradient needs to be fully utilised with the maximum change in polarisation (equation 2.3). As shown in Figure 2.5, the available potential difference in response to the performed change in polarisation can then be simply discharged across an external electrical load. When maximising this type of energy harvesting discharge circuit, the source impedance has to match the load impedance [69]:

$$Z_{Source} = Z_{Load} \tag{2.18}$$

in order to extract the maximum power from the pyroelectric harvester. Considering a purely resistive external load, the instantaneous power is then the product of the performed current and voltage accross a resistor. In the context for pyroelectric energy harvesting, resistive load impedance matching with industrial bulk PZT, PMN-PT and PVDF films were experimentally

characterised [70]. When alternating the material temperature between 30 ºC and 145 ºC over several minutes, optimum load resistances in the $M\Omega$ range were identified. According to the equation 2.4 and equation 2.5, various thin film geometry pyroelectric materials were tested across a fixed external resistance showing a good agreement with the pyroelectric theory [71]. Linear energy conversion characteristics were confirmed for pyroelectric thin- and thick-films [72]. With free standing energy harvesting applications and pyroelectric materials, substrate mounted PZT films [25] or ZnO layers also exhibit high durability and a linear thermal to electrical behaviour of pyroelectrics [73]. With similar performance properties, PVDF, and the PVDF copolymer derivative PVDF-TrFE, were also directly employed for energy harvesting when discharged across an external resistor [74] or simply rectified using a full-wave bridge circuit [75]. Material and geometrically independent, thin films, bulk, or nano-architecture pyroelectric materials have been used with synchronised switch harvesting on inductor (SSHI) [40], synchronised electric charge extraction (SECE) [76], synchronous charge inversion (SCI) [77] and synchronised switch damping on inductor (SSDI) circuit designs with a greater energy conversion effectiveness than traditional impedance matching approaches (equation 2.18) or a simple full wave bridge rectification with respect to the available thermal source [78]. Sebald et *al.* presented on how pyroelectric generators compare to thermoelectric generators (TEGs) on an energy harvesting level showing that a potentially higher efficiency can be achieved with pryoelectrics [79]. A more advanced

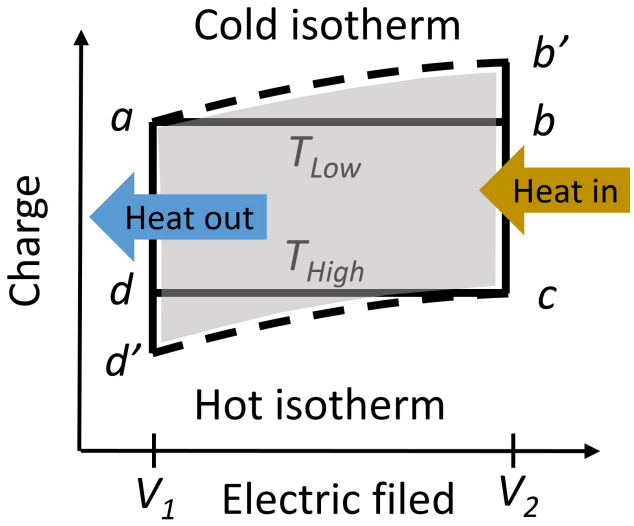

Fig. 2.8 The electrical Carnot and the Olsen-cycle (modified from [82]).

pyroelectric harvesting system can utilise the high pyroelectric activity by themo-dielectric modulation [80]. According to Figure 2.8, on changing the temperature of a pyroelectric while maintaining the available charge along the cold (a-b) and hot (c-d) isothermal line

and applying an external electrical field enables a form of thermodynamic cycling. In an approximate analogy to a liquid-vapour Carnot energy cycle, sequential iso-polarisation and iso-electrical changes of the material enables high efficiency energy pumping between the two temperatures, T_{low} and T_{high}:

$$\eta = 1 - \frac{T_{low}}{T_{high}} \tag{2.19}$$

providing an ideal thermal to electrical energy conversion efficiency [81]. The cycle consists of four strokes, starting (a) with charging the pyroelectric element to a high voltage (V_2) (b). As the temperature increases (b) to T_{High} at a constant applied voltage, the dielectric constant of the pyroelectric element decreases, and charge is forced to flow into the external circuit [82]. The applied voltage is then reduced to V_1 along the iso-polarisation line to (c) followed by a decrease in temperature to T_{Low} (d). At low temperatures, the applied electric field is then increased again from the external electrical circuit to V_2 (a). For this type of pyroelectric heat engine, the induced electric field can be almost completely recovered with an external capacitor leading to a surplus in electrical energy [83]. Since the pyroelectric Carnot cycle is difficult to realise, Olsen et *al*. replaced the iso-polarisation strokes by iso-thermal strokes [84]. According to Figure 2.8, replacing the horizontal lines by the dashed (a – b') and (c – d') electrical charge versus the applied electrical field strokes lines, led to an improvement of the harvested energy due to a greater change in polarisation followed by a higher surface charge density from the available temperature window. Therefore, employing this non-linear thermal and electrical behaviour improves the overall conversion efficiency, where the remnant polarisation requires an external electrical poling field for recovery. The area, covered by the Olsen cycle represents the surplus in electrical work, defined by [85]:

$$P_{electric} = \oint E\, dP \tag{2.20}$$

which is shown in Figure 2.8. Due to the need of additional external circuits charging and discharging elements for the pyroelectric generator followed by the complex synchronisation of electric charge and thermal flow, energy harvesting with the Olsen cycle is less popular with practical applications.

2.8 Pyroelectric energy harvesting devices

The very first reports of energy conversion utilising the pyroelectric effect dates back to 1961 where Clingman and Moore demonstrated a two diode circuit driven by a pyroelectric barium titanate oxide ($BaTiO_3$) capacitor, performing a thermodynamic cycle running at an efficiency

of 1 % compared to the limit of 10 % Carnot efficiency [86]. This work has been up scaled to a pyroelectric device employing a stack of pyroelectric elements [87]. A number of reviews on energy harvesting [88] with an emphasis on pyroelectric energy harvesting [89] or the review of different pyroelectric energy harvesting principles [82] divide this field in naturally driven, or passive, systems and in forced heating and cooling active systems. Figure 2.9

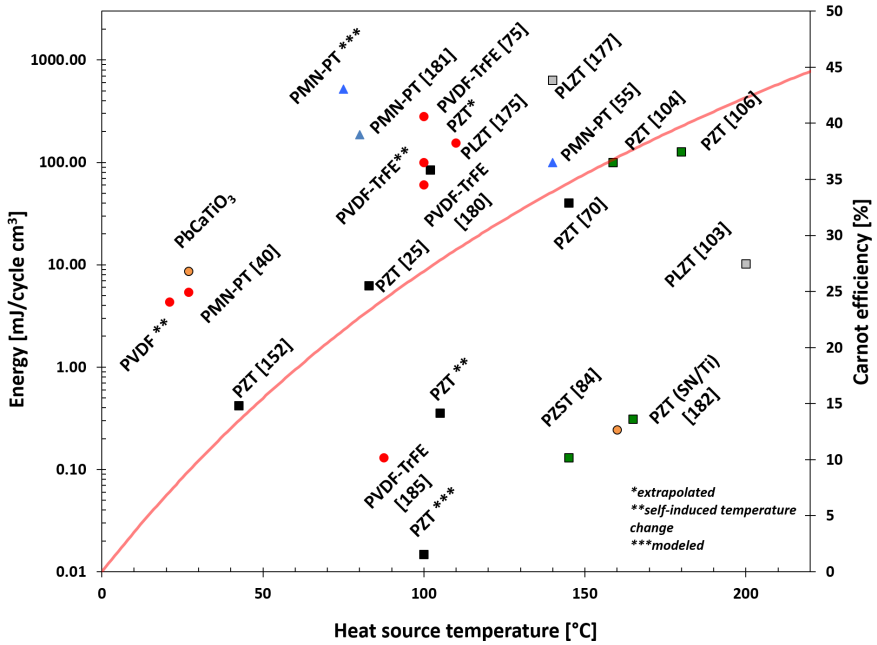

Fig. 2.9 Comparison of materials used for pyroelectric energy harvesting with respect to the heat source temperature along with the corresponding Carnot efficiency (red line) [38].

reviews the materials used for energy harvesting in the literature. When utilising relatively low temperatures in the range of 20 ºC to 100 ºC for energy harvesting, PVDF shows high energy conversion densities of 1 - 100 μJcm^{-3}. However, at higher temperatures PZT and PMN-PT perform much better, outperforming PVDF systems dramatically by one order of magnitude.

2.8.1 Passive energy harvesting

Passive changes in temperature are suitable for harvesting energy from road vibrations [90] and thermal impacts [91]. However, at room temperature, natural temperature fluctuations have been harvested with PVDF but are slow (day and nigh time temperature changes) leading to a low voltage in the range of 2 V [92]. The utilisation of low frequencies in combination with low temperatures leads to difficulties at the electric energy harvesting

in form of voltage thresholds and current leakage (parasitic losses). In addition, natural temperature oscillations remain rare and slow, usually well below 1 Hz.

2.8.2 Active energy harvesting

Efforts to increase the operating frequency and temperature magnitude of pyroelectric harvesting devices, include self-induced pyroelectric engines that make use of a bistable membrane for mechanical switching, generating an open circuit voltage of up to 13 V (primarily utilising the piezoelectric effect) [93]. Other theoretical approaches employ the difference in thermal conductivity between a liquid and a vapour fluid relying on mechanical motion of the pyroelectric engine [94] or a cantilever structure which mechanically switches the heat flow [95]. However, attempts to combine bimorphs with temperature changes have not been reported beyond the theoretical design stage [96]. For this reason, active changes in temperature without mechanical motion are demonstrated later in this work driving a pyroelectric generator with natural fluctuations in oscillating heat pipes.

2.9 Conclusions

The intrinsic need for a high energy density, high power output and low device cost with pyroelectric energy harvesters requires the full utilisation of the available heat energy using inexpensive materials. On a device level, high temperature pyroelectric ceramics operating in the temperature range between 100 ºC and 200 ºC compete with a large number of waste heat recovery and thermal energy harvesting technologies (e.g. thermoelectric modules, organic Rankine cycles). At lower temperatures, the available temperature gradient is limited, leading to a small heat flow and a slow thermal diffusion. Following an approach of enhanced heat transfer, the improved heat flow and thermal diffusion into the pyroelectric material maximises the thermal energy trade off and widens the operation range for this technology. In particular for polymer base materials, enhanced heat transfer lifts the energy density of pyroelectric harvesters to a competitive level. Eventually, an enhanced heat transfer leads to more effective and efficiency pyroelectric energy harvesting devices driving low power electrics and battery-less systems and fully utilising the available heat source.

Chapter 3

Pyroelectric characterisation

3.1 Introduction

Chapter 3 introduces heat transfer fundamentals for pyroelectric energy harvesting and identifies suitable pyroelectric materials classes and geometries. In order to obtain a systematic comparison of materials under consistent experimental boundary conditions, infra-red electromagnetic radiation heating for inducing controlled temperature oscillations in the pyoelectric was employed. Geometrical optimisation for uniaxial heating revealed that thin films are the most favourable architecture for pyroelectric energy harvesting.

3.2 Heat transfer with pyroelectrics

When harvesting thermal energy with pyroelectrics, the developed change in temperature is the driving force of the solid state thermo- to electrical-energy conversion process. This multi-physics phenomenon requires a systematic and controlled evaluation procedure when comparing different materials, devices and structures exposed to an ambient heat source. Radiation, conduction, and convection heating, or a combination of all heat transfer principles, have been utilised for pyroelectric energy harvesting and reported in the literature [38]. Despite the material specific pyroelectric performance (equation 2.3), the heat transfer characteristics are governing the energy conversion effectiveness. Therefore, the key to delivering a viable pyroelectric harvesting system is to identify an application where the heat flow and the temperature changes are sufficiently rapid in order to generate useful power, since naturally occurring temperature fluctuations are often small (e.g. day and night temperature changes) and slow (e.g. 24 hours). Since the harvester has to be exposed to a continuous change in temperature (dT/dt) in order to generate electricity and a high

current (I), fast and large transient changes in temperature is of pivotal importance for the effectiveness of the harvesting system. When examining pyroelectric media, all pyroelectrics are naturally electrically- and thermally-insulating for which reason heat cannot diffuse quickly. Consequently, improving the material's electrical- and thermal-specific performance will lead to better pyroelectric energy harvesting devices [37]. For this reason, realistic test procedures are developed in this chapter that are suitable to characterise the pyroelectric energy harvester under a wide range of potential thermal energy sources. This work does not intend to measure materials specific coefficients, but aims to test pyroelectric devices and structures for energy harvesting. With a large number of publications regarding the characterisation of pyroelectric media, Lubomirsky and Stafsudd reviewed in detail the available pyroelectric measurement principles and led to the conclusion that only a stress free, strain free and unclamped homogeneous- or uniform-heating enables a precise pyroelectric coefficient measurement under open circuit and closed circuit conditions [53]. Although the pyroelectric coefficient is a material specific constant, defining the relative change on polarisation with temperature under closed circuit conditions, the only way to extract energy from the system is to discharge the energy across an external load. Therefore, the voltage mode of operation is used in energy harvesting application. However, since the relative permittivity is affected by the change in temperature (the material is more conductive at higher temperatures), the available energy (equation 2.9) is potentially lower than the calculated theoretical values. For this reason, experimental results will be obtained across a wide temperature span with pyroelectric materials in order to quantify distortions of relative permittivity and changes in the pyroelectric coefficient. Finally, the results presented are limited to temperatures above room temperature, conducting a device optimisation based on material selection and thermal device engineering [97].

3.3 Transient change in temperature

The change in temperature (dT) of the pyroelectric as a function of time (dt), has an effect of the unsteady transferred heat ($Q = W.dt$), which is the driving force of the pyroelectric inducing the change in dipole moment and generating pyroelectric energy. Since the available temperature window is usually constant (the available temperature gradient from the ambient heat source), it is crucial to understand the dynamics of the heating and cooling procedures. With the pyroelectric harvester operating between two absolute temperature differences defined by T_1 (heat source temperature) and T_2 (heat sink temperature), the thermal boundary condition for the heat transfer analysis are considered constant. Consequently, the change in

temperature is:

$$dT = T_2 - T_1 \tag{3.1}$$

providing the effect change in heat. The energy Q transferred into a pyroelectric volume V is defined by rearranging equation 2.6 and substituting equation 3.1 into equation equation 3.2:

$$Q = W.dt = V.c_v(T_2 - T_1) = V.\rho.c_p(T_2 - T_1) = m.c_p(T_2 - T_1) \tag{3.2}$$

for the material mass m, volumetric heat capacity c_v or mass heat capacity c_p. Following equation 3.2, the heat transferred is a function of the available temperature gradient. However, assuming infinite time for the duration of heating, a thermal equilibrium between the heat source and the pyroelectric volume occurs ($T_2 \approx T_1$), in which case pyroelectric energy will be no longer generated. In order to quantify this state, Newton's law of cooling is employed utilising an experimental surface conduction coefficient h (empirical number) [98]:

$$q = h.A(T_\infty - T) \tag{3.3}$$

with:

$$T_\infty = T_2$$

and

$$T = T_1$$

accounting for the uniaxial heat flow q across the solid control volume area A, when exposed to the heat source. Based on the assumption of perfect conduction, heat immediately dissipates through the volume at:

$$q = \rho.V.c_p\frac{dT}{dt} = m.c_p\frac{dT}{dt} \tag{3.4}$$

Equating equation 3.3 and equation 3.4, separating variables and integrating between the two temperatures T_1 and T_2 for the duration of t_1 and starting with $t_0 = 0$ leads to:

$$\int_{T_1}^{T_2} \frac{1}{T - T_\infty} dT = \int_0^{t_1} \frac{h.A}{\rho.V.c_p} dt \tag{3.5}$$

so that:

$$\frac{T - T_2}{T_1 - T_2} = e^{[-\frac{h.A}{\rho.V.c_p}t_1]} \tag{3.6}$$

where the pyroelectric control volume temperature T is a function of the heating duration t. This fundamental relationship between energy, temperature and time governs the pyroelectric energy conversion dynamics. Therefore, when the pyroelectric surface is heated or cooled, the system experiences an exponential decay in temperature change with time $T(t)$, due to the diminishing change in available temperature difference $t_\infty = (T_2 - T_1) \approx 0$. This basic introduction into transient heat transfer assumes finite time and perfect thermal diffusion in pyroelectric media. However, since pyroelectric media is thermally and electrically insulating, heat cannot diffuse quickly followed by a temperature gradient across the material. Therefore, the perfect conduction assumption does not fully apply and the pyroelectric volume is thermally resistive along the thermal penetration depth x, perpendicular to the heating surface A. Since most pyroelectric materials are ceramics or polymers, isotropic thermal conduction properties for the pyroelectric control volume need be assumed with a constant thermal conductivity k along the defined heating direction x. Following Fourier's law for conduction in a macroscopic solid, heat transfer in a thermally resistive media is described by an empirical thermal diffusion coefficient k providing an analytical solution for conduction [99]:

$$q = -k.A\frac{dT}{dx} \tag{3.7}$$

for uniaxial (dx) heating. From an engineering perspective, this simple relationship describing the diffusivity (temperature with time spatial distribution) across the pyroelectric material serves reasonably well when analysing thermal energy harvesting applications. According to equation 3.6 and equation 3.7, the exponential temperature envelope for uniaxial heating is described by the following second order differential equation [96]:

$$\frac{dT}{dt} = \alpha\frac{d^2T}{dx^2} \tag{3.8}$$

with:

$$\alpha = \frac{k}{\rho.c}$$

providing the time- and spatial-solution for the change in temperature assuming a constant diffusivity α. Since h (equation 3.6) and k (equation 3.7) are empirical numbers, experimental results are required to verify the semi-analytical analysis. For thermally conductive materials, such as aluminium with a diffusion coefficient > 10000 m^2s^{-1}, the assumption of perfect conduction is reasonable, reducing the thermal analysis to equation 3.6. However, when using insulating ceramics or polymers, which have small diffusion coefficients, this approach oversimplifies the thermal analysis. For this reason, the thermal analysis requires a numerical approach solving equation 3.8, since an exact analytical solution is not available [96].

Table 3.1 Thermal and electrical properties of popular pyroelectric materials [97]

Material	$p*$	c_p	k	ρ	α	[Ref.]
	$\mu Cm^{-2}K^{-1}$	$kJkg^{-1}K^{-1}$	$Wm^{-1}K^{-1}$	kgm^{-3}	m^2s^{-1}	-
PMN-PT	1071	300	2.60	7.90	1.090	[38, 97]
PZT	533	500	1.10	7.50	0.290	[38, 97]
$BaTiO_3$	210	400	2.60	6.20	0.270	[38, 97]
PVDF	33	1500	0.19	1.78	0.071	[38, 97]

Generally, materials with a high diffusivity respond faster to their thermal environment followed by a greater thermal penetration depth. Eventually, a greater penetration depth will lead to a greater change in temperature dT followed by a higher pyroelectric conversion efficiency. According to *van der Ziel*, the product of the specific heat, density, area and heat conductivity should be as small as possible which maximises the area and minimises volume [99]. However, according to equation 2.17, the energy harvesting device also requires a low permittivity and low heat capacity in order to store the transformed electrical energy (equation 2.9). Table 3.1 compares popular pyroelectric materials based on their thermal and electro-active properties. Based on the thermal diffusivity α, PVDF is thermally highly resistive, compared to ceramics and single crystals, but also experiences scaling effects for thick layers [101]. Especially for thin films ($< \mu$m), thermal conductivity improves and the anisotropic properties along the polymer chain direction enable multifunctional device properties.

The heat transfer analysis becomes more complex when the pyroelectric energy harvester is utilising different energy sources such as wind and solar [102], or random energy sources for conduction and radiation [92]. When utilising the pyro- as well as piezo-electric effects for energy harvesting, difficulties in synchronising the thermal flow and the mechanical force lead to complex modelling solutions [93]. Therefore, this work evaluates only experimental data for the analysis deriving optimisation parameters based on an empirical approach for different energy harvesting systems and architectures. In the following sections the different heating principles used for pyroelectric energy harvesting are reviewed and the operation parameters are discussed.

3.3.1 Conduction with pyroelectric materials

In order to test materials for energy harvesting, basic heat conduction experiments have been initially carried out by placing the pyroelectric active material on a hot plate for heating. The change in temperature generated by the conductive heat flow across the contact area between

the hot plate and the pyroelectric element generates a change in temperature, starting from room temperature [92] [103]. With a relatively fast heating rate of approximately 2 Ks^{-1} and a cooling rate of less than 1 Ks^{-1}, the performed pyroelectric conversion cycles with PVDF-TrFE enabled high energy densities ($\approx 155 mJcm^{-3}$). The highly non-symmetric nature of the thermal conduction method is due to a high thermal mass in contact with the pyroelectric when cooling, and affects the results when comparing different pyroelectric materials as well as the physical motion needed to put the materials in place. Smaller resistive heating elements enables a synchronous heating with up to 14.5 Ks^{-1} and discharging of the pyroelectric device across an external load, which provides important information on the electric power generated [70] and maps the potentials for energy harvesting with PZT thin films [71]. Employing a more advanced heat conduction experiment, Olsen et *al*. utilised a hot and cold oil bath in contact with the pyroelectric material [104] followed by hot and cold oil pumping apparatus operating between 138 ºC and 195 ºC [105]. When improving the experiment, the oil bath was heated by a resistive element with controlled changes in temperatures utilising contact heating and enabling thermal oscillation at 160 ºC heat source temperature [106]. Recently, a numerical heat transfer model confirmed the Olsen fluid pump experiment with contact conduction between a heat transfer fluid and lead zirconate stannate titanate (PZST) operating at temperatures of 185 °C [107]. However, in order to reduce the high temperature level and to remove heat from the pyroelectric element, a harvester was thermally cycled by a Peltier device (Seebeck effect like in a TEG) [69]. With heating and cooling rate of 0.1 Ks^{-1}, controlled temperature experiments were conducted [108]. However, the changes in DC driving current of the Peltier module induce an electrostatic and magnetic field affecting the pyroelectric when measuring mutli-ferroic materials, since certain ferroelectrics are also ferromagnetic. In addition, the low frequency nature of the temperature oscillations and the nature of small pyroelectric current signals (usually in the *nA* range) at the presence of high electromagnetic noise leads to intensive data post processing and trapped currents, affecting the measurement in an unfavourable way [109].

3.3.2 Convection with pyroelectric materials

Unlike thermal contact conduction, natural or forced convection is a buoyancy driven energy flow creating mechanical pressure and affecting the pyroelectric energy harvester as thermal (pyroelectric) as well as mechanical (piezoelectric) energy converter. For this reason, the pyroelectric response to heat and the piezoelectric response to mechanical pressure cannot be readily distinguished. When employing a hot air gun ('hair dryer') for thermal cycling, a forced and free cooling mechanisms are active, harvesting pyroelectric energy between room temperature and 60 °C [25]. When harvesting forced convention, the surface area exposed

to the heat flow as well as the area exposed to the air flow is active [110]. In this regard, natural ambient temperature oscillations acting slower on the materials are more difficult to control. However, since the piezoelectric materials are highly sensitive to mechanical energy, the system is more likely to be allocated in the category of piezoelectric energy harvesting due to the higher mechanical to electrical energy conversion efficiency rather than the less efficient category of pyroelectric energy harvesting.

3.3.3 Radiation with pyroelectric materials

Thermal radiation, or electromagnetic solar radiation, is the most powerful and potentially free ambient energy source. Efforts in harvesting solar energy in the higher wavelength (μm to mm) lead to the utilisation of solar driven pyroelectric generators. For this type of energy harvesting devices, a complete thermal analysis was published, providing higher changes in temperature for radiative than conductive heat transfer [110]. In order to heat the pyroelectric active material, an infra red (IR) lamp was used. By varying the IR lamp beam intensity, controlled heating experiments for relatively slow heating rates were conducted [111]. For an identical IR lamp setup, a mechanical chopper rotating disc was used, where open areas in the disc enable a controlled synchronous but not symmetrical temperature oscillations. When changing the rotating disc speed, the oscillation frequency was varied between 0.5 Hz and 620 Hz [112]. Other approaches use an IR lamp providing a constant radiation beam for absorption, reflection and transmission measurements [113]. When radiation heating is employed, it is difficult to estimate the amount of thermal energy absorbed by the pyroelectric harvester [53]. However, since only the perfromed change in temperature with respect to the energy input of the heat source is important for energy harvesting, the heat radiation analysis can be neglected at this point. According to *van der Ziel*, this is considered sufficiently accurate when comparing simple single layer structures [99]. When heating thin films, multilayer structures or encapsulated devices, a detailed heat transfer study needs to be completed prior to conducting the radiation energy harvesting experiments.

3.4 Radiative heating test rig

In order to test, examine and harvest thermal energy with pyroelectric devices, controlled temperature oscillations are introduced and the pyroelectric energy transformation performance as well as geometric effects on the transient heat transfer are measured. With multiple mechanical and thermal sources, a distinctive analysis of an energy harvester separating the sources is difficult to obtain. Therefore, this work employs a single contact less radiation heat

source providing constant measurement conditions across all types of simple pyroelectric energy harvesting structures. Based the fundamental heat transfer equation 3.2, 3.6, 3.8, and on Kirchoff's Law in 3.10, constant thermal heat source conditions are realised using a single radiation source. With radiation, there is no physical contact between the heat source and the solid test specimen (liquid pyroelectric materials are not considered in this work). This enables consistent heating experiments as long as the test sample thickness is much thicker than the radiation beam wavelength λ. Consequently, substrate mounted materials in the low *nm* thickness range require more sophisticated radiation sources (e.g. laser) or convection and conduction heating principles, limiting the use of widely available industrial IR light sources for heating. In this regard, ideal radiation heating measurement would take place in a vacuum, which is more difficult to realise, where a lack of vacuum directly translates into an experimental uncertainty (further discussed in section 3.6.1 of this work).

As shown in Figure 3.1, a Philips 175 W infra red (IR) lamp (PAR38) 230 V (diameter 121 *mm*) heating lamp is powered by a main electric power supply (230 V - AC). The high voltage power line is controlled by a variable increment power transformer (Zenith - England), continuously adjusting the lamp radiation intensity. Temperature oscillations are realised by switching the lamp periodically 'on' and 'off' using a variable frequency controller covering the switching frequency range from mHz to Hz. According to the equivalent circuit shown in Figure 3.1, a high voltage power line (230 V - AC) is binary controlled by a low voltage signal line (5 V - DC) to switch a power relay. Each component is commonly grounded. When the light is switch on, the exposed pyroelectric test device is heated and when the light is switched off, free convection cools the pyroelectric test device. During the off phase of the lamp, free air convection cools the sample on each side by a technically infinite heat sink, assuming the room air temperature is maintained at a constant (22 °C). Since the test samples is exposed only from one side (top down) to the IR radiation beam, uniaxial heating similar so solar radiation heats the test specimen. Temperatures were captured when the system established a thermal equilibrium and the average temperature of the specimen with the switching lamp was constant. The temperature was constant when the lamp periodically (duration 'on' time = duration 'off' time) was periodic so that the average temperature remains constant, where the average heating and cooling energy cancels each other out. Then, the specimen energy balance aggregates to zero for radiative heating and convective cooling, neglecting other heat transfer phenomena [96]. The performed changes in temperature are measured using leaf type K-type thermocouples (Omega - US) at the surface of the specimen. The thermocouple is electrically insulated from the conductive surface of the pyroelectric materials with a thin coating of lacquer. For temperature data acquisition, a PicoTech (UK) data logger (TC - 08) is used with a maximum sampling rate of 10 Hz and with the thermocouples

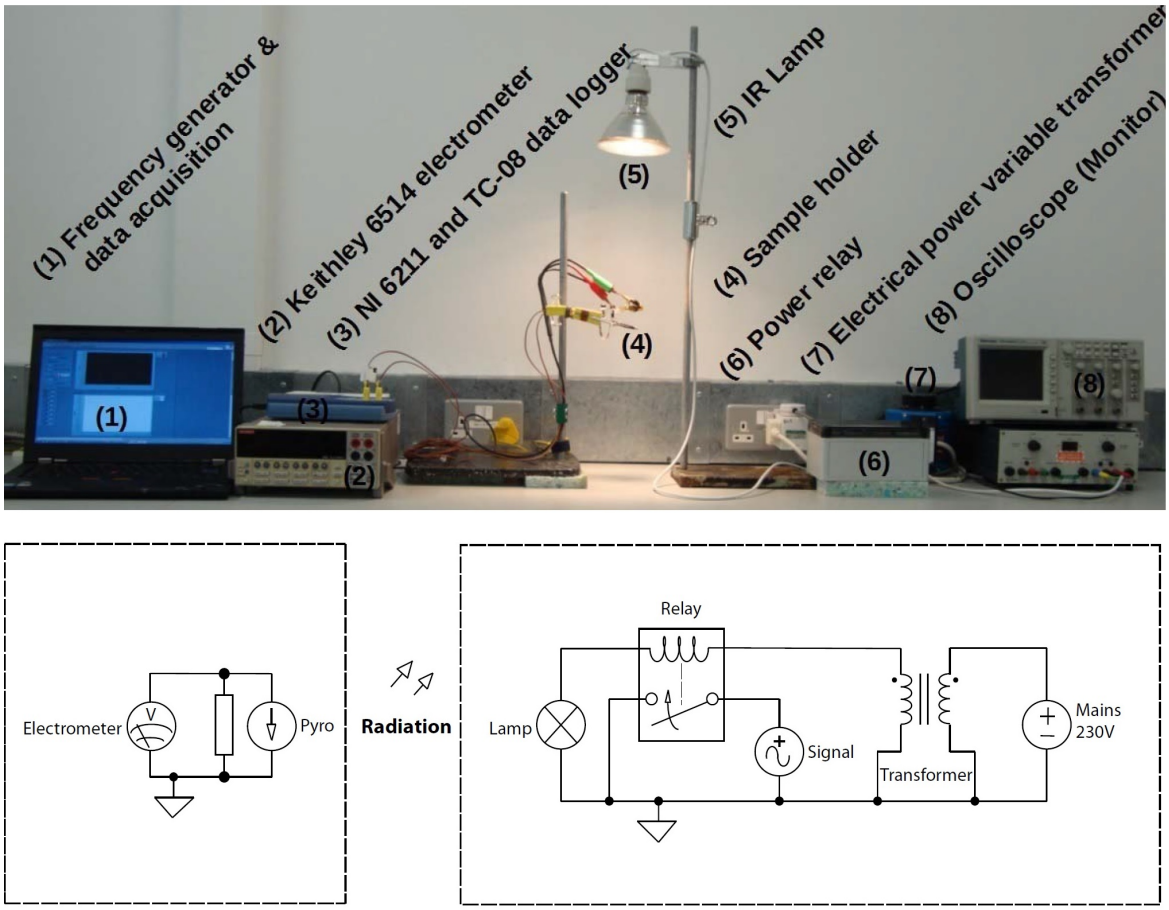

Fig. 3.1 Setup of pyroelectric IR-lamp test setup and circuit equivalent developed in this work.

attached to the top and bottom surface of the material. Other temperature measurement techniques such as a bolometer, a thermistor or a thermal radiation technique (which also use pyroelectric materials) seem possible but are not used for reasons of measurement accuracy and device simplicity. For pyroelectric device characterisation, the pyroelectric open circuit voltage (equation 2.4) and closed circuit current (equation 2.5) is measured using a Keithley (US) 6517 high input impedance electrometer (200 $T\Omega$). According to Figure 3.1, only the electromagnetic radiation from the lamp can interfere with the electrical measurements. However, it is important to notice that with different types of pyroelectric ceramics and polymers, an un-poled reference material is also needed to be tested [36]. In addition, if the sample is heated faster than the thermal diffusion time, the material is heated non-uniformly introducing a strong secondary piezoelectric contribution (equation 2.3) [53]. At such a condition, conduction only governs the change in temperature defined by the lumped capacitance model (analogue to electrical resistance in an electrical system). However, since the test conditions for temperature oscillations are maintained small and slow, the propose set-up with a data sampling rate of over 10 Hz for the temperature and 100 Hz for the electrical measurements is designed well above the Nyquist limit of *1/2* the signal input frequency. With the samples being directly exposed to the IR-beam, the corresponding rate of change of temperature dT/dt (equation 2.5) is calculated using the time forward derivative [114]. The pyroelectric signals together with the recorded temperatures are acquired in a LabVIEW (US) environment for data analysis and data processing.

From a thermal energy harvesting point of view, only the performed change in temperature providing the available voltage and current is of interest for the pyroelectric energy harvesting measurements. Therefore, the approximated value of the thermal energy processed and absorbed is a results of the experienced change in temperature (dT). This measure serves reasonably well to describe the efficiency of a systems and compare it with other harvesting devices. For the heating energy, the transient performance (time domain) provides the work integral, deriving the average heating power. However, parallel to the experimental evaluation of the energy harvesting systems, an analytical solutions for the relationship between emitted radiation power and temperature is described by Planck's Radiation law [116]:

$$U(\lambda,T) = \frac{2h_c v^3}{c^2} \frac{1}{e^{h_c v/k_B T - 1}} \tag{3.9}$$

where h_c is the Planck's constant, c the speed of light and k_B the Boltzmann constant. Since for energy harvesting the emitted power by the lamp is considered free, there is no need for a detailed lamp analysis. However, the energy available to the pyroelectric sample for the duration of the experiment as well as under variable radiation conditions when

changing the lamp intensity, is of importance for the energy harvesting device characterisation. Therefore, for a gradual increase in electric power in equally spaced 10 % continuous radiation increments starting from 10 % to 100 % power (175 *Watt*), Figure 3.2 presents the thermal power available for absorption. The reported power density was measured with a calibrated thermal power sensor (THORlabs – Germany) at a 20 *cm* distance to the lamp. The sensor

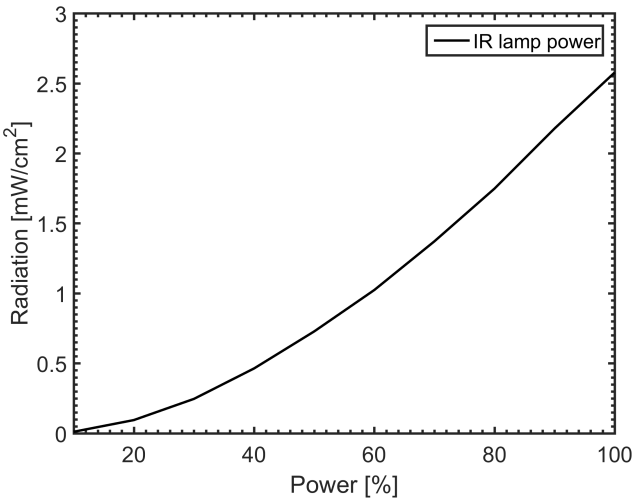

Fig. 3.2 IR-lamp intensity with increasing electrical power.

covers the wavelength range from 190 *nm* to 25 μm. For an increasing electric power supply to the lamp, the measured absorbed thermal power by the sensors is also gradually increasing up to 2.5 $mWcm^{-2}$ at 100 % power. This value is close to the maximum natural solar radiation on earth. When absorbing the available thermal power, Kirchhoff's law of spectral radiation:

$$1 = reflection + absorbance + transmittance \tag{3.10}$$

defines the relationship between reflected, absorbed and transmitted radiation for the test specimen. Since these phenomena depend on the radiation wavelength, the material employed, the surface finish (roughness) and the thickness, together with other material and manufacturing specific parameters, a detailed study is not scope of this work. However, it is important to notice the differences in radiation intensity across the available lamp specific wavelengths in order to compare and optimise it for ambient radiation sources such as e.g. solar. In addition, since most of the pyroelectric materials employed for energy harvesting are well characterised with respect to electromagnetic radiation absorption, the emittance of the IR lamp across the different wavelength needs to be compared with the available radiation source when charactering pyroelectric device for ambient energy harvesting.

According to Figure 3.3, the spectral emissivity of the lamp employed in this work across an increasing wavelength is presented for the incremental electrical power presented in Figure 3.2. The emissivity was measured using an Ocean optic nanoCalc XR sensor (US)

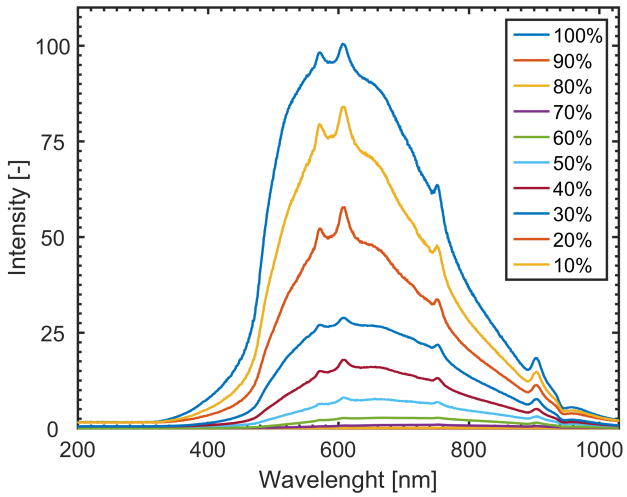

Fig. 3.3 IR-lamp intensity against electromagnetic wavelength with increasing electrical power.

and the Ocean optic Spectra suite (light chromatographer) device placed 42 *cm* away from the IR lamp used. For the power increments presented in Figure 3.2, the corresponding wavelength distribution shows a peak around 700 *nm* with a trend towards 600 *nm* with increasing power. When integrated across the available wavelength spectrum, the heating experiments performed in this work have a peak intensity around the visible light spectrum. The wavelength specific radiation energy can then be determined by the Stefan-Boltzmann Laws:

$$W = k_B.A.T^4 \tag{3.11}$$

providing the radiation power with $k_B = 5.67x10^{-8}Wm^{-2}K^{-4}$ and the available heat source temperature T. Considering a nonlinear wavelength absorption of crystalline materials, it is of importance to notice that the integrated energy absorption leads to the converted thermal energy. Therefore, the experienced change in temperature (dT^4) by the specimen accounts for the total energy absorbed. Due to an inherent lack of natural and ambient temperature oscillations, the pyroelectric effect and its application in energy harvesting suffers optimisation difficulties on a device level. For this reason, the presented heating set-up enables a systematic heating experiment for pyroelectric media under elevated temperatures.

3.5 Testing pyroelectric materials

Pyroelectric active bulk soft PZT type PIC255 material with silver electrodes, supplied by PI Ceramics (UK), was thermally exposed to IR radiation for duration of 30 sec. The characterised by the manufactured and industrially pre-poled material is a subgroup of PZT with a high T_c of 350 ºC and generally used for high temperature sensor and actuator applications. In order to characterise the pyroelectric properties and to demonstrate pyroelectric energy harvesting performance, the open circuit voltage was measured for a constant heating rate of 2.5 $mWcm^{-2}$ at 100 % lamp intensity. While the material was heated under open circuit conditions, the resulting potential difference, ΔV, across the surface electrodes was measured so that the system behaves as a parallel plate of capacitance C (equation 2.8). The corresponding temperature, voltage and the electric field E for an induced change in temperature ΔT is presented below [97].

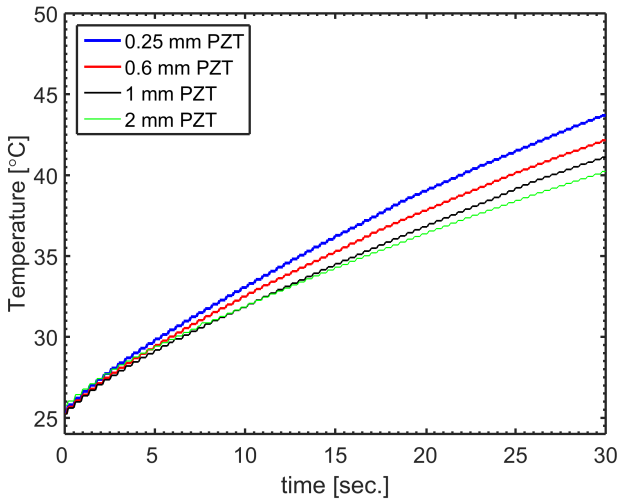

Fig. 3.4 Pyroelectric materials surface temperature for different PZT thickness at constant heating conditions of 2.5 $mWcm^{-2}$.

Under constant thermal boundary conditions, the heating profile in Figure 3.4 shows a constant increase in surface temperature for the test samples (0.25 *mm*, 0.6 *mm*, 1 *mm* and 2 *mm* thick). After 30 sec. of heating, the thin 0.25 *mm* PZT sample has a 5 *K* higher surface temperature compared to the 2 *mm* PZT sample.

Figure 3.5 shows for the constant heating power the pyroelectric voltage of the thermally exposed PZT discs (1.4 cm^2) of thickness $x = 0.25$ *mm*, 0.6 *mm*, 1 *mm* and 2 *mm*. According to equation 2.7, a thicker material develops a higher voltage; but the same electric field $E = V/x$ as thinner samples. However, due to thermal diffusion, the early portion of the heat wave changes the temperature faster in a thin sample than in a thick sample providing an initially

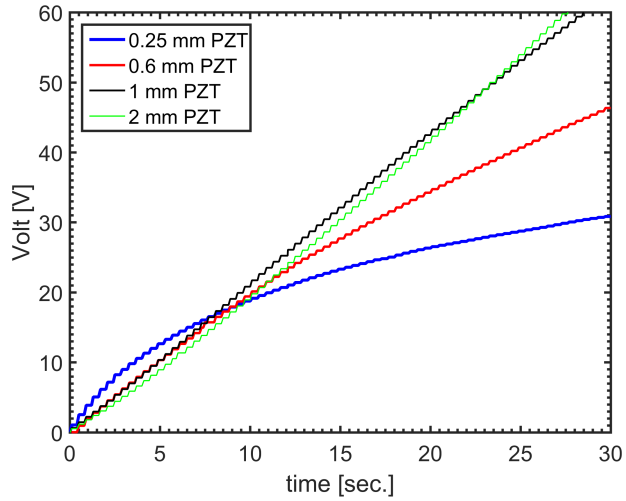

Fig. 3.5 Pyroelectric voltage for different PZT thickness at constant heating conditions of 2.5 $mW\,cm^{-2}$.

higher voltage for the first 8 sec. of the heating cycle. It can also be observed that thin samples reach thermal equilibrium (and constant voltage) faster, due to a smaller thermal mass [97].

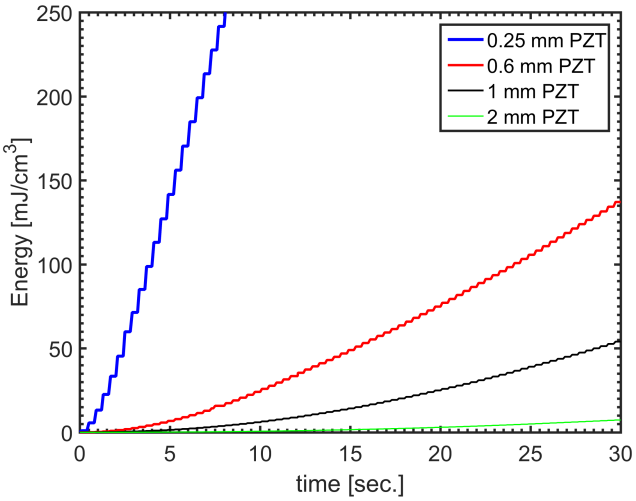

Fig. 3.6 Energy stored in the pyroelectric element for constant heating with PZT at constant heating conditions of 2.5 $mW\,cm^{-2}$.

The energy stored in the pyroelectric element equals the available electric energy for discharge, and corresponds to the accumulated free charge, stored in the material. Figure 3.6 shows the corresponding electrical energy stored in the pyroelectric element for constant

heating, calculated with:

$$E_{electric} = \frac{1}{2}C.V^2 = \frac{1}{2}\varepsilon_r\varepsilon_0\frac{A}{d}V^2 = \frac{1}{2}1750x8.86x10^{-12}\frac{0.00014}{d}V^2 \tag{3.12}$$

On a volumetric base, the energy densities are much higher for the thin 0.25 *mm* PZT than for a 0.6 *mm*, 1 *mm* and 2 *mm* PZT at an identical surface area A. When exposed to a radiative beam, thin materials reach high temperatures faster than thick materials. In addition, the capacitance for thin samples is significantly higher (equation 2.8) than for the thick sample of 1 nF and 8.76 nF, respectively. The slow rise in accumulated energy of the thick samples can be explained by the longer duration for the thermal diffusion of heat. For a thick sample, the heating rate becomes impractically long and the stored energy per unit volume remains low and thus thin materials are preferred. In addition, the energy stored in a pyroelectric generator as a capacitor for an extended amount of time can leak and reduces the energy transformation; for example although the reported (PI Ceramics - UK) loss ($tan\delta$ = 0.014) is small , it is finite [96]. For this reason, thin materials with a larger surface areas are preferred for pyroelectric energy harvesting providing a higher energy conversion compared to thick materials under constant thermal boundary conditions.

3.6 Experimental uncertainties and data analysis

When conducting pyroelectric experiments for energy harvesting, the analysis can be reduced to a thermal input (temperature, heat flow and temperature oscillation frequency) and an electrical output (energy and energy density) in order to quantify the performance. The linear energy conversion relationship for the pyroelectric voltage (equation 2.4) and current (equation 2.5) provides analytical plausibility when testing pyroelectric energy systems. However, experimental uncertainties, associated with the energy transformation from heat to electricity need to be identified, mitigated and when possible eliminated in order to draw fundamental conclusions and report empirical data.

3.6.1 Measurement uncertainties

When designing an experimental setup, the experiment must be reproducible and repeatable under equal environmental ambient conditions. Limiting the number of variables requires the employment of material ($p*$, d, ρ), thermal (k, h, α), mechanical (d, τ) and electrical (λ, ε) specific constants affecting the pyroelectric performance (I, V) and therefore the available energy. This assumption is attributed to a large number of experimental uncertainties. According to Figure 3.7, the input parameter are subjected to large number of intensive (specific)

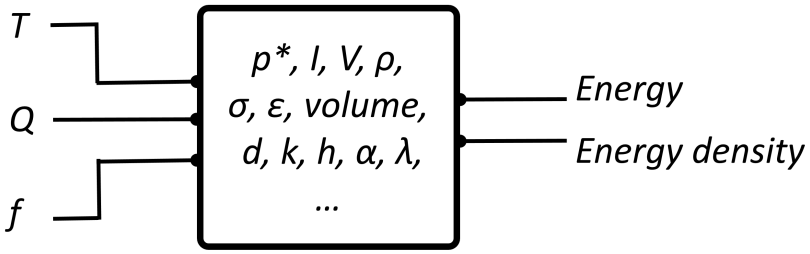

Fig. 3.7 Input and output uncertainty parameter.

and extensive (quantitative) property changes affecting the transformed energy and energy density. Potential uncertainties are as follows:

1. temperature is subject to constant changes (relative vs. absolute).
2. material purity, manufacturing technique.
3. changes in material geometry (bulk, thin film, deposition technique).
4. high voltage leakage currents.
5. low current induction ('noise').
6. non-planar uni-axial heating.
7. thermal and electrical poling history.
8. light beam spread and sample size.

According to the temperature measurement for pyroelectric energy harvesting, the transient change in temperature determining the conversion effectiveness of a pyroelectric generator is required for the analysis rather than the absolute temperature level. Indirect contributions due to day and night time temperature fluctuations (over 24 hours) are assumed to be relative small compared to the temperature oscillations selected for testing. Alternations in material conditions as well as geometry were reduced by testing each industrially procured batch electrically (impedance spectroscopy) and mechanically (measuring the dimensions) in order to ensure constant properties. With respect to the high voltage leakage currents and low current noises, the corresponding electric circuit in Figure 3.1 shows a common ground for each component used in the experimental set-up in Figure 3.1 ensuring the elimination of stray electric charges. In order to reduce the likelihood of changes in uni-axial heating and light beam spread, the test specimen dimensions were tailored and significantly smaller than the light bulb size.

Chapter 4

Manufacturing of meshed electrodes

4.1 Introduction

Micro- and nano-photolithography manufacturing techniques enable novel device architectures improving feature density, aspect ratio and the use of innovative materials. When adopted for polymers, challenges arise due to the highly non-isotropic and flexible nature of the materials. Here, the photolithography manufacturing process of meshed electrodes on PVDF is presented along with the electro- and chemical-characterisation required for energy harvesting devices. The effects of poling are studied and the meshed electrode structure fully characterised.

4.2 Materials enhancement

From equation 2.5, one way to increase the pyroelectric current generated by a pyroelectric device of a specific surface area is to improve the pyroelectric coefficient $p*$. Improvements in the pyroelectric energy transformation of PVDF based materials has led to the development of trifluorethylene (TrFE) co-polymers in order to resist higher poling fields, increase dipole strength and improve chain alignment of the β phase. This leads to higher pyroelectric coefficients in the range of 49 – 51 $\mu Cm^{-2}K^{-1}$ [117]. Additionally, solvent purification lead to a slightly higher pyroelectric response and provides a higher ferroelectric to paraelectric phase transition temperature for PVDF-TrFE, which is beneficial for harvester operating at high temperatures [75]. In addition, blending of PVDF with polymethyl methacrylate (PMMA) an additionally higher transition temperatures but reduces the level of crystallinity and lowers the pyroelectric response [118]. Potentially, there are more dopants available which might improve composite materials for electric energy harvesting. Another approach towards

improved flexible pyroelectrics is the formation of polymer-ceramic composites, combining high pyroelectric activity of pyroelectric ceramics with the high elastic properties of polymers. Composites of non-electroactive polymers (e.g. PDMS) with pyroelectric active PZT [116], as well as pyroelectric active polymer with pyroelectric active ceramics are possible [119]. With a relatively small volume fraction of 20 % PZT, the composite material provides a remarkably high pyroelectric coefficient of 92 $\mu Cm^{-2}K^{-1}$ [120]. However, polymer composites are from a thermal perspective like pure pyroelectric polymers and limited to temperatures below 90 ºC. Materials with a nano-scale geometry exhibit a high pyroelectric coefficients of 68 $\mu Cm^{-2}K^{-1}$ in the form of a PVDF-TrFE copolymers in a dense nano-fiber array [121]. Piezoelectric P(VDF-TrFE) polymer harvester with micro-patterned PDMS carbon nanotubes composites and graphene nanosheets potentially improve heat-transfer and -diffusion in a harvesting device and therefore improve the thermal to electrical conversion [122]. Other geometry optimisations approaches improving the effective pyroelectric output is the introduction of porosity [123]. Employing novel manufacture technique for pyroelectrics, a second phase is established in the pyroelectric active material modifying the electric as well as the mechanical properties of the harvester. According to equation 2.17, PVDF foams enable higher weight energy densities leading to better energy harvesting devices [124].

4.3 Heat transfer enhancement

From equation 2.5 the second way to increase the pyroelectric current, generated by a pyroelectric device of a specific surface area, is to improved the exchange of heat. Improving the thermal conductivity and the diffusivity effectively improves dT/dt in a pyroelectric system [125]. Structural changes aim to improve the utilisation of the available heat source and therefore improves the generator thermal to electrical energy transformation efficiency. For radiative heating, the replacement of a fully covered electrode with a partially covered electrode (PCE) increases the thermal diffusion because of the higher radiation absorption coefficient of the pyroelectric material compared to the conventionally used metallic electrode [126]. For pyroelectric applications, the use of symmetrical meshed electrodes [112] or non-symmetrical woven electrodes [127] has the potential to improve the available thermal conduction [128], convection and radiation [129] into the ferroelectric and therefore can enhance the effective change in temperature ΔT, or rate of change in temperature ($\Delta T/\Delta t$) [130]. Figure 4.1 shows a schematic of a pyroelectric material and the meshed electrode structure with equally spaced squares on the upper electrode. When subjected to thermal radiation, a fully covered metallic electrode acts to reflect the radiation but with partially covered meshed

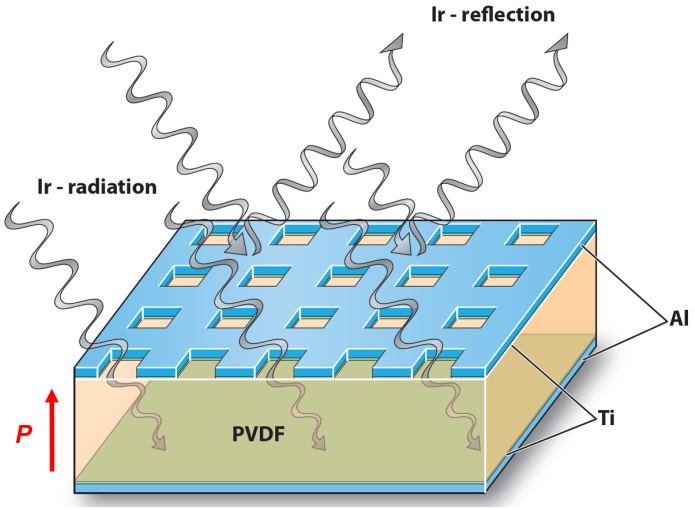

Fig. 4.1 Pyroelectric generator with partially covered meshed electrode exposed to IR radiation [131].

electrodes employed, the pyroelectric materials are directly exposed to the IR heat radiation source due to the presence of openings in the reflective electrode, so that the pyroelectric material gets directly heated. This effect is illustrated by a decreasing amplitudes of the irradiation arrows in Figure 4.1 when the radiation beam hits the electro active materials (here: PVDF). Consequently, the pyroelectric active materials with a meshed electrodes have the potential to achieve a higher absolute change in temperatures (and therefore higher open circuit voltages) and faster- and higher-rates of change in temperature (and therefore higher closed circuit currents) [131].

In this work the methods for the fabrication of partially covered or meshed electrodes on PVDF films and an investigation of benefits of such an electrode structure for pyroelectric energy harvesting are presented [115]. Despite a relatively low FOM in comparison to PZT or PMNN-PT, PVDF is of particular interest for energy harvesting due to the outstanding features of unique mechanical and weight properties are outperforming all other pyroelectric materials in terms of energy harvesting device applicability and costs (equation 2.17). On the one hand, the synthesised polymer is biocompatible but not bio-compostable, for which reason PVDF causes controversy. Since there is only a very limited number of flexible and low cost pyroelectric materials, PVDF is showing the best flexible and stretchable performance, costs and durability. In addition, PVDF is of great interest for hybrid piezo- and pyro-electric devices since it can be elastically deformed to high strains [121]. For pyroelectric thermal sensors, where the pyroelectric active materials is attached to a substrate, temperature field simulations show the negative influence of a thermally conductive substrate on the pyroelectric response, since it acts as a heat sink [132]. Based on the complex

and transient temperature profile in pyroelectric media during heating or cooling, thin film geometries are desirable, such as thin films of PVDF [100]. For radiative heating, the use of black surface electrodes shows only a marginal impact on heat transfer characteristics [133]. For pyroelectric sensor applications, substantial improvements in pyroelectric response were achieved by introducing a partially covered electrode (PCE) design on a ZnO material. The use of partially covered electrodes (PCEs) in pyroelectric sensors applications show a four times higher voltage response at a 50 – 65 % electrode area coverage [134] when compared to the fully covered Gold/Chromium electrode material that was employed. The improved heat transfer with PCEs in this system stemmed from the fact that ZnO has a higher radiation absorption coefficient compared to the gold/chromium electrode material used. Numerical solutions of the heat transfer equation (equation 2.27) confirmed a higher and faster heat flow across the material for different shapes of upper electrodes [125]. For film type devices, the pyroelectric response is four times higher with PCEs on a 3 μm thick ZnO due to the enhanced heat transfer [135]. Hsiao et *al*. revised this approach by adding 10 *nm* nickel layers on top of the uncovered ZnO leading to a higher voltage responsivity [136]. For lithium tantalite ($LiTaO_3$) a patterned PCE approach by etching three dimensional geometries into the pyroelectric material achieved a 1.5 times higher voltage response and improved the signal to noise ratio for sensing applications [137]. Considering three dimensional geometries, Hisao et *al*. adopted this approach for pyroelectric energy harvesting using PZT. When analysing the mesh width of (100 x 100) μm^2 and the etching depth of 15 μm in bulk PZT, the thermal diffusion across the material depth improved by 40 % [128]. The thermal diffusion further improved by 110 % for an etching depth between 50 and 150 μm. Additional improvements were achieved by decreasing the mesh width of a PCE from 100 μm to 30 μm for ZnO [137]. Alternative patterned electrode geometries of rectangular-, web- or criss-cross type on ZnO where shown to lead to improvements in heat transfer of around 28 % for the web type geometry [138]. Considering a spiral or vortex type electrode on PZT, where the electrode contact forms a loop with spacess, the rate of change of temperature improved by 53.9 % compared to the fully covered design [107]. Therefore, a PCE on PVDF is a simple and effective way to improve the energy generation capability of a pyroelectric energy harvester.

4.4 Modelling emissivity of aluminium meshed electrodes on PVDF

Despite the relatively low pyroelectric coefficient of PVDF, the material has attracted attention for pyroelectric harvesting due to to the low permittivity providing a high energy density for energy harvesting. The unique mechanical and weight properties are outperforming all other pyroelectric materials and makes them suitable for hybrid pyroelectric generators where the pyroelectric response is enhanced by the piezoelectric effect [38]. Therefore, PVDF is employed in this work for thermal energy harvesting with meshed electrodes in order to enhance the conversion efficiency of a pyroelectric energy harvesting system. Since the material is stable up to about 80 ℃, low temperature radiative heating experiments cover the majority of the available ambient heat source temperature levels. This work aims for a light, flexible, high strain and cheap electrode, aluminium shows the best trade-off between weight and electrical conductivity at highly competitive costs. In particular, the low temperature deposition techniques suits the 80 ℃ temperature threshold for PVDF. According to Kirchhoff's law (equation 3.10), the absorbance of radiation with PVDF is higher across all the available wavelengths than with aluminium. Utilising the higher absorbance coefficient of 0.4 with PVDF, the available radiation energy can be transformed into a greater change in temperature followed by a higher pyroelectric output [139]. With a local absorption maximum at 700 *nm*, PVDF largely absorbs solar IR radiation [140]. In contrast, aluminium has a reflective nature. Measurements for evaporated aluminium on glass (for UV and IR at 800*nm*+) show a local minimum for reactivity between 650 and 1100 *nm* of 0.12 (min. at 820 *nm*) [141]. For shorter wavelength irradiation beyond the visible spectrum, evaporated aluminium becomes more reflective [142], taking into account the natural oxide layer on aluminium. Based on equation 3.8, 3.9 and 3.10, Figure 4.2. shows a simple thermal radiation model for a 84 % meshed aluminium PVDF when exposed to a constant radiation source. Compared to a fully covered aluminium electrode, four windows have been removed from

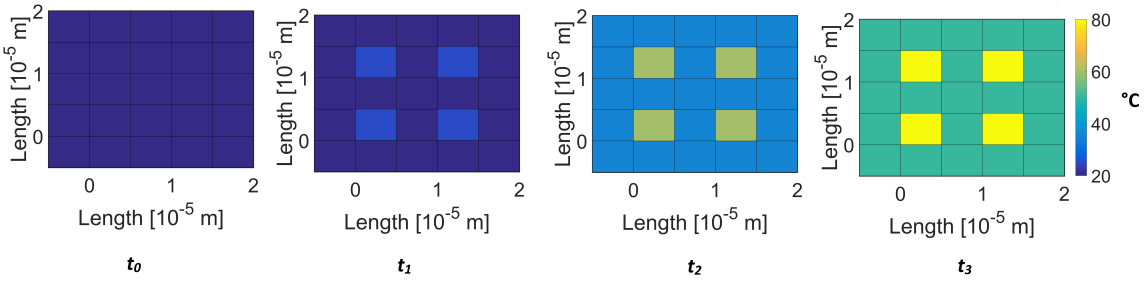

Fig. 4.2 Emissivity model for PVDF with meshed aluminium electrodes.

the surface creating an equally spaced mesh in order to heat the PVDF around the directly exposed areas. Starting with a meshed device at thermal equilibrium (t_0 and T = 22 ºC), the effective change in temperature for the arbitrary time steps t_1, t_2, and t_3 is higher for the directly exposed PVDF than for the aluminium electrode. For this reason, the spatial thermal diffusion with thickness (equation 3.7) is also higher. This leads to the conclusion, that more 'windows' in the aluminium electrode enable a larger average change in temperature. In addition, since the thermal conductivity is a function of heating time and device architecture, smaller spaces between the aluminium covered areas also lead to a faster thermal dissipation. Consequently, the mesh has to be made as small as possible. For this reason, a coarse series of meshed electrodes is manufactured and experimentally characterised for pyroelectric energy harvesting. The goal of this study is to experimentally prove the heat transfer improvements with meshed electrode and quantify the benefits of these structures for energy harvesting with PVDF.

4.5 Manufacturing of meshed electrodes on free standing PVDF

A prepoled extruded 52 μm PVDF film (Precision Acoustics, UK) was used to manufacture the device for pyroelectric harvesting. Since the PVDF is in corona pre-poled condition, there is a need to preserve the ferroelectric and mechanical properties of the PVDF by limiting the number of manufacturing steps and ensuring each fabrication step has been carried out at temperatures of less than 60 °C. This is well below the maximum useable temperature for PVDF of 75 – 80 °C [143]. Initially, a Ti (2 *nm*)/Al (200 *nm*) electrode was deposited on one side of the prepoled extruded PVDF film using a sequential electron beam vapour deposition system (Edwards FL - 400) while maintaining the temperature in the vacuum chamber below 38 °C. This vacuum thin film metal deposition manufacturing technique ensures high purity uniform electrodes providing excellent thermal and electrical conductivity required of efficient pyroelectric devices. The 2 *nm* bonding layer of titanium, measured using a parallel correlating thickness reference crystal in the chamber, was introduced in order to prevent pinhole generation, oxide formation, strip breaks, nanocracks and to improve adhesion with the polymer film [144]. Microfabrication of meshed electrode was controlled using a direct laser writing process with a positive photo-active resist. Direct laser writing was employed since it is a versatile technique that allows exploration of a variety of electrode pattern geometries, fill factors, and shapes. Figure 4.3 is a schematic of the four main manufacturing stages, starting with the deposition of a 2 μm thick AS1512HS photoresist (MicroChem-

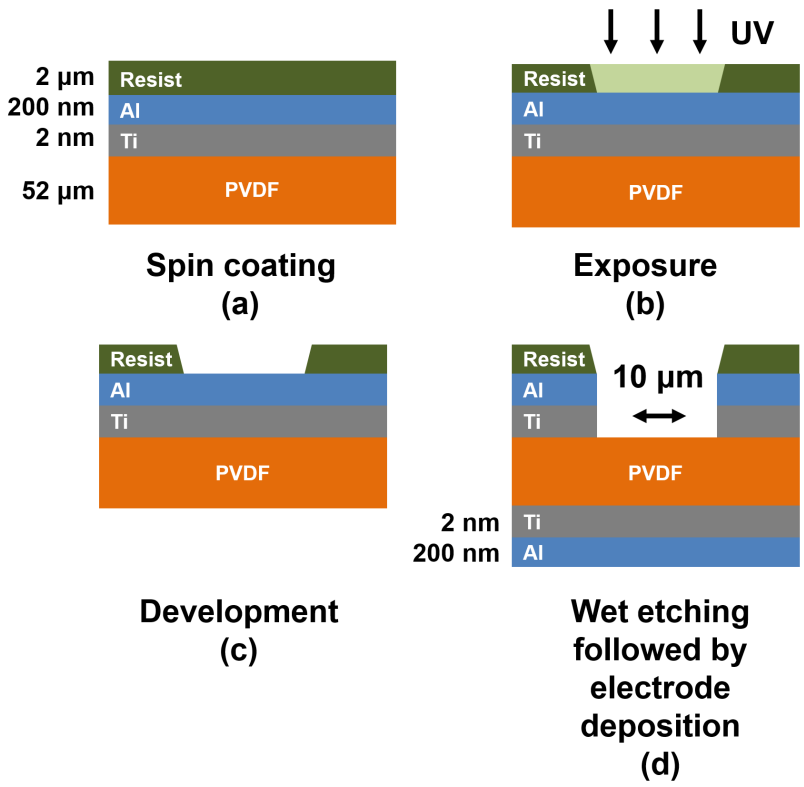

Fig. 4.3 Manufacturing steps of micropattern on Al (200 nm)/Ti (2 nm)/PVDF pyroelectric harvester. a) Spin coating of photoresist, b) UV exposure of laser exposed micropatterned surface, c) resist removal and development, and d) wet etching of aluminium to expose PVDF followed by second electron beam vapour deposition of back electrode [115].

icals - Germany) layer by spin coating (Figure 4.3 a). The photoresist was spin coated at 50 s^{-1} and soft baked on a hot plate for 45 min. at 55 °C. The free-standing PVDF film was held on a carrier glass during the fabrication process in order to maintain flatness. A direct laser writer (Heidelberg μPG 101 - Germany) was used to expose a (10 × 10) μm^2 square pattern array on a (2 × 1.5) cm^2 surface (Figure 4.3 b). The exposed photoresist was then dissolved in an AZ developer (MicroChemicals - Germany), revealing the aluminium surface and the remaining resist was hard baked for 30 min. at 55 °C (Figure 4.3 c). The exposed aluminium was then etched away by a wet etching process using an etchant solution (H_3PO_4:HNO_3:CH_3OOH:H_2O) for 2 min. (Figure 4.3 d). The PVDF is reported to be resistant against these acids [140]. Finally, the remaining resist was removed with acetone and the PVDF film peeled off the handling glass substrate. The non-patterned backside of the device was electroded after etching using a second Ti (2 *nm*)/Al (200 *nm*) backside electrode electron vapour deposition (Figure 4 d). The corresponding recipe with a detail timing is provided in Appendix B 1. Due to the highly flexible manufacturing process, the electrode surface area was decreased by a gradual increase in the number of etched squares per unit area so that devices with electrode coverages of 91 %, 88%, 70%, 53%, 45%, 28%, and 19% were fabricated. According to equation 2.8 and 2.10, the electrode area of a parallel plate capacitor with meshed electrodes for pyroelectric energy harvesting is defined as the total surface area (A) perpendicular ($\perp$) to the average ferroelectric polarisation (P) moment (Figure 4.1) subtracted by the surface area (here squared windows) directly exposed to the IR radiation beam:

$$\text{Electrode coverage} = A_{\perp,P} - A_{\perp,P} \text{ directly exposed to IR radiation} \tag{4.1}$$

The fully electrodes surface area of the PVDF film therefore represents 100 % coverage as a reference. This definition applies for the experimental results reported as well as for the modelling conducted in this work. Figure 4.4 provides a picture of the manufactured film type harvester with a surface area of 2.0 *cm* x 1.5 *cm* and a coverage of 50 %.

4.6 Material characterisation of PVDF-meshed electrodes

The pyroelectric activity of the non-electroded PVDF film was measured by Fourier transformation infrared (FTIR) spectroscopy using a PerkinElmer Frontier (USA) of the employed industrially extruded ferroelectric PVDF film which indicates that the PVDF is in its β-phase with a distinctive specific absorption peak at 839 s^{-1} [142]. Figure 4.5 shows the wavelength admittance between 600 and 1500 cm^{-1}. For the electrode PVDF film, FTIR cannot be used for which reason other measurement techniques like polarisation-electric field, piezoelectric

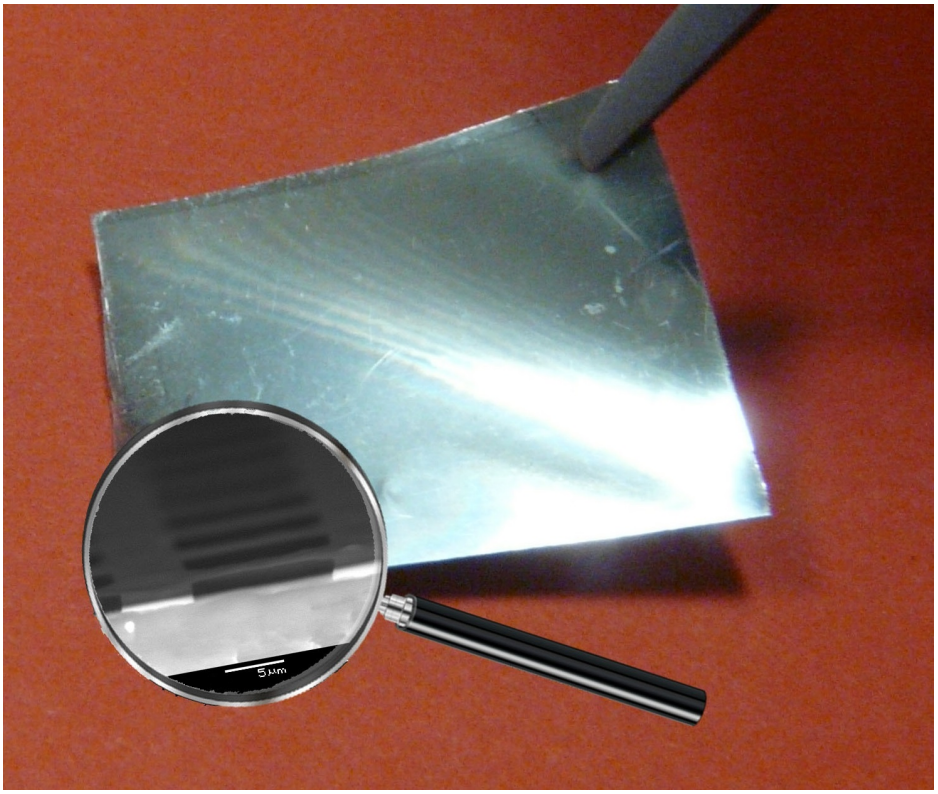

Fig. 4.4 Image of the (2x2) cm^2 pyroelectric device with x 4000 magnification [115].

testing, or pyroelectric testing need to be conducted. In this study, prepoled- as well as electroded poled-meshed PVDF device are characterised.

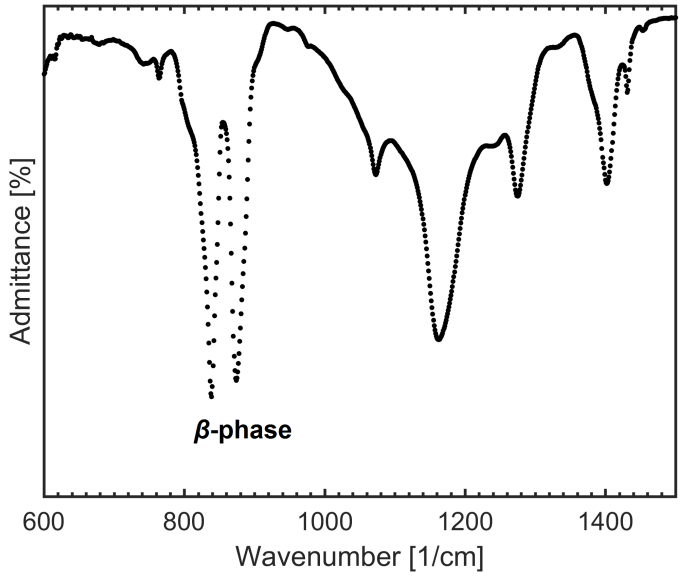

Fig. 4.5 Emissivity model for PVDF with meshed aluminium electrodes [115].

Since the pyroelectric device is fully electroded and poled, the meshed-electrode PVDF pyroelectric device manufacturing quality needs to be examined. Scanning electron microscopy (SEM) (Raith ELPHY Plus) planar images are provided in Figure 4.6 showing examples of the PCE mesh for surface area coverages of 70%, 45%, and 28%. The defect free homogeneous distribution proves the suitability of the laser writing and wet-etching manufacturing techniques for free standing PVDF films. The inset in Figure 4.6 shows

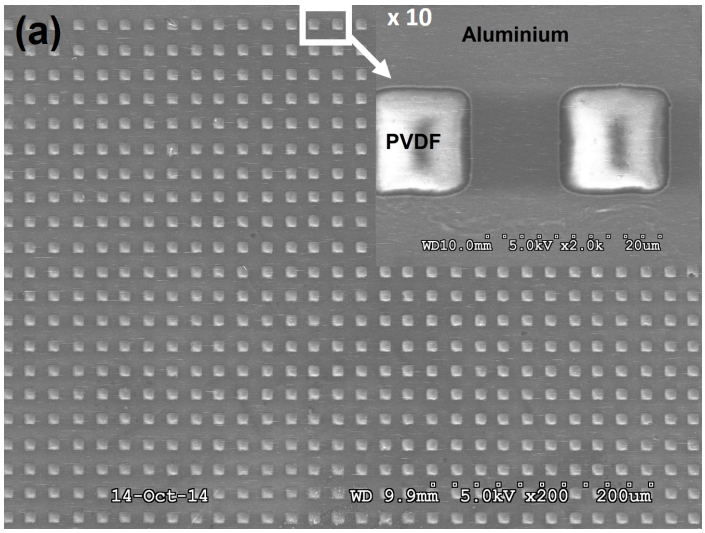

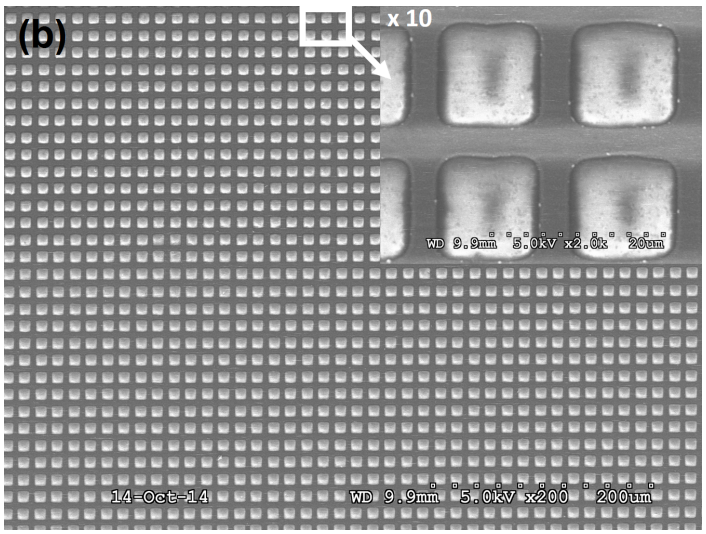

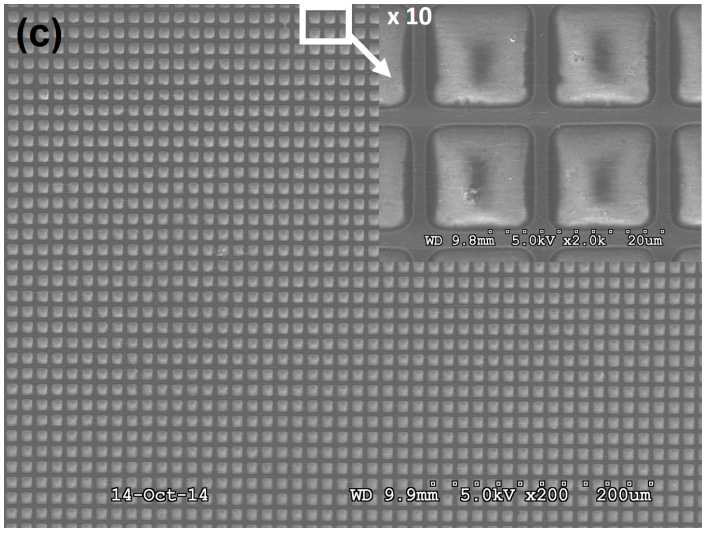

Fig. 4.6 Examples of PCE with surface coverage of 70% (a), 45% (b), and 28% (c). The darker area is the aluminium electrode and the lighter area is the exposed PVDF.

a x 2000 magnification of the scanned surface area. A thick mesh with 70% coverage has only two etched squares (Figure 4.6 a) whereas a thin mesh with 28% electrode coverage has around six etched squares for the same surface area of PVDF (Figure 4.6 c). The uniformity of the etched square size as well as square quality was maintained constant for the total surface device area of (2 × 1.5) cm^2. Appendix B.2 shows a single etched square image on the PVDF film with a x 5000 magnification. Since the planar view of the

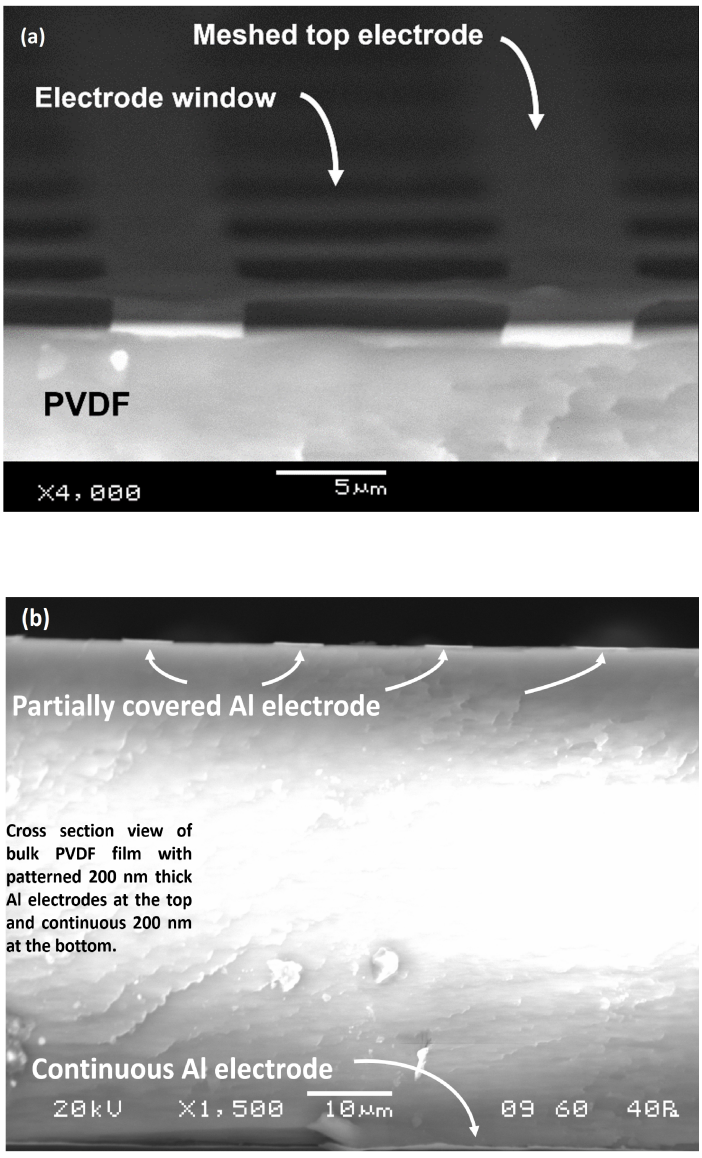

Fig. 4.7 Off-axis (angled) view (a) and cross section view (b) of a PCE with surface coverage of 45 [131].

meshed electrode does not reveal any defects, a cross sectional views of the architecture provides an insight into the etching process. SEM images (JEOL SEM6480LV) of a 45 % covered meshed electrode sample are provided in Figure 4.7. The off-axis view in Figure 4.7 (a) reveals no damage to the PVDF with a homogeneous etched meshed electrode. The cross-sectional view in Figure 4.7 (b) shows the patterned aluminium top electrode on PVDF with the fully covered (continuous) bottom electrode. Therefore, it is concluded that the low temperature-wet etching manufacturing process does not affect the PVDF film. However, in order to prove the meshed electrode nature (elemental analysis) and properties (geometry), energy-dispersive x-ray (EDX) spectroscopy measurements were conducted. According to the surface area, exposed to the election beam in Figure 4.6 (a-c), Figure 4. 8 shows the EDX surface reflection. The measurement was conducted using an EDX measurements (Oxford INCA X-Act SDD) x-ray detector. Distinctive peaks for carbon (C),

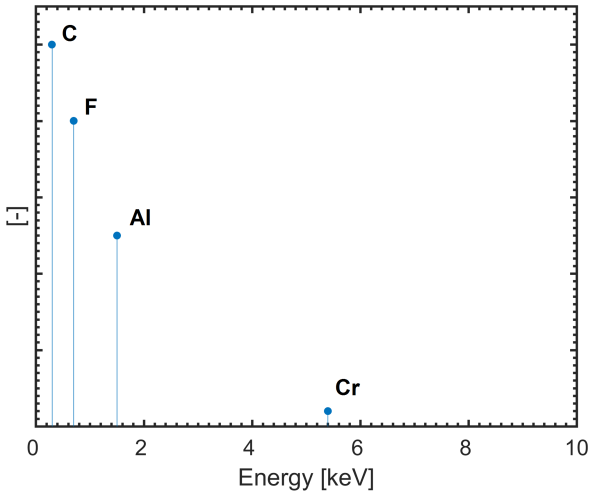

Fig. 4.8 EDX for aluminium meshed top electrode on PVDF.

fluoride (F) aluminium (Al), and chromium (Cr) reveal a complete removal of the titanium bonding layer. As a second reference measurement, 50 % of the scanning area is positioned free standing (on an aluminium sample holder) and the other 50 % of the area is the meshed electrode area of interest. Figure 4.9. shows for the highlighted area (blue window) and the corresponding response across a wide range of x-ray energy intensities.

According to Figure 4.9, the EDX surface scan shows a sharp line between the mesh electrode PVDF and the free standing reference. For the electrode window, a high carbon and fluoride concentration present with decreasing concentration for the mesh electroded area. In contrast, a high aluminium is present at the meshed area with a sharp decrease for the free electrode window (aluminium sample holder is correctly assumed high aluminium

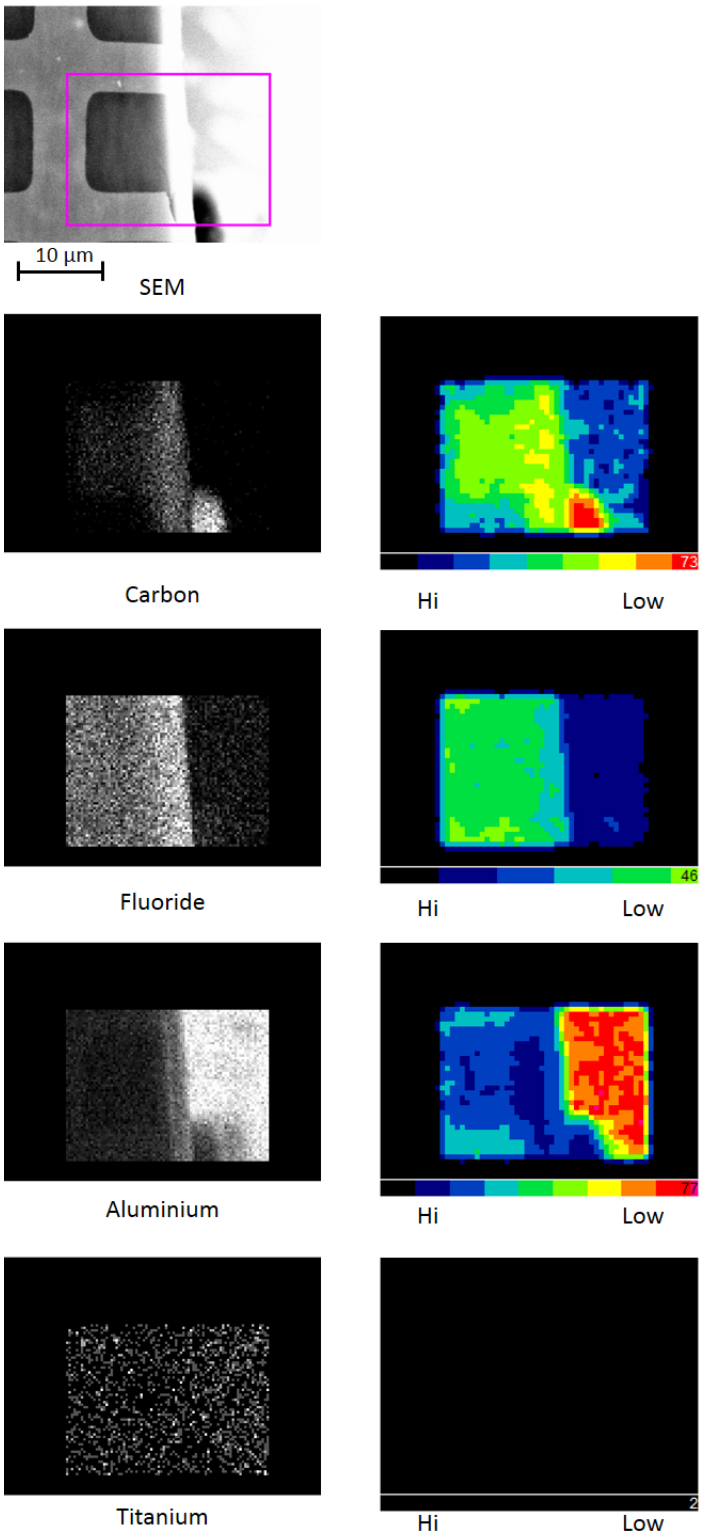

Fig. 4.9 EDX visualisation for aluminium meshed top electrode on PVDF.

intensity). For etched aluminium/titanium area, no titanium was detected with constantly low values for reference and meshed area.

4.7 Electro-chemical characterisation of PVDF-meshed electrodes

When employing meshed electrodes, there is a potential to form a non-uniform electric field distribution throughout the device. This is experimentally verified by measurement of the ferroelectric hysteresis loops (P-E loops) and capacitance to characterise the average macroscopic polarisation, which includes the non-electroded areas of the mesh in Figures 4.1. Using a Sawyer-Tower circuit, a 1 Hz and 10 kV triangle wave was cycled from positive to negative in order to record the remnant polarisation using a aixACCT (Germany) PES test system with the sample immersed in Dow Corning (US) silicone fluid during the test [131]. The applied electric field - polarisation was measured for 25 %, 43 %, 76 %, 91 % meshed- and fully covered 100 % reference electrodes on the previously reported PVDF films until dielectric breakdown at around 2 $MVcm^{-2}$ occurred [115]. For pyroelectric systems, which require a change in temperature in order to develop a potential difference, the temperature dependence of the material properties as well as the high electric field hysteresis loops with PVDF were studied by heating the test chamber to 50 ºC [145]. Piezoelectric strain - electric field was measured for a 52 μm thick PVDF film on a fully covered electrode geometry using an aixDBLI double beam laser interferometer at the centre of the sample. For energy harvesting it is important to understand the dominant source capacitance and peak voltage of the pyroelectric element with meshed electrodes in order to account for the transformed energy (equation 2.9); for example in equation 2.8 which is the parallel plate assumption and the source capacitance in Figure 4.1. For this reason, electrostatic macroscopic polarisation for the 25 %, 43%, 76%, 91% and 100 % covered meshed electrodes was measured on (10 x 10) mm^2 samples in Figure 4.10 (a). Constant values for remnant polarisation (P_r = 6 μCcm^{-2}) and coercive field (E_c = 750 $kVcm^{-1}$) with decreasing surface coverage were observed up to electric fields of 1950 $kVcm^{-1}$; at higher field electrical breakdown was observed [115].

When recovering electrical energy from heat, the temperature changes developed and the change in dipole moment due to pyroelectric effects, the permittivity and the nonlinear dielectric behaviour are of interest [77]. Under moderate thermal conditions below 80 ºC, PVDF is of particular interest for pyroelectric energy harvesting applications due to the low relative permittivity and high thermal conductivity followed by a high volumetric energy

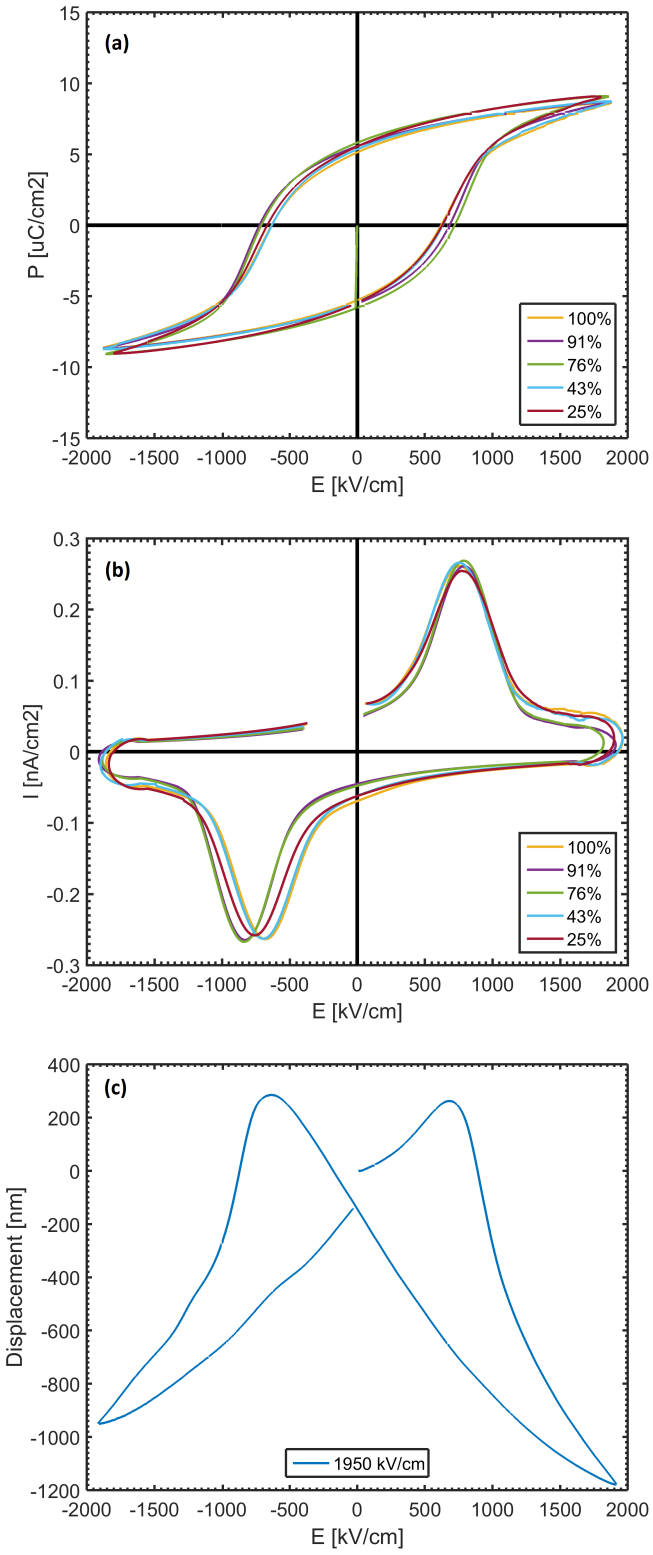

Fig. 4.10 (a) Ferroelectric polarisation - applied electric field (P-E) loop of PVDF with various meshed electrode areas (b) current – applied electric field (I-E) loop for various meshed electroded (c) and piezoelectric displacement of PVDF with fully covered electrode for externally applied electric field [131].

density when manufactured in thin films and large areas [37]. In Figure 4.11, the $P-E$ loop of PVDF for a fully covered electrode between a room temperature of 25 ℃ and 50 ℃ are compared to assess the change in properties for this particular temperature range where changes in ambient temperature for pyroelectric harvesting are likely. The coercive field decreases slightly (from 750 $kVcm^{-1}$ to 700 $kVcm^{-1}$) with an increase in temperatures, as does the remnant polarisation. According to equation 2.2, the calculated change in polarisation P for a performed change in temperature ΔT of 25 ℃ with PVDF is 82 nC for a 1 cm^2 PVDF film ($p* = 25\ \mu Cm^{-2}K^{-1}$) [38]. Under elevated temperatures, the coercive field decreases because the molecular mobility increases with temperature improving ferroelectric switching. The intrinsic electro-mechanical and -thermal properties of PVDF

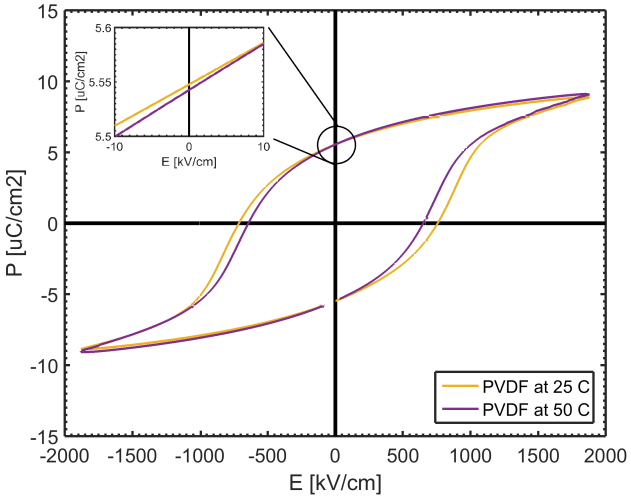

Fig. 4.11 Ferroelectric polarisation – applied electric field ($P-E$) loop for PVDF with fully covered electrode at room temperature and 50 °C.

have a great potential for energy harvesting systems. For the meshed electrodes considered in this work the polarisation-field ($P-E$) and current-field ($I-E$) characteristics are unaffected since the fringing fields were generally small.

4.8 Conclusions

Heat transfer enhancement for pyroelectric energy harvesting with meshed electrodes has the potential to improve energy density and peak power output. Here, meshed electrodes with a novel aspect ration on a flexible pyroelectric PVDF showed a constant ferroelectric behaviour despite a decreasing electrode surface coverage. Compared to standard fully covered aluminium electrodes, the openings in the electrode enable a direct heating of the

pyroelectric active material followed by an improved thermal- to electrical-energy conversion. Chapter 5 will present experimental heating measurements based on constant thermal boundary conditions for pyroelectric energy harvesting with meshed-electrode on PVDF.

Chapter 5

Meshed electrodes for pyroelectric energy harvesting

5.1 Introduction

Heat transfer enhancement for pyroelectric energy harvesting provides a new route for higher efficiency, higher energy density and higher peak power with pyroelectric harvesters than non-optimised systems. For the first time the full range of meshed electrode coverages is experimentally analysed providing a peak power at 45 % electrode coverage with a corresponding energy improvement of 1050 % compared to a standard aluminium electrode design.

5.2 Pyroelectric response of meshed PVDF devices

For pyroelectric electrical energy harvesting characterisation, meshed PVDF films were exposed to a cycled infra red (IR) light beam of 293 $mWcm^{-2}$ heating power operating at a switching frequency of 0.05 Hz in order to establish harmonic temperature oscillations with constant average temperatures. When the beam was switched on, IR radiation perpendicularly hits the meshed electrode surface area, thereby heating the PVDF film. When the beam was switched off, natural convection cooled the PVDF film. For cyclic heating, the transient open circuit voltage and closed circuit was recorded using a Keithley (US) 6514 electrometer (calibrated in 2015) with an input impedance of 200 $T\Omega$ and a sensitivity of 10 pA [131].

Figure 5.1 (a) shows temperature variation with time for PVDF with different electrode coverages, along with a fully covered electrode (100 %) for comparison. From Figure 5.1 (a) it

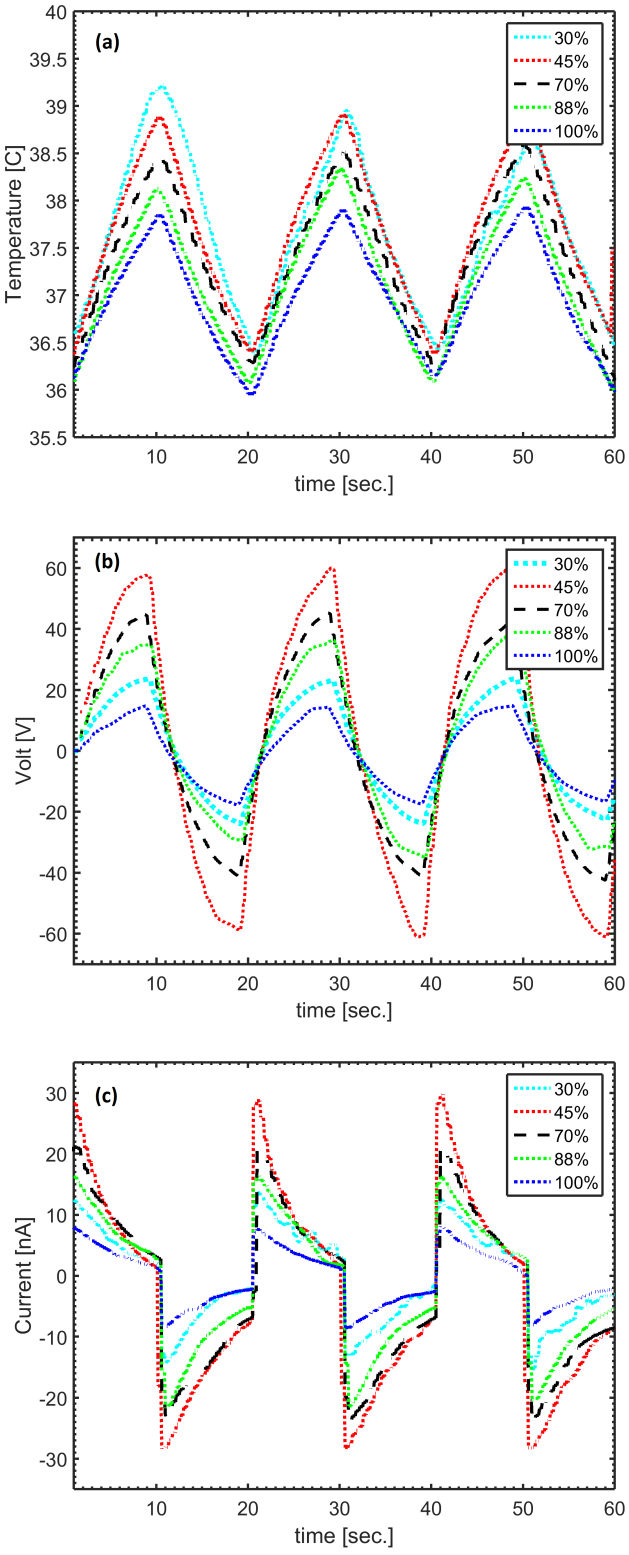
(a)
30%
45%
70%
88%
100%
Temperature [C]
time [sec.]
(b)
Volt [V]
time [sec.]
(c)
Current [nA]
time [sec.]

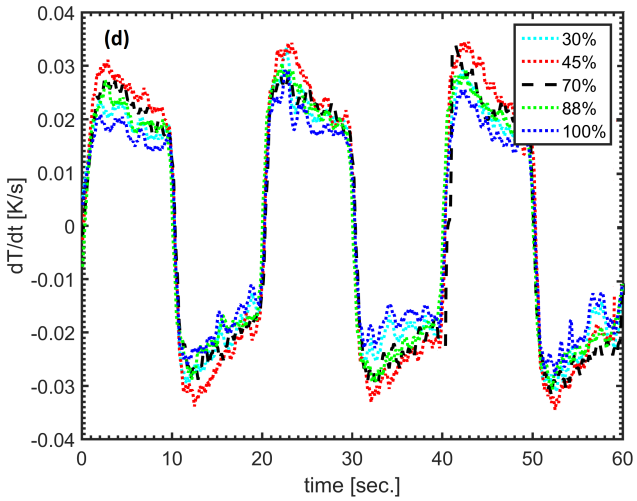

Fig. 5.1 Developed a) temperature, b) open circuit voltage, c) closed-circuit current and d) rate of change of temperature for 100%, 88%, 70%, and 45% electrode coverage at temperature oscillation of 0.05 Hz [131].

can be observed that the absolute temperature magnitude (T) and its difference (ΔT) becomes larger with decreasing surface electrode coverage. The temperature profile for a 70% PCE shows a 2.2 °C change in temperature over 10 sec., while 45% PCE results in a larger change in temperature of 2.8 °C. For identical boundary conditions, the fully covered (100%) sample temperature changes by only 1.5 °C. By measuring the developed temperature over the full range of electrode coverage (100%, 88%, 70%, 53%, 45%, 28%, and 19%), it was observed that when the PCE coverage decreases, the rate of change of temperature, dT/dt , also increases. According to equation 2.5, faster rates of change in temperature (Figure 5.1 b) lead to a larger closed circuit currents. Particularly for the early portion of each heat wave the difference in dT/dt between a patterned and unpatterned harvester is larger by 50 %. Subsequently, corresponding current measurements in Figure 5.1 d confirm the ability to increase the closed circuit current by decreasing the electrode coverages. As an example, the 70% covered electrode has a closed circuit pyroelectric current of 20 nA and when compared to the fully covered electrode that develops 7 nA for identical conditions, the enhancement in heat transfer improves the closed circuit current by 285%. Considering the corresponding open circuit transient voltage response, a larger temperature change leads to a higher voltage according to equation 2.5. In Figure 2 c, the 70% PCE develops a closed circuit voltage of 42 V which is an increase of 280% compared to the 16 V for the fully covered reference sample. Clearly the higher heating and diffusion rates associated with a PCE lead to faster thermally induced changes in polarization and develop more released charge at the electrode surface followed by a higher energy transformation. Figure 5.2 (a)

shows the pyroelectric short-circuit current and Figure 5.2 (b) open-circuit voltage for the whole range of electrode areas examined. For a 45 % PCE a peak current of 30 *nA* and a

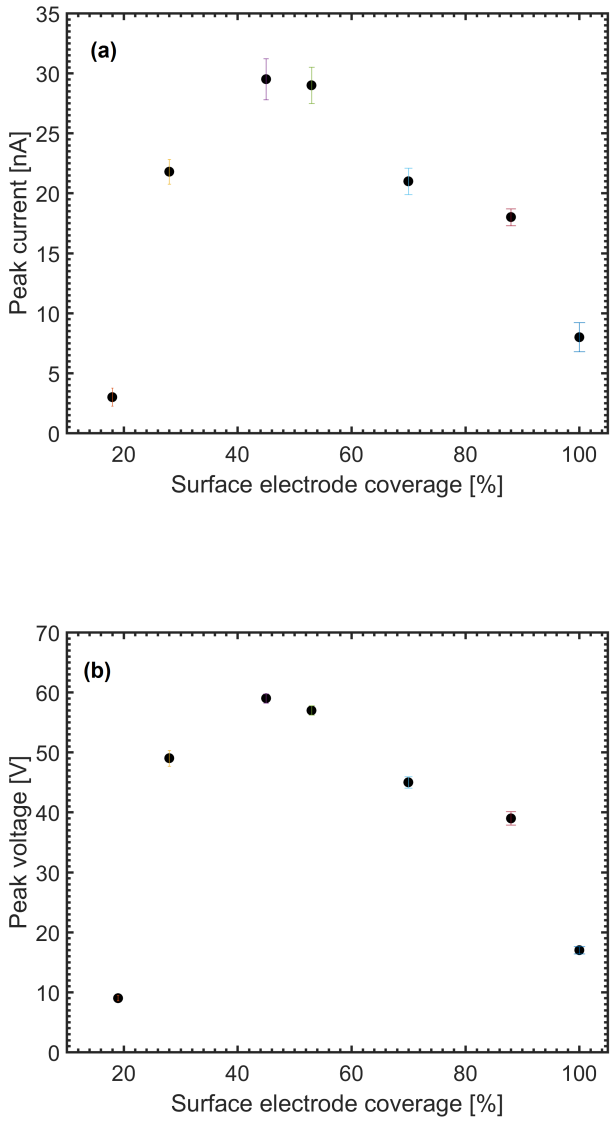

Fig. 5.2 Measured peak: a) closed circuit current and b) open circuit voltage for a range of surface electrode coverages [115].

peak voltage of 59 *V* is achieved and when compared to a fully covered electrode reference sample with a current of 8 *nA* and a voltage of 16 *V*, the 45 % PCE provides a 380 % higher voltage and a 420 % higher current. The optimisation approach shows a local maximum at 45% for the energy transformation so that further decrease in PCE coverage leads to a

deterioration of generated pyroelectric current and voltage. Ultimately the optimum PCE is a balance between the areas of electrically conductive aluminum required to collect the free charges to the exposed PVDF area to improve heat transfer [115]. For the here testes PVDF film architecture, identical energy harvesting performance was measured on industrially pre-poled (corona poling) devices with a dielectric breakdown field of 2 MVm^{-1} as well as on meshed electrode poled PVDF samples using the polarisation P - applied electric field E set-up reported in Chapter 4 of this work. The pyroelectric peak performance at 45 % electrode coverage with meshed electrodes is reported for corona poled meshed samples [115] as well as for electrode poled samples [131], showing a rapid performance decrease when the electrode coverage is being removed greatly.

Despite the increasing heat transfer performance with decreasing electrode coverage, the highly nonlinear trend shows how critical the optimisation of a pyroelectric systems is. In order to gain complete evidence, the change in polarisation generating the electrostatic field with the electrode structure needs to be studied. Since an experimental polarisation-electric field measurements in Chapter 4 do not reveal any decay with electrode coverage, a numerical finite element model can provide an insight into the electrode area of the mesh and will be described in the next section of this thesis. At this point, the 3 dimensional (3D) complexity of the structure does not allow a trivial solution.

5.3 Finite element analysis of meshed electrodes using coupled field model

The charge-voltage relationship and piezoelectric displacement with applied electric field are numerically evaluated and compared with experimental results for PVDF films in order to resolve polarisation, electric field distribution and capacitance with meshed electrodes and non-homogeneous electric fields. The specific capacitance of a (100 x 100) μm^2 and 52 μm thick element is modelled as close approximation for the meshed electrodes of area (10 x 10) mm^2 and 52 μm thick free standing PVDF films and shows the electric field patterns at the electrode corners, the edges, and the areas between the equally spaced squares in the 3D space in Figure 4.1 [145]. With the meshed electrodes modelled as two dimensional layers, the PVDF is considered unclamped. Following the piezoelectric constitutive equations for the mechanical stress σ_{ij} and the mechanical displacement D_i [65]:

$$\begin{bmatrix} \sigma_{ij} \\ D_i \end{bmatrix} = \begin{bmatrix} C^E_{ijk} & -e_{ijk} \\ e_{ijk} & \varepsilon^{ST}_{ij} \end{bmatrix} \begin{bmatrix} s_{kl} \\ E_K \end{bmatrix} \tag{5.1}$$

the stiffness matrix C_{ijk} under constant electric field E, permittivity ε_{ijk} under constant stress S and temperature T, and piezoelectric charge coefficient e_{ijk} (constant stress), was solved with the commercially available finite element analysis (FEA) package ANSYS 15. With the PVDF film poled through the thickness ('3'- or 'z'- direction), the anisotropic mechanical and electrical bulk properties for uniaxial mechanically stretched PVDF films provided by the manufacturer [144], are compared against the literature for the piezoelectric charge coefficient [65]:

$$e_{ijk}\,(CN^{-1}) = \begin{bmatrix} & & & & 0.18533 & \\ & & & & 0.008869 & \\ & & & & -0.41678 & \\ & & -0.49091 & & & \\ -0.03333 & & & & & \end{bmatrix} \tag{5.2}$$

and the elastic compliance [149]:

$$C^{E}_{ijk}\,(Nm^{-2}) = \begin{bmatrix} 3.61 & 1.61 & 1.42 & & & \\ & 3.13 & 1.31 & & & \\ & & 1.63 & & & \\ & & & 0.55 & & \\ & & & & 0.55 & \\ & & & & & 0.69 \end{bmatrix} \tag{5.3}$$

and the relative permittivity at constant stress [150]:

$$\varepsilon_r^{ST} = \begin{bmatrix} 11 & & \\ & 11 & \\ & & 11 \end{bmatrix} \tag{5.4}$$

which applies to most piezo-electric and pyroelectric systems that are free to deform (unclamped) [151]. When the piezoelectric system is clamped, constant stress permittivity for the crystallographic 3-3 direction is converted into constant strain permittivity employing the electromechanical coupling coefficient k [29]:

$$k_{33} = \frac{d_{33}}{\sqrt{s_{33}\varepsilon_{33}}} \tag{5.5}$$

satisfying most piezoelectric load conditions. The complete ANSYS source code including the input and output parameter is provided in Appendix C.1. The coupled field analysis of the PVDF film in Figure 5.3 (a) enables the analysis of the local electric field distribution around the meshed electrodes and the local piezoelectric displacement in Figure 5.3 (b) for the local electric field. For the electric equipotential in Figure 5.3 (c) the numerical solution of the inhomogeneous distribution around the top electrode shows a small fringing electrical

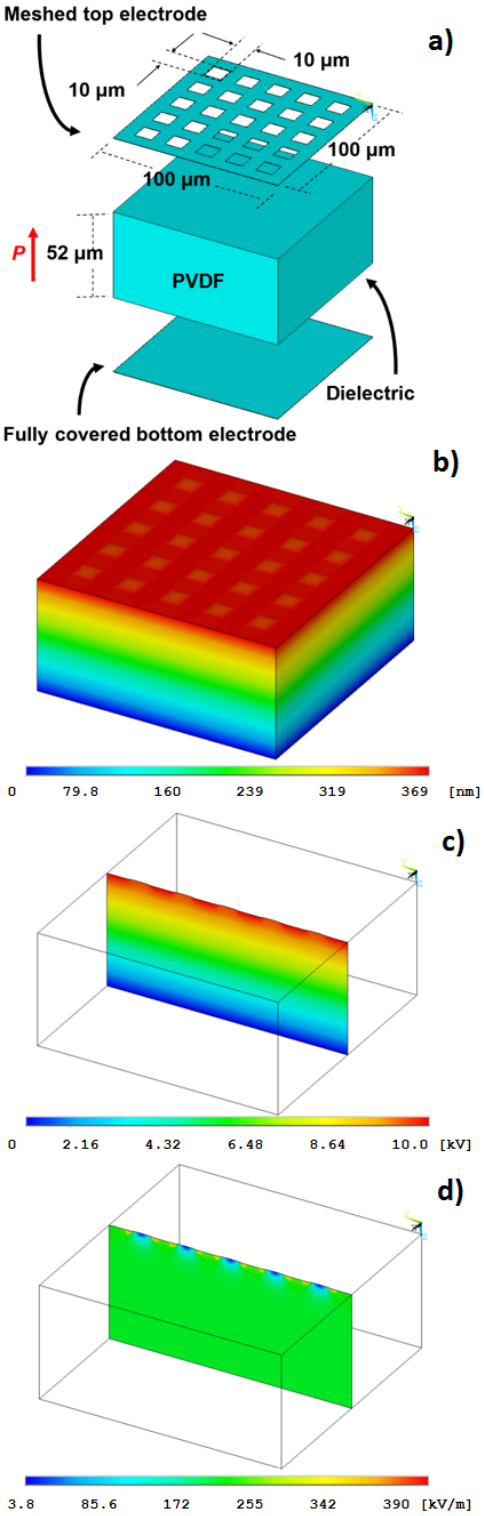

Fig. 5.3 Finite element model of meshed electrodes showing geometry (a), piezoelectric displacement (b) electric-potential through thickness (c) and electric field through thickness (d) with 75 % coverage [131].

flux in Figure 5.3 (d); this will be described in more detail later in this chapter and compared against experimental dielectric impedance spectroscopy measurements in order to determine the influence of the electrode area coverage and the aspect ratio, defined as the ratio of PVDF thickness to window dimension, on model outputs [127].

5.4 Pyroelectric energy generation with meshed electrodes

The energy density of the energy harvesting systems, and therefore the electrical capacitance, needs to be determined in order to assess the performance of different generators (equation 2.10). The small changes in $P-E$ and $I-E$ loops with increasing meshed area in Figure 4.10 indicate that a constant energy storage capability with meshed electrodes despite a decreasing electrode coverage. Therefore, electrical impedance spectroscopy (EIS) measurements (Solatron S1 1260 impedance analyser) for the 25 % to 100 % electroded PVDF films were examined to determine the change in device capacitance with electrode coverage. This section compares the measured capacitance of meshed electrodes with the numerical simulations conducted.

According to Chapter 4, small changes in the $P-E$ and the $I-E$ loops with increasing meshed area indicate a constant energy storage capability with meshed electrodes despite a decreasing electrode coverage. Based on the parallel plate assumption in equation 2.9 for the electrical capacitance, the electrical field is assumed to be parallel (ignoring fringing fields) with respect to the meshed top electrode area A. For this reason, equation 2.9 provides a linear decrease in capacitance with a decrease in electrode coverage. With the FEA model taking into account the fringing fields, dielectric and piezoelectric displacement for the applied electric field, Figure 5.4 a compares the calculated with modelled capacitance together with the experimental measurements for 25, 43, 76, 91 and 100 % covered samples. For the 100% area coverage all three approaches (measured, numerical and parallel plate) are in good agreement. However, the experimental and numerical finite element results show a slow decrease in capacitance with decreasing electrode surface coverage. Compared to the fully covered electrode, with a 18 μFm^{-2} reference capacitance, the 19 % covered electrode geometry shows only a 4 % lower capacitance for the numerical simulation of 17.28 μFm^{-2} in Figure 5.4 b [131]. The experimental results show an extrapolated reduction in capacitance of 8 %. This leads to the conclusion that the average electric field strength remains constant for the device geometry examined in this work, despite a non-homogeneous parallel plate geometry. Therefore, it is reasonable to assume that the here manufactured geometry has a constant electrical capacitance.

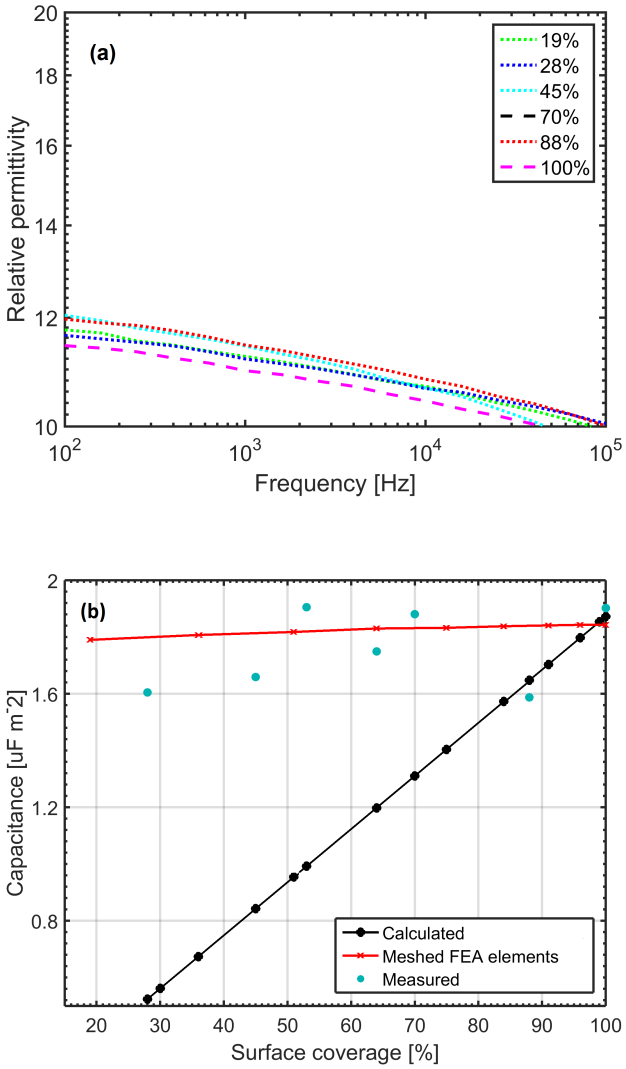

Fig. 5.4 (a) permittivity with meshed electrode and (b) variation of device capacitance with electrode surface coverage. The measured values are compared with the FEA prediction and parallel plate assumption [131].

In section 4.1, it has been demonstrated that for pyroelectric systems, meshed electrodes provide a novel approach to improve energy conversion of a PVDF energy harvesters [131]. Considering a 59 V peak voltage for the 45 % PCE and a measured capacitance of 600 pF, the energy stored in the pyroelectric element is 1.04 μJ. On a volumetric basis, the energy density is 66.9 μJcm^{-3} per thermal cycle. Finally, due to the squared relation of energy and voltage, the 45% PCE has a 1080% higher energy transformation than the fully covered reference, which only provides 6.2 $\mu Jcm^{-3}cycle^{-1}$. In addition, the generated energy of the patterned device corresponds to a harvesting effectiveness k^2 of 0.19 % for a volumetric heat capacity of 1.8 $Jm^{-3}K^{-1}$, relative permittivity ε_r = 11, pyroelectric coefficient of 33 $\mu Cm^{-2}L^{-1}$ and source temperature of 39 °C [40]. The 66.9 μJcm^{-3} of micropatterned PVDF is smaller than a measured energy density of 420 μJcm^{-3} for PZT at approximately 42.5 °C with a fully covered electrode; this is associated with the significantly higher pyroelectric coefficient of PZT compared to PVDF [148]. Measurements on a PMN-PT single crystal show pyroelectric energy densities of 149 $mJcm^{-3}$ at temperatures slightly above room temperature [40]. Therefore, the improvements associated with micropatterned PVDF approach provides a route for flexible and low cost pyroelectric harvesters; the energy density could be further improved using a PVDF-TrFE copolymer [115].

5.5 Electric field distribution

The origin of the relatively constant device capacitance and polarisation-field loops with meshed electrode area can be explored via the numerical modelling where the meshed top electrode structure maintains the same level of charge as the fully covered bottom electrode followed by local charge concentrations and high electrical fields. Based on the FEA model for the electric flux within the ferroelectric, Figure 5.5 provides the local electric field distribution of the 2 dimensional (2-D) plane from the Figure 5.3 (d) model. The non-linear electric field lines in Figure 5.5 developed around the electroded areas of the meshed top electrode are fringing towards the fully covered bottom electrode. In contrast, the electric field strength decreases around the non-electroded areas of the meshed top electrode. Consequently, the piezoelectric displacement weakens for a lower strength electric field creating slight bumps at the surface of the PVDF film due to a lack of piezoelectric strain.

The left side of Figure 5.6 shows the electric field line in a parallel plate capacitor. The right side of Figure 5.6 shows the qualitative analogy of the fringing electric field lines from Figure 5.5. High electric fields dominate the meshes top electrode with a peak electric field strength 2.2 greater than the average field. When analysing the electric field further down towards the fully covered bottom electrode, the electric field lines becomes parallel

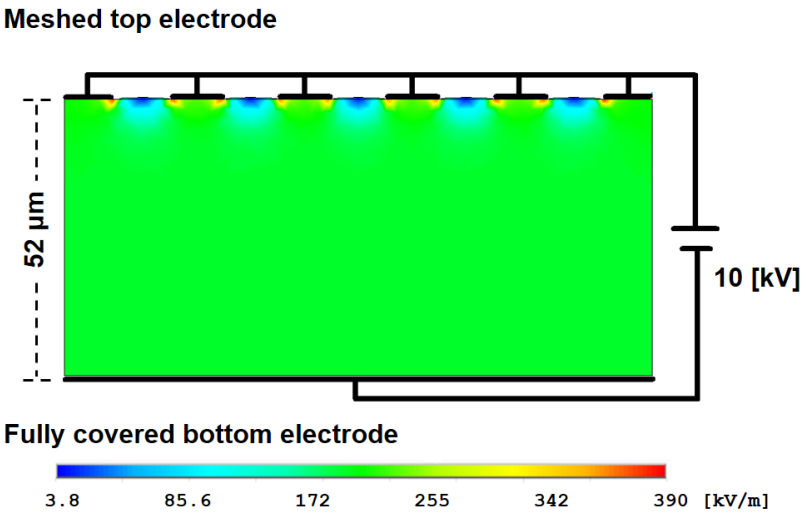

Fig. 5.5 2-D plane showing the electric field distribution through the PVDF thickness for a meshed electrodes (electrode coverage area is 75%) [131].

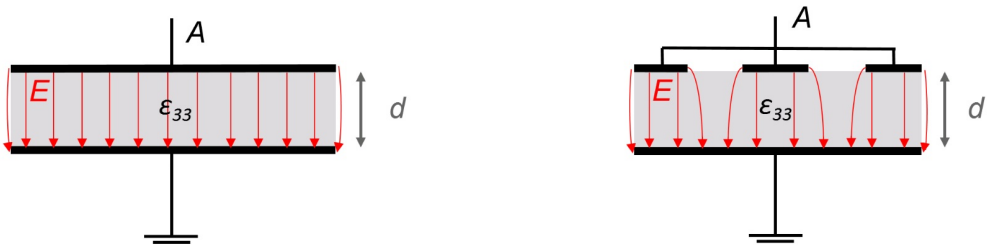

Fig. 5.6 Fringing electric fields with meshed parallel plate electrodes .

at approximately 1/10 of the dielectric thickness (52 μm) where the high 390 kVm^{-1} as well as the low 3.8 kVm^{-1} fields vanish. Where electric field lines are parallel, the parallel plate assumption and therefore the capacitance form equation 2.8 is justified. This condition is determined by the dielectric thickness d and the spacing between the conductors of the meshed electrode [148]. In this model, the aspect ratio of the dielectric thickness 52 μm to the mesh spacing of 10 μm between in the conductors relates to 5.2, for which the parallel plate assumption for non-homogeneous electrodes is a sufficiently accurate assumption. With high

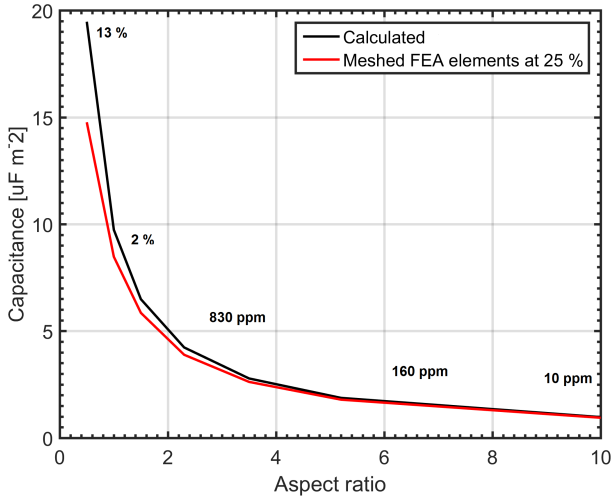

Fig. 5.7 Influence of PVDF thickness to window dimension aspect ratio on the device capacitance. The numbers indicate the difference between the parallel plate assumption and the finite element simulations [131].

aspect ratios above five, where the ferroelectric is much thicker than the electrode spacing, the parallel plate assumption provides a good approximation of the systems geometry with parallel electric fields. However, for thin dielectrics with a large electrode spacing (low aspect ratio), most electric field lines are fringing and the available capacitance decreases. Figure 5.7 shows the discrepancy between calculated capacitance assuming a homogeneous electric flux and the modelled capacitance of a meshed electrode 10 μm spacing for varying aspect ratios. For an aspect ratio of 0.5, with a dielectric thickness of 5 μm and a spacing of 10 $\sim \mu m$, the modelled capacitance of 15 μFm^2 is 25 % lower than the ideal calculated capacitance of 20 μFm^2 (equation 2.8). For larger aspect ratios, eg. greater than four, the fringing electrical fields quickly recover as well as the electrical storage capabilities of the meshed energy harvesting system [131].

5.6 Rectification and storage of pyroelectric energy

While it is of interest to characterise the improvements in open circuit voltage and short circuit current, in practical energy harvesting applications there is a need to store the harvested energy or subject the energy harvester to an electrical load. Since temperature oscillations are usually small and slow, the non-ideal pyroelecric alternating supply current (AC) is variant in time and magnitude, and for this reason some form of power conditioning is needed. In addition, most silicon based electronics require a direct current (DC) power supply requiring rectification when harvesting thermal energy with pyroelectric [131]. When optimising a pyroelectric energy harvesting systems and the device performance, the small and slow thermal oscillations are challenging. Unlike impedance matching with high resistive external loads for PVDF [153], more sophisticated Synchronised Switching Harvesting (SSH) circuits improve the systems energy conversion [77]. Therefore, in this work the electrical energy

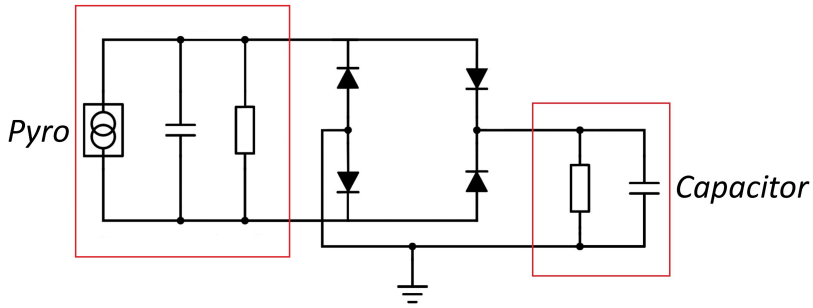

Fig. 5.8 Full wave bridge rectifier circuit used to supply an external storage capacitor during thermal cycling [131].

as a result of irradiation of the material with an IR lamp is transformed into a symmetrical full wave bridged rectifier circuit that was formed from four diodes (Vishay GP02) and the energy was harvested by free standing pyroelectric PVDF film with an area of (10 x 10) mm^2 with a 52 μm thickness. The cycled IR beam current from the pyroelectric generator ('Pyro') was then rectified and discharged into an external capacitance output ('Capacitor'). The corresponding electric circuit diagram in Figure 5.8 shows the standard h-bridge configuration employed supplying the rectified electrical energy into an external storage 100 nF (AVX) multilayer ceramic capacitor (C) with the pyroelectric element acting as a current source in parallel to an RC element. According to the energy harvesting circuit in Figure 5.8, various meshed pyroelectric PVDF samples were exposed to the cycled IR beam while the rectified capacitor terminal voltage was recorded. The terminal DC voltage for the storage capacitor was measured using a Keithley 6514 electrometer [131].

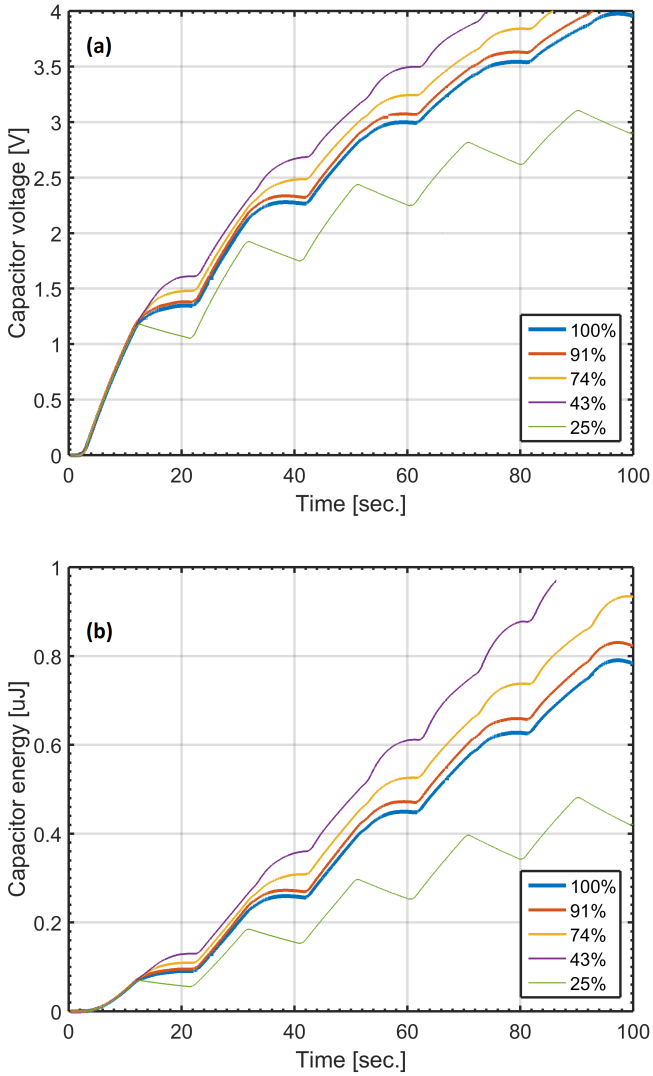

Fig. 5.9 (a) capacitor voltage and (b) harvested thermal energy with meshed electrodes stored in an external 100 nF capacitance [131].

Figure 5.9 (a) compares the charging performance with the rectifier circuit from Figure 5.8 of the fully covered 100 % reference electrode with meshed 91, 74, 43 and 25 % covered samples at the external capacitance over five thermal cycles. The rectified instantaneous current from Figure 5.1 c is stored in the external capacitive element as potential difference accumulating the harvested electrical energy. The capacitor voltage of 4 V after 100 sec. of continuous charging shows a steady increase for the fully covered reference electrode in Figure 5.9 (a). With meshed electrodes, the 4 V potential difference was reached after 84 sec. with the 74 % covered meshed electrode and after 70 sec. with the 43 % covered meshed electrode, respectively. Compared to the fully covered electrode, the 43 % covered meshed electrode charges the rectification circuit 1.42 times faster, improving device performance, efficiency and energy conversion. Further improvements is charging time can be achieved for higher capacitor voltages. However, when reducing the electrode coverage to 25 %, the meshed PVDF film is unable to build up the external capacitor voltage to 4 V within 100 second, underperforming the fully covered design. According to equation 4, the energy stored at the external 100 nF capacitor at 4 V corresponds to 0.8 μJ. Figure 5.9 (b) compares the energy for the individual PVDF samples for continuous thermal cycling. The benefit with meshed electrodes is the quicker charge build up enabling faster thermal cycles and harvesting more energy. Due to the squared dependency of the stored energy (equation 2.4), meshed electrode significantly improve pyroelectric energy harvesting [131].

5.7 Conclusions

Significant improvements for energy harvesting with meshed electrode on PVDF were achieved, showing a complete experimental series of meshed electrode coverages. Since the test devices were exposed to the radiation only at the upper electrode (top down), absorbance and transmittance, neglecting back-reflections, for the here employed aluminium electrodes significantly improved followed by a greater pyroelectric energy trade off. In order to fully utilise the available radiation energy source, Chapter 6 will present a black-body absorber on PVDF using a graphene-ink based electrode material.

Chapter 6

Graphene-ink electrodes for pyroelectric energy harvesting

6.1 Introduction

Heat transfer enhancements for pyroelectric energy harvesting improve energy density, peak energy generation and energy efficiency. For graphene ink electrodes with a thermal absorption of 97 %, the complex interaction between radiative- and conductive-heat transfer dominates the pyroelectric energy harvesting performance. With screen printed graphene ink electrode structures on free standing PVDF, the open-circuit voltage and close circuit current was measured as well as the electric energy that was harvested and stored in an external storage capacitance. Since all pyroelectric systems are also piezoelectric, the 2-2 connected laminated ferroelectric polymer-graphene ink device experiences a high interface coupling between surfaces inducing a tangential shear stress when thermally excited leading to both a pyroelectric and a piezoelectric response and enhanced energy harvesting performance.

6.2 Radiation emissivity, thermal and electrical conductivity of graphene-ink

When utilising thermal radiation for pyroelectric energy harvesting, an ideal electrode material should have a high radiation absorption ('black body') along with a high thermal- and electrical-conductivity in order to fully utilise the available thermal energy and accumulate the free surface bound charge. According to Kirchhoff's law of radiation (equation 3.10), a high radiation absorption material reduces reflection and transmittance, and therefore improves heat transfer when integrated with a pyroelectric material. This leads to improved

energy densities with pyroelectric systems, high peak power generation and improved energy efficiencies under constant thermal boundary conditions. Various forms of molecular carbon experience high electrical conductivity, high thermal conductivity and high thermal radiation absorbance. Compared to conventional metal electrodes, potentially highly flexible and ultrathin graphene sheets provide outstanding mechanical properties and a high radiation absorption with increasing thickness [152]. Due to the arrangement of the graphene-ink sheets in a thick structure, electrical conductivity between sheets and the surface morphology of graphene acting as 'black-body' and leading to an radiation absorption gain compared to conventional metallic electrodes. Therefore, in this chapter molecular graphene sheets dispersed in a polymer ink are deposited on free standing flexible PVDF in order to enhance the pyroelectric energy harvesting performance. When in contact with the pyroelectric material, the interconnected graphene sheets bonded in the dried ink act as an electrical conductor while the individual graphene sheets absorb the thermal radiation energy needed for the change in temperature.

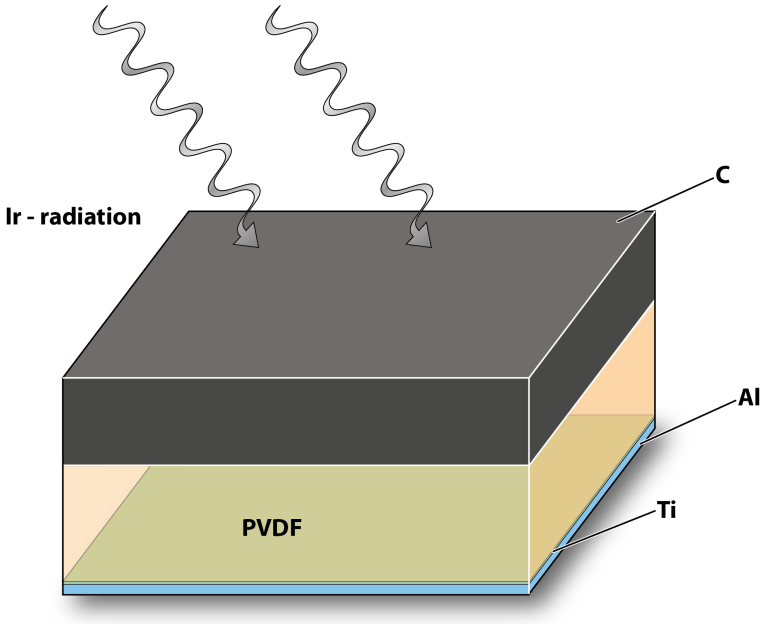

Fig. 6.1 Graphene ink electrode on flexible PVDF.

In an analogous approach to a mesh electroded pyroelectric energy harvester (Figure 4.1), Figure 6.1 shows an upper graphene-ink electrode on a PVDF film with a standard Ti/Al bottom electrode exposed to a radiation beam. The pre-poled pyroelectric active PVDF material employed in this work is identical to the material used for the meshed electrodes in section 4 and section 5, and acts as a carrier for the graphene ink. In contrast to the standard metallic electrodes which require a sputtering or low vacuum metal evaporation deposition

process, the screen printing deposition process performed in this work is remarkably simple leading to potentially large scale, low cost and highly flexible pyroelectric energy harvesting devices.

6.3 Flexible graphene-ink electrodes on free standing PVDF films

Graphene ink – HDPlas Sc213 supplied by Haydale Ltd. (Wales) was used as an electrode material for the PVDF film type harvesters. The graphene ink electrode was screen printed using an ATMA AT - 25PA (US) screen printing setup with a squeegee speed of 220 $mmsec^{-1}$ at constant pressure (squeegee material: Shore 70A 0605) on a flat prepoled (2 x 2) cm^2 and 52 μm thick PVDF film using a 200 μm square sized mesh screen. The extrusion manufactured PVDF film was held in place by the screen printing mask. Following an extensive drying period of several days at room temperature, subsequent thickness measurements, after the ink dried, were conducted using a Dektak (US) surface profiler across the edges, the corners and the centre pf the test specimen. With an average thickness of 18 μm ($\pm$ 10 %) the screen printed graphene ink on flat PVDF shows a homogeneous thickness with a PVDF to electrode thickness ratio of $\sim$ 3 (52/18). This is unusual, since the electrode is relatively thick in comparison with the pyroelectric active PVDF layer. Compared to previous studies on high thickness ratio zinc (Zn) or aluminium (Al) electrodes, a ratio of 0.09 shows an enhancement for pyroelectric energy harvesting [153]. Based on the presented manufacturing process, critical electrical- and thermal-properties for pyroelectric energy harvesting needs to be determined.

6.3.1 Electrical characterisation of graphene-ink

In order to prove the electrical conductivity of the screen printed graphene ink electrode, the electrical surface resistance was measured. Unlike bulk resistance measurements, the film type graphene-ink electrode was surface probed in order to obtain conductivity values for film type electrode architectures. With a linearly arranged Jandel (UK) four point probe (tungsten carbide with a probe spacing of 5 *mm* needle to needle), bipolar line sweep calibration measurements against an indium tin oxide (ITO) on a glass substrate were conducted. The four point probe measurement technique was employed in order to eliminate contact resistance between the probe needles and the the grahpehe-ink surface. Derived from Ohms-law, the surface resistance for a sweep of voltage-current boundary conditions determines the sheet resistance for the test surface. The manufactured screen printed graphene electrodes had a

measured surface resistance of 65 Ωsqr^{-1}. Compared to a highly conductive square meshed electrodes (from Chapter 4) that had a measured surface resistance of 0.58 – 7.2 Ωsqr^{-1} (depending on the surface electrode coverage), the graphene-ink electrodes are almost 10 times more resistive leading to parasitic joule heating losses across the electrode width length.

6.3.2 Thermal characterisation of graphene-ink electrode

Bulk thermal conductivity measurements for the screen printed graphene ink were conducted according to ISO8301 and ASTM C518 standards using a TA instruments (US) Fox 50 measuring setup. Prior to these measurements, the ink was screen printed (1.2 *mm* thick) onto a larger copper disc (50 *mm* diameter and 0.45 *mm* thick). In order to prevent surface thermal resistance, the sample was placed between two Peltier elements and the surface contact was ensured with a copper grease. Since the copper disc has a high thermal conductivity and is relatively thin with respect to the sample thickness, the heat flow between the two Peltier devices is dominated by the test thermal resistance of the printed graphene ink. With an average thermal conductivity k of 1.8 $Wm^{-1}K^{-1}$ at 20, 40 and 60 ºC for the graphene ink, the lower thermally conductive nature of the ink shows a much lower k value than the reported k values for graphite or 2D graphene sheets (8.7 – 2900) [154].

6.4 Heat transfer with graphene-ink electrodes

For the pyroelectric energy harvesting characterisation, the graphene ink electroded PVDF film was exposed to a cycled infra red (IR) light beam of 293 $mWcm^{-1}$ operating at a switching frequency 0.05 Hz. Considering the thick nature of the screen printed electrode of 18 μm, the radiation absorption is the dominating heat transfer phenomenon. As a reference, a fully covered standard 0.2 μm thick evaporated aluminium electrode was characterised under identical energy harvesting boundary conditions along with the meshed electrodes reported in section 4 for comparison.

According to figure 6.2, the radiation absorption coefficient for the evaporated aluminium reference electrode is 0.2 across the effective lamp spectral wave length [142]. For the un-electroded PVDF film, the wavelength dependent radiation absorption coefficient decays from a perfect absorption of 0.97 at shorter wavelengths to 0.2 at longer wavelengths around the far end of the visible light spectrum [67]. For reasons of simplicity, it is assumed that across the relevant light spectrum between 400 and 900 *nm* at low temperatures the graphene ink acts as 'black body' absorber with a nearly perfect and constant absorbance (0.97) due to

the thick nature of the electrode deposition. Here, the arrangement of graphene layers in the thick polymer ink structure acts as 'carbon black' surface [155].

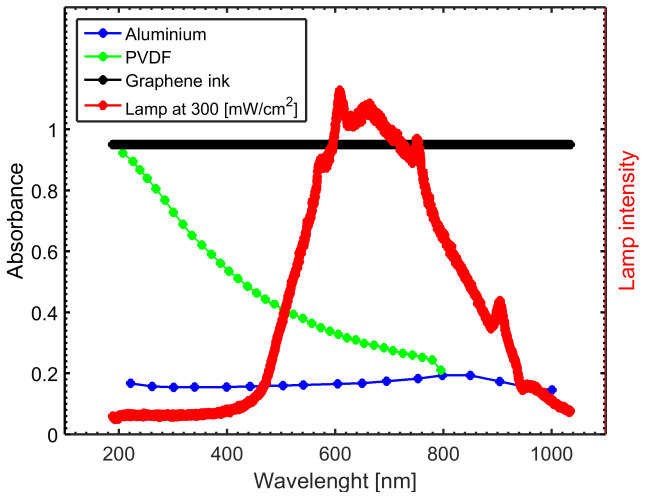

Fig. 6.2 Lamp radiation emission and graphene-ink [152], PVDF [140] and aluminium [142] radiation absorption.

Energy harvesting measurements with an emphasis on the total change in polarisation based on the available change in temperature were conducted. In response to the cycled IR light beam, the absorbed radiation thermal energy and the corresponding temperature evolution is recorded and analysed for the top and bottom electrode surface temperature of the graphene ink (exposed to the lamp radiation) and Ti/Al bottom electrode in Figure 6.1, and compared with the fully covered aluminium type reference harvester. Temperatures were measured by contact conduction using a K-type leaf type thermocouple (OMEGA – US) at the top and the bottom electrodes.

The aim of the temperature analysis is to determine the difference in radiation absorption between the different electrode concepts and the effect they take on the absolute change in temperature. For the rapid changes in temperature performed in the test, radiation, conduction and convection across the pyroelectric active element dominate both the absolute change (ΔT) in temperature as well as the rate of change of temperatures (dT/dt) . According to Figure 6.3, the controlled changes in temperature of the harvesters and the transient change in temperature take place at a constant average temperature. For the symmetric transient change in top electrode temperature with a graphene ink electrode, the pyroelectric harvester experiences a change of +3 K over 10 sec. followed by a change of -3 K after another 10 sec. The change in temperature for the fully covered (100 %) aluminium reference electrode is smaller at $\pm$ 1 K and for the 74 % and 45 % covered meshed electrodes are 1.8 K and 2.0 K, respectively. It is interesting to note that the aluminium reference electrode shows

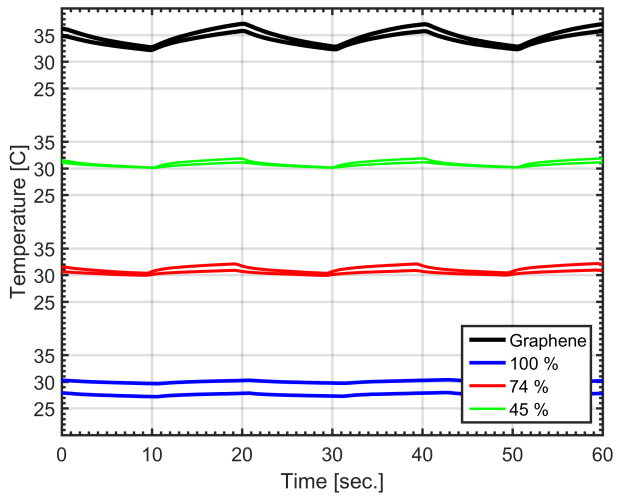

Fig. 6.3 Electrode top and bottom surface temperature.

a considerable temperature difference between the top and the bottom temperature ($\pm$ 1 K). For a decreasing meshed surface coverage, the temperature difference between the top and bottom temperature diminishes to zero with the 45 % covered meshed electrode. For the down sweep, the temperature decay with the 45 % covered mesh top and fully covered bottom electrode are identical.

6.5 Strain enhanced pyroelectric PVDF-graphene ink electrodes for electrodes

Due to the different heat transfer phenomena for heating and cooling with the IR lamp set-up, all four types of harvester (graphene-ink, fully covered aluminium, 74 % and 43 % mesh covered aluminium) develop a temperature gradient when heated. Unlike the meshed and the reference electrode, the graphene-ink type harvester shows a significant change in temperature difference between the top and bottom electrode for the up and down temperature sweep. With the quasi 'black body' graphene-ink on the PVDF substrate, the layered device with a relatively thick 18 μm graphene-ink electrode compared to a thin 200 nm aluminium electrode experiences high interface bonding followed by a high strain due to thermal strain when periodically heated and cooled. Figure 6.4 shows three sequential pictures captured over 5 sec. of the periodic heating wave generated by the IR lamp test set-up. In order to demonstrate the high strain, experimental boundary condition applied in figure 6.4 differ from the temperature measurements in figure 6.3 in terms of: no planar heating, high radiation intensity, and one point sample fixture.

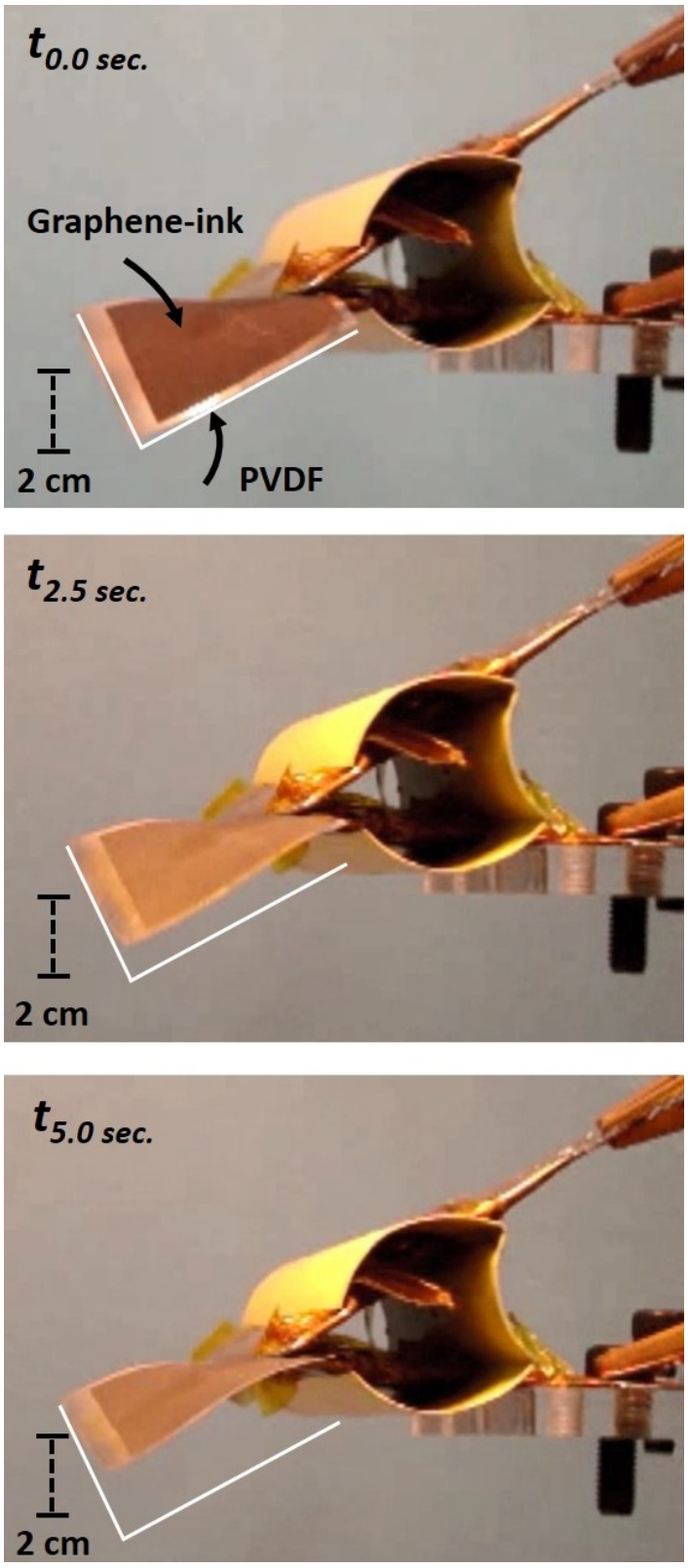

Fig. 6.4 Deflection of PVDF-graphene-ink structure when heated.

With a thermal expansion coefficient of $\alpha_V = 150\ \mu m.m^{-1}K^{-1}$ [156] for the PVDF and thermal expansion coefficient ranging from 0 to 6 $\mu m.m^{-1}K^{-1}$ for graphite/graphene [157], a significant difference can be assumed. This difference in thermal expansion of the graphene-ink in combination with the thermal strain of the PVDF substrate film seems sufficiently high in order to induced a shear stress at the layer interface. Since the exact composition of the industrial graphene-ink is unknown, further studies of the thermo-mechanical properties are required (eg. Youngs modulus, poisson ratio, thermal expansion coefficient) in order to analyse the effect of thermal strain in a mechanical model. With highly anisotropic extruded PVDF films, the strain effects and the interaction between the 2-2 layered graphene-ink and the polymer experience a complex bonding behaviour. However, the graphene-ink layer is observed to be sufficiently thick and stiff to strain the underlying pyroelectric material and also does not to crack or de-bond during the observed deformation, wrinkling-, buckling-, bending- and deflection-moments. Rough estimates comparing the performed change in temperature (dT) per thermal cycle of the meshed aluminium electrodes with the graphene-ink electrode device, meshed electrodes experience only half the rate of change in temperature (dT/dt) and also half the absolute change in temperature (dT) compared to the graphene-inked device. Therefore, the meshed electrode device provides only half the electric energy (I and V), for which reason it is assumed that the piezoelectric contribution with graphene-ink is fairly small due to the linear heat-electric energy relationship with pyropelectrics (equation 2.4 and 2.5).

Considering the continuously changing temperature difference across the pyroelectric element, the internal stress enhances the pyroelectric activity of the harvester by the piezo-electric secondary contribution (equation 2.3). The utilisation of the purely pyroelectric component as well as and the secondary piezoelectric contribution in a flexible pyroelectric device takes into account the properties of the thick layered ink and the anisotropic properties of the aligned molecular chains in the PVDF harvesters the anisotropic piezoelectric shear charge coefficients d_{31} and d_{32} affecting the bulk system behaviour non-uniformly. Reports on a high adhesive interface bonding show a seven times higher stress in stretched direction followed by a dominant secondary contribution [158]. In this work, the 2-2 interface bonded laminates develop a stress as a result of a mismatch in thermal expansion. Considering that the graphene ink has a low strain and is not very stretchable due to the high thickness, the graphene ink harvester can be considered a hybrid harvester utilising the strain induced (piezoelectric) change in polarization as well as temperature induced (pyroelectric) change in polarisation. Compared to the aluminium electrodes reported in section 4 and 5, the thin nature of the aluminium is not able to strain the pyroelectric harvester followed by a lower change in temperature compared to the black body absorber; adding a thick aluminium layer

by sputtering/evaporation of 10's of microns is also not practical for thermal and mechanical reasons.

6.6 Pyroelectric energy harvesting with graphene-ink electrodes

Since the pyroelectric signals (current and voltage) indicate the pyroelectric activity of a harvester, the open circuit voltage and closed circuit current based on the performed changes in temperature (dT and dT/dt) are conducted. Since the pyroelectric current is a linear function of the rate of change of temperature (dT/dt), dT/dt is calculated in Figure 6.5 (a) using the time forward derivative based on the top electrode (exposed to the IR beam) temperature evolution in Figure 6.3. The function envelope in Figure 6.5 (a) corresponds to the pyroelectric closed circuit current in Figure 6.5 (b). Following a symmetric change in temperature, the closed circuit current shows a symmetric AC current for the fully covered reference as well as for the meshed electrodes in Figure 6.5 (b). For the graphene-ink electrode, a 10 $nAcm^{-2}$ current for the cooling period was measured followed by a 13 $nAcm^{-2}$ for the heating period. Compared to the reference electrode, the non-symmetric profile stems from the fact that the graphene ink has an advantage in radiative heat transfer due to the high absorption coefficient compared to highly reflective aluminium. However, for convective cooling this advantage does not apply leading to an identical cooling evolution with fully covered-, meshed- and graphene ink-electrodes. Nevertheless, the use of graphene ink electrodes doubles the closed circuit current in Figure 6.5 (b) and open circuit voltage in Figure 6.5 (c) compared to the 45 % covered meshed electrode and 500 % improvement of the closed circuit current and open circuit voltage performance compared to the 100 % reference aluminium electrode. Considering the linear relationship between the change of temperature and the effective pyroelectric current in equation 2.4, the available change in temperature only partially accounts for the enhanced pyroelectric energy conversion. According to equation 2.5, the calculated current magnitude based on the dT/dt is lower for all four samples due to the thermal resistance at the thermocouple interface. However, the steeper decay of dT/dt (Figure 6.5 a), as well as the current (Figure 6.5 b) for the fully covered, 74 % and 43 % compared to the graphene-ink samples indicates a difference in heat transfer performance. Since the AC pyroelectric current in highly non-symmetric with the graphene-ink electrodes, the available energy is difficult to account for and cannot be directly compared. By employing the full wave bridge rectification circuit from figure 5.7, the rectified energy stored in an external capacitance and compared over several heating

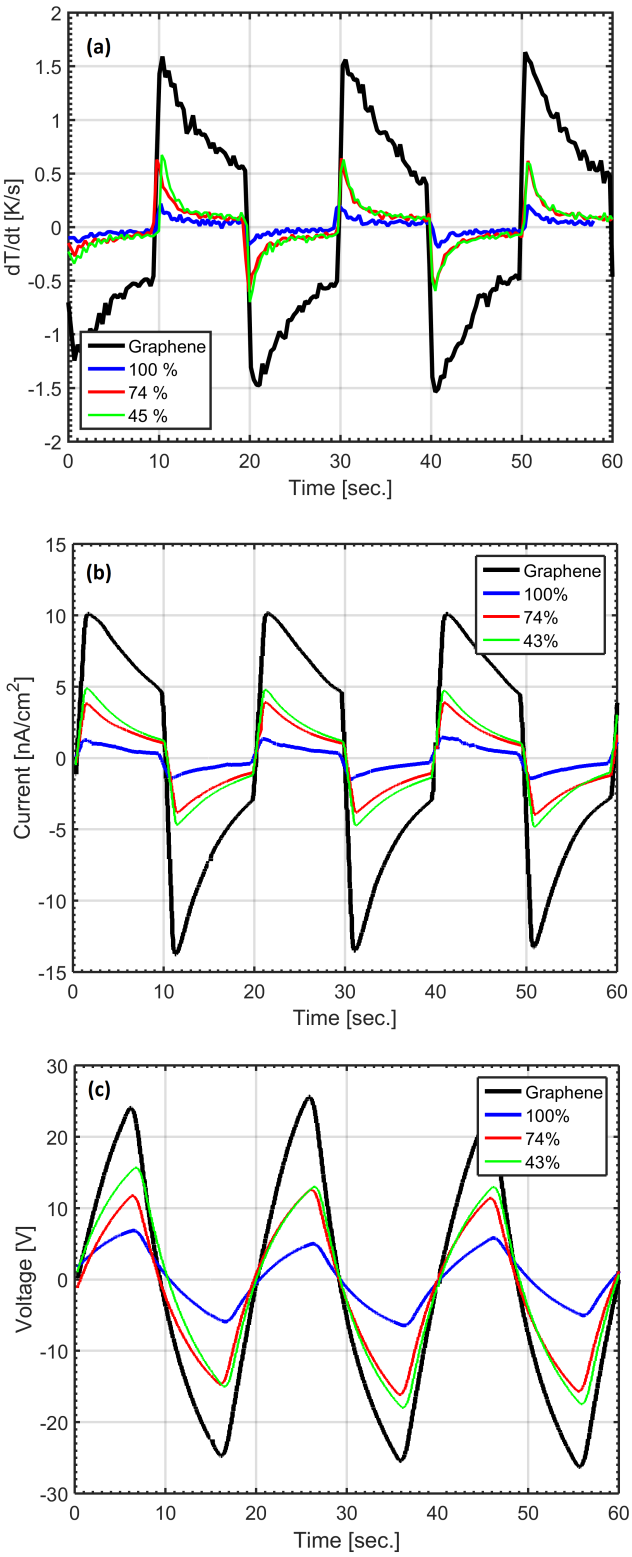

Fig. 6.5 (a) Rate of change of temperature (dT/dt), closed circuit pyroelectric current (b) and open circuit pyroelectric voltage (c) for fully covered reference aluminium electrode (100 %), meshed electrode increments and graphene-ink top electrode.

cycle in order to quantify the harvesting potential with graphene-ink electrodes based on a potential application scenario.

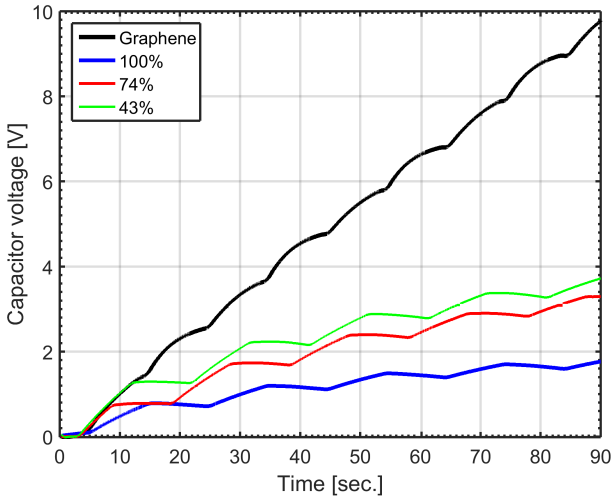

Fig. 6.6 External capacitor voltage over 90 sec. of charging.

According to Figure 6.6, the fully covered reference sample charges the external 100 nF storage capacitor to 1.9 V terminal voltage. Compared to the reference electrodes, the meshed 74 % and 43 % samples charge the capacitance to 3.5 V and 3.9 V, respectively over the same period of time. For the graphene ink pyroelectric energy harvester, the capacitor terminal voltage is 9.5 V after 90 sec., providing a five times higher voltage than the fully covered reference. In terms of energy, the stored charge is 25 times higher due to the squared voltage relationship ($E = \frac{1}{2}CV^2$). Employing graphene-ink electrode leads to higher absolute changes in temperature, higher rates of change in temperature and higher energy generation.

6.7 Conclusions

Strain enhanced pyroelectric energy harvesting shows significant improvements in open circuit voltage, closed circuit current and energy conversion. In particular with thick layered structures of PVDF-graphene-ink, the mechanical component due to thermal strain as well as the heat transfer component due to the 'black body' nature dominates the pyroelectric energy conversion. The presented proof of concept enables an insight into the complext interaction between pyroelectric primary and secondary contribution. Further characterisation of the industrial graphene-ink and the comparison between printable conductive ink manufacturers using different binder-, solvent- ink-compositions and concentrations remains the scope of

future work in this field. Nevertheless, by employing black ink electrodes enhanced radiation absorbance provides a novel route to pyroelectric sensors and energy harvesters.

Chapter 7

Pyroelectric generator utilising temperature oscillations from oscillating heat pipes

7.1 Introduction

By linking the subject fields of heat transfer in oscillating heat pipes (OHPs) for high performance cooling together with a pyroelectric energy harvesting device, the system exploits a heat induced liquid-vapour transition of a working fluid as a primary driver for a pyroelectric generator. The two phase instability of a fluid in a closed looped capillary channel of an oscillating heat pipe (OHP) creates pressure differences which lead to local high frequency temperature oscillations in the range of 0.1 – 5 K. Such temperature changes are suitable for pyroelectric thermal to electrical energy conversion, where the pyroelectric generator is attached to the adiabatic wall of the OHP, thereby absorbing thermal energy from the passing fluid. This new pyroelectric-oscillating heat pipe (POHP) assembly of a low temperature generator continuously operates across a spatial heat source temperature of 55 °C and a heat sink temperature of 25 °C, and enables waste heat recovery and thermal energy harvesting from small temperature gradients at low temperatures. Eventually, the POHP system acts as waste heat recovery and thermal energy harvesting device capable of converting small fractions of low grade thermal energy into electric energy.

7.2 Waste hear recovery, thermal energy harvesting and compact cooling

Today, over 80 % of the world's electricity is generated from heat [159] and conventional generators such as internal combustion engines (>900 °C) or external combustion cycles (> 450 °C) operate extremely efficiently at such high temperatures. However, the fossil fuel resources, such as coal and gas, which are required to generate high temperatures are limited in availability and the technologies are greatly optimised. At a lower temperature scale, Organic Rankine Cycles (ORCs) are capable of effectively utilising low temperature heat (> 150 °C), but much of this low grade heat is often not exploited and is simply wasted and released into the atmosphere [160]. This untapped waste heat ranges from thermal management of microprocessors, industrial curing processes, and geothermal sources to more unconventional heat sources such as the human body and contact friction. When exploiting waste heat for energy generation, the generated electricity improves the conversion efficiency of the primary thermal driver and reduces thermal pollution, and is therefore an opportunity for harvesting otherwise unused thermal energy. However, temperatures below 100 °C are difficult to recover and to harvest, since the available thermal gradient is low. The use of thermoelectric generators (TEGs) when assembled into a device can be limited, because a practical effectiveness requires large spatial temperature gradients [13].

There is an increasing number of industrial and consumer electronics devices with a need to achieve miniaturisation and circuit integration and this leads to highly concentrated thermal areas which require structurally small heat transfer devices to transport heat. This includes microprocessors, voltage transformers and current rectifiers, since much of the modern electronics requires a direct current (DC), and a wide range of mobile computing devices or electric motors; the use of water-cooling pumps or blower fans is undesirable due to safety or noise concerns. As a result, the need for more effective heat transfer devices is rapidly growing [161]. The application area of heat pipes and oscillating heat pipes (OHPs), also termed pulsating heat pipes (PHPs), is attracting interest for thermal management or low gradient heat transfer, since they have a high effective thermal conductivity and can be fabricated in almost any shape and size [162]. When an OHP moves thermal energy from one place to another, the naturally driven fluid flow leads to temperature oscillations along the device surface and provides an opportunity for pyroelectric based energy harvesting. Since pyroelectric materials produce an electrical current from temperature changes (dT/dt), the surface temperature oscillation from OHPs can be therefore transformed into electricity while it effectively provides cooling for heat concentrated areas. For such a system , the combination of compact cooling, waste heat recovery and thermal energy harvesting with

pyroelectrics is of significant interest since naturally occurring temperature oscillations are often at much lower frequency («1 Hz). Efforts to employ pyroelectric materials for thermal energy harvesting at high frequencies have led the development of self-induced pyroelectric engines that make use of a bistable membrane for mechanical switching, generating an open circuit voltage of up to 13 V (primarily utilising the piezoelectric effect since all pyroelectrics are also pyroelectric) [92]. Other theoretical approaches employ the difference in thermal conductivity between a liquid and a vapour fluid to provide mechanical motion for a pyroelectric engine [163] or a cantilever structure which mechanically switches the heat flow [94]. However, due to the complexity of these systems the energy trade-off is typically small with pyroelectrics.

The proposed solid state assembly in this chapter is a novel type of waste heat recovery and thermal energy harvesting device capable of transforming low temperature fluctuations in oscillating heat pipes into electricity utilising the pyroelectric effect. The combination of pyroelectrics (P) with oscillating (O) heat (H) pipes (P) – POHP, enables highly effective heat transfer at low temperatures transforming heat into electricity where needed. The proposed POHP system is free of mechanical motion, compared to conventional liquid vapour energy systems employing large size impulse machinery, where the pyroelectric element is powered by the heat that is exchanged within an OHP. This type of generator assembly has the potential for applications in compact cooling, operation in harsh environments due to the sealed design, solid-state thermal to electrical conversion, and utilising a wide range of temperatures by tailoring the working fluid. There is also potential for miniaturisation of the system with weight reductions and downscaling benefits with micro fluid systems. In addition, the cooling performance enhancement is expected to be 100 times greater than conventional cooling systems due to the variable surface tension with fluid mixtures and the possibility of a supercritical evaporation [164]. The POHP generator can therefore be considered as an efficient low temperature electric power generator and cooling device.

7.3 Pyroelectric - Oscillating Heat Pipe (POHP)

The complex interaction between the different heat transfer principles of conduction, evaporation and condensation is the driving force of a self-sustaining pulsating fluid flow in an OHP system. The OHP device is initially filled with a working fluid in the liquid-vapour saturation state, and is then placed between a hot reservoir (heat source) and a cold reservoir (heat sink). Figure 7.1 shows a schematic of a closed-loop OHP device [165]. In the OHP, a single capillary channel that separates the liquid ‘slugs’ by vapour ‘plugs’ moves the working fluid successively through the hot evaporator area (left side in Figure 7.1) and through the

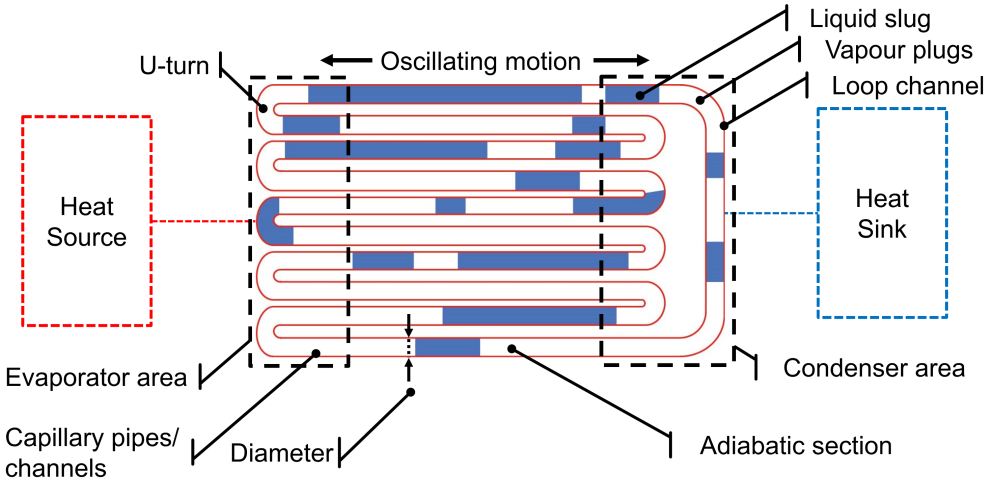

Fig. 7.1 Schematic diagram of closed loop oscillating heat pipe (OHP) [165].

cold condenser area (right side in Figure 7.1) [162]. As a result, the working fluid evaporates at the evaporator zone at the left side of Figure 7.1 and condenses at the condenser zone at the right side of Figure 7.1 creating local pressure difference. The induced liquid-vapour phase transitions creates a self-driven, rapidly pulsating and circulating fluid flow in the looped capillary channel of the OHP [166]. This sudden change in thermodynamic state of the fluid is determined by the fluid temperature, pressure, gravity and fluid surface tension, where the self-arranged fluid continuously absorbs heat at the hot evaporator zone and ejects it at the cold condenser zone after passing through the central adiabatic section (centre of Figure 7.1) [167]. When considering the energy balance, and considering no heat losses to the surroundings, the amount of absorbed heat at the hot side corresponds to the amount of ejected heat at the cold side. A key variable to design a viable OHP device is the hydraulic capillary channel diameter (maximum diameter of channel) that separates the liquid-vapour plugs and slugs by the fluid surface tension. By consider the Bond number Bo, which is the ratio between gravitational and capillary forces acting on an isolated bubble in a vertical capillary tube, the first design approach for an OHP is to determine the critical channel diameter [162]:

$$Bo = \frac{1}{2}\frac{d_h^2.g(\rho_l - \rho_v)}{\tau} \tag{7.1}$$

where $\rho_l - \rho_v\ kgm^{-3}$ is the density difference between the two phases ($\rho_l =$ fluid and $\rho_v =$ vapour), and $\tau\ nm^{-1}$ is the surface tension of the fluid. The maximum diameter $D_{(n,h,max)}$ of the OHP tube is given by:

$$\frac{D_{(n,h,max)}}{2} = \sqrt{\frac{\tau.Bo}{g(\rho_l - \rho_v)}} \tag{7.2}$$

Equation 7.2 provides a geometrical upper limit of the OHP channel width for maintaining a slugs and plugs separation in the tubes. In addition to the channel diameter, other design parameters include the viscous pressure that increases along the channel length and limits fluid motion and is therefore a secondary geometrical limitation. In addition to the channel design, the selection of the working fluid influences the operation of an OHP with surface tension, latent heat, liquid viscosity and the pressure gradients, determining the characteristic liquid-vapour plug and slug separation in Figure 7.1. At the evaporator area, the emergence of evaporation and nucleated bubbles is the driving force of the natural and self-sustaining bubble train flow [165]. Figure 7.2 shows a top- and a cross-sectional view of the capillary

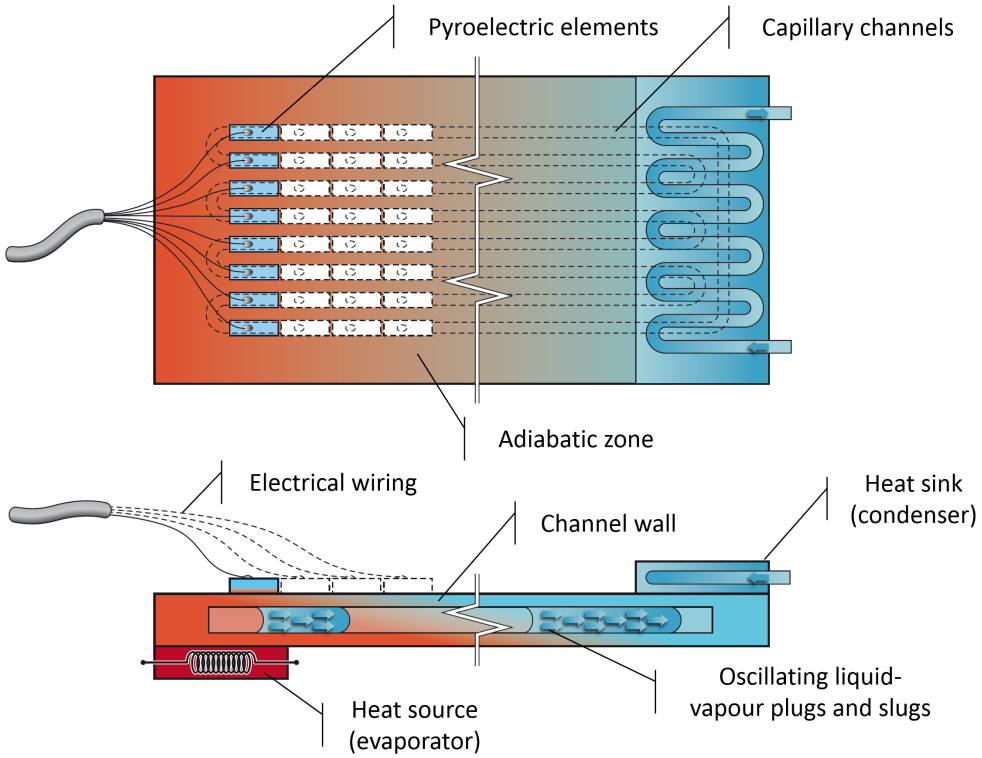

Fig. 7.2 Working principle of a POHP generator with the hot evaporator on the left and the cold condenser on the right side [165].

channels embedded in an OHP device. As a result of the change in heat transfer properties of the liquid slugs and gaseous plugs phases, they also exchange heat along the adiabatic channel wall of the OHP with local fluctuations in temperature. If we consider a pyroelectric element attached to the channel wall, as shown in the left side of Figure 7.2, the passing liquid vapour plugs and slugs sequentially heat and cool the pyroelectric element respectively. Since a pyroelectric directly converts a change in temperature into an electrical potential difference, the temperature variations induced by the passing liquid slug - vapour plug flow

can create an alternating current (AC) proportional to the heat exchange between the fluid and the pyroelectric through the channel wall. While thermoelectric modules based on the Seebeck effect (TEGs) recover heat from spatial temperature gradients, the available transient change in temperature (dT) with OHPs changes the polarisation ΔP_s of a pyroelectric material (equation 2.3) [79]. For the pyroelectric elements attached to the OHP channel wall, as in Figure 7.2, the consecutive heating and cooling cycles at the OHP adiabatic wall, the passing liquid-vapour plugs and slugs inside the OHP channel continuously thermally excite the pyroelectric generator which then drives an alternating closed circuit current I. When a pyroelectric (P) is combined with an oscillating (O) heat (H) pipes (P), POHP, and the assembly operates under a constant heat source and sink conditions, the POHP moves heat from the hot side to the cold side while continuously thermally exciting the pyroelectric element divining a AC across the generator terminals. By carefully choosing the organic working fluids used in the POHP, the phase transition temperature of the evaporation of the system can be adjusted to the available temperature level to tailoring the cooling performance under different thermal conditions for compact cooling applications while simultaneously generating electricity from small temperature differences [165].

7.4 Experimental set-up and methodology

For low temperature gradients, Akacshi [168] introduced a tubular shaped looped OHP partially filled with a working fluid which acted as a powerful heat transfer and cooling device. Compared to a tubular OHP design, flat plate heat pipes combine a high heat flow and a compact design, which is considered a more efficient approach [169]. Tubes fabricated from copper lead to high heat transport rates with minimal spatial temperature gradients across the conductor due to the high thermal conductivity of the material [170]. Therefore, in this work a 24 channel flat plate OHP design (1.6 x 2.0) mm^2 (equation 7.1) and (equation 7.2) with 12 U-turns machined into a 2 mm thick copper base plate (20 x 12) cm^2 (Figure 7.3) is employed.

This plate was covered with a second plate with the same dimensions and 1 mm of thickness, where the adjacent channels were sealed off relative to one another. The evaporator zone of the flat plate pulsating heat pipe in Figure 7.2 and Figure 7.3 was heated by a wire electrical heater (Thermocoax Type ZEZAc10) that was embedded in a copper plate with dimensions of (10 x 120) mm^2 and 2 mm thick by means of a serpentine groove machined on one side of the plate. In rough analogy to Figure 7.2, the heater was connected to electrical power supply (EA Elektro-Automatik model PS8360-10T). On the opposite side, the condenser zone (80 mm long and 120 mm wide) was cooled by an ethylene-glycol/water

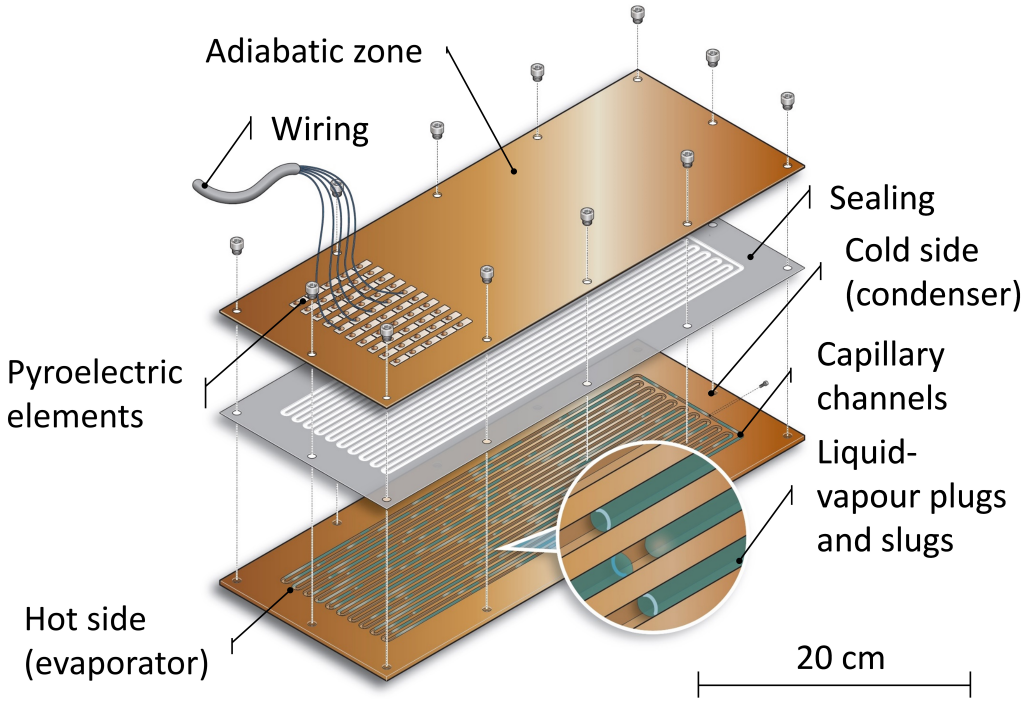

Fig. 7.3 OHP with a pyroelectric generator attached to the wall showing a common ground and connected to an electrometer using the attached wires for pyroelectric voltage and current measurements [165].

mixture flow that crossed an aluminium block whose temperature was controlled by means of a cryostat (Huber CC240wl). Good contact between both surfaces (OHP and aluminium condenser) was provided by screws through OHP holes that uniformly distributed the pressure contact. A pressure sensor (GE PTX5076-TA-A3-CA-H0-PS) allowed recording of the pressure levels and fluctuations in the surrounding loop channel. The OHP was filled with ethanol as working fluid with a filling ratio (liquid volume on total channels volume ratio) of 50 %, where the horizontally orientated channels guide the circulating fluid through the system [165].

Figure 7.3 shows the design of the flat plate closed loop POHP harvesting and cooling set-up, where the pyroelectric elements are placed directly above the capillary channels of the OHP, where the pyroelectric is placed to generate electricity. For the liquid-vapour plugs and slugs, the orientation of the OHP wall is of particular interest since the gravitational force acting on the bubbles leads to a continuous aggregation of liquid at the evaporator zone, particularly in vertical orientation (bottom heated mode). Therefore, two positions were examined over several hours operation time in the laboratories at the institute Pprime CNRS - Universite de Poitiers - France, one with the gravity acting planar to the OHP wall (vertical position), and the other with the gravity acting in a 45° angle perpendicular to the wall. In both positions the boundary conditions are maintained constant with the resistive electric heating power fixed at 120 W and the chiller, maintaining the cold condenser temperature at 20 °C and ensuring constant average temperatures. If the device to be cooled acts as a heat source (left side Figure 7.2 and Figure 7.3), the spatial temperature gradient across the system introduces liquid plugs and vapour slugs which exchange heat along the channel wall of the OHP leading to fluctuations in temperature at a relatively high frequency; we will see later in this work that typical frequencies and temperature changes are 0.45 Hz and 5 K respectively [165]. Figure 7.4 shows the local temperature profile measured at the evaporator (highest temperature), the adiabatic zone and the condenser (lowest temperature) for the 45° tilted wall of the OHP. The temperatures were measured using K-type thermocouples located across the OHP wall. Although the system was synchronised between the evaporator and the condenser, thereby showing an identical temperature envelope, the fluid flow is chaotic and leads to random changes in temperature (dT), starting from 0.1 K at the condenser to 5 K at the evaporator with no particular temperature oscillation frequency. A Fast Fourier Transformation (FFT) analysis did not reveal any characteristic or natural frequency providing a constant line across the frequency spectrum. Therefore, there is no evidence for distinctive temperature oscillation frequencies. This leads to the conclusion that the transient temperature profile is highly unsteady due to the two-phase instability of the working fluid under certain thermal and geometrical boundary conditions [171]. With

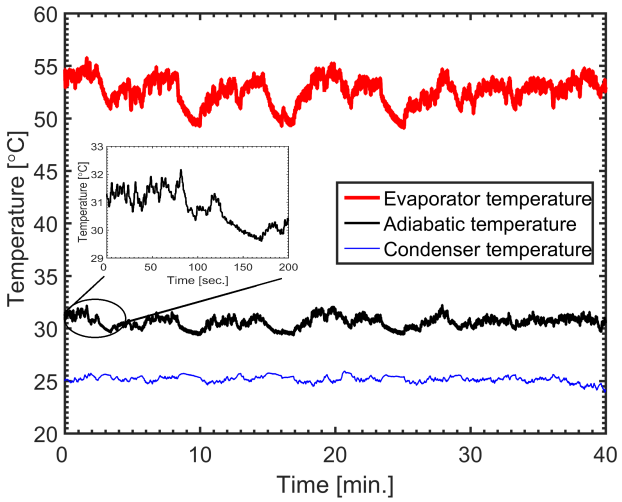

Fig. 7.4 OHP temperature map for 45° operation at an arbitrary chosen time window [165].

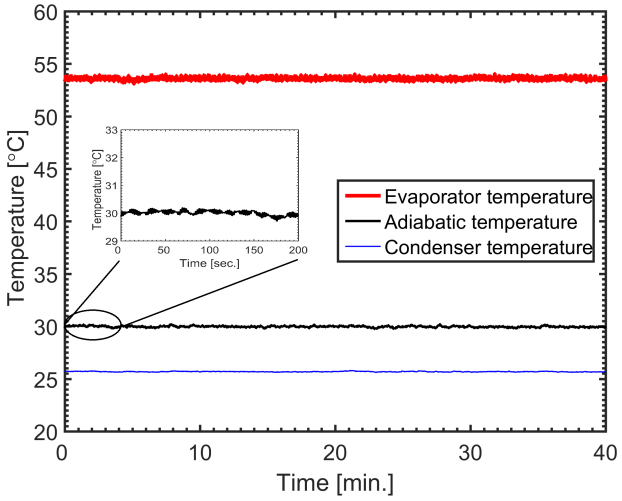

Fig. 7.5 OHP temperature map for 0° operation at an arbitrary chosen time window [165].

horizontally orientated channels (planar gravity), Figure 7.5 shows the temperatures across all three OHP zones (evaporator, adiabatic and condenser). With an average evaporator temperature of 54 °C, a chiller temperature of 26 °C, and a temperature gradient of 28 °C, the OHP operates at a steady state oscillation frequency of 0.45 Hz. Continuous and symmetric temperature oscillations with constant transient temperatures are observed along the adiabatic zone with a temperature oscillation magnitude of 0.3 K; e.g. see the inset in Figure 7.5. The temperature oscillations at the OHP wall that are shown in Figure 7.4 and Figure 7.5 stem from the heat, exchanged with the surrounding environment, which can be utilised to successively heat and cool a pyroelectric generator attached to the wall surface. In order to achieve rapid (equation 2.4) and large (equation 2.5) temperature oscillations to maximise the pyroelectric signal it was found from thermocouple measurements that the highest oscillation magnitude takes place at the lower region of the adiabatic zone, which is closer to the hot evaporator. At steady state operation conditions, as in Figure 7.5, the temperature constantly fluctuates between 38.4 °C and 39.7 °C leading to an available change in temperature of 0.3 K at 0.45 Hz. Compared to already existing pyroelectric thermal harvesters operating in the lower mHz oscillation range [148], the temperature oscillations frequencies in a POHP system are therefore much larger and faster [165]. Since the available thermal gradients

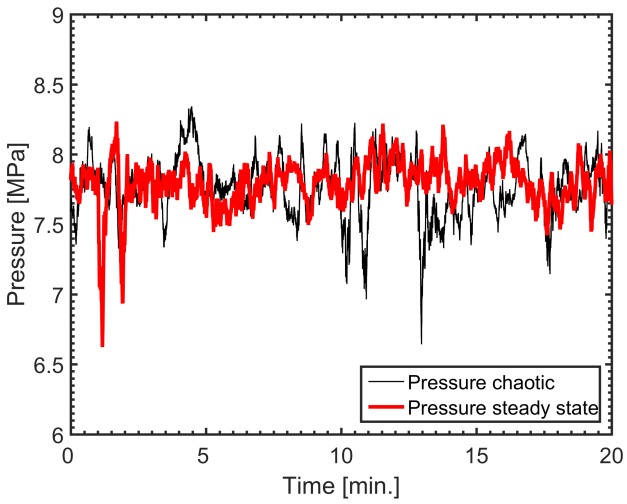

Fig. 7.6 Condenser pressure for chaotic and steady state operation of the OHP at the loop channel [165].

are low at the condenser section (around 0.1 mK), the corresponding liquid-vapour pressure difference is also low. When a pressure sensor was placed at the surrounding looped channel of the cold condenser zone to measure the transient pressure, Figure 7.6 shows the pressure fluctuations for both chaotic and steady state OHP operation. Since the fluid flow at low temperature and pressured gradients is perpendicular to the rest of the channel, pressure for

Table 7.1 Material and POHP device properties for PMN-PT and PZT (modified from [165]).

		PMN-PT	PZT	[Ref.]
ρ	$[\mu Cm^{-2}K^{-1}]$	-746	-380	[38]
A	$[mm^2]$	(11 x 3)	(11 x 3)	[-]
d	$[\mu m]$	500	500	[-]
ε_r	$[-]$	2100	2900	[38]
C	$[nF]$	2.11	0.17	[-]
k	$[Wm^{-1}K^{-1}]$	2	0.8	[38]
T_{Curie}	$[^\circ C]$	121	200	[38]
$Electrodes$	$[-]$	Au	Ag	[-]

chaotic operation and steady state operation are indistinguishable. However, as shown in Figure 7.4 and Figure 7.5, the OHPs provide large and rapid naturally driven temperature oscillations without mechanical switching which are ideally suited to power a pyroelectric generator attached to the wall surface [165].

7.5 Harvesting energy with POHP

Since pyroelectrics are typically electrically and thermally insulating, the heat exchanged between the OHP and the pyroelectric generator is assumed to be via conduction only, where the contact area between the pyroelectric element and the OHP wall determines the heat flow. In this work we have placed both a (11 x 3) mm^2 and 500 μm thick lead z-cut <111> industrially grown and pre-poled magnesium niobate – lead titanate (PMN-PT) single crystal (APC-International Ltd. - US) and a prepoled polycrystalline lead zirconate titanate (PZT) (11 x 3) mm^2 and 500 μm (PI-Ceramics GmbH - Germany), on the OHP wall directly above the adiabatic channel (Table 7.1). Since the OHP utilised in this work was not designed with harvesting in mind, the use of solid PMN-PT and PZT pads suites the flat surface of the device. When using flexible pyrelectric PVDF, the interface contact with thermal conduction requires sophisticated surface bonding techniques. In addition, the materials employed here are off the shelf so that the system can be easily reproduced. Figure 7.3 shows the geometrical position and the electrical set-up where the pyroelectric was placed 35 *mm* from the heater (evaporator) and 9 *mm* from the edge. The open circuit voltage and the closed circuit current per element was measured using a Keithley 6517b electrometer (input impedance 200 $T\Omega$) at a sampling rate of 100 Hz together with the temperature measurements using a Picotech TC-08 at a sampling rate of 10 Hz. A good interface contact between the pyroelectric element and the OHP wall was ensured using

a copper paste (Electrolube-UK) providing a good thermal and electrical contact with the common ground. Temperature measurements were conducted using a leaf K-type thermocouple (OMEGA-US) directly below the pyroelectric element and encapsulated in the copper paste [165]. For the steady state operating OHP (Figure 7.5), Figure 7.7 (a) compares the recorded symmetric temperature oscillations with a measured pyroelectric closed circuit current of 4.2 nA, generated by the PMN-PT pyroelectric element. The measured open circuit voltage with PMN-PT was 0.8 VAC (Figure 7.7 b). With an available electrical capacitance of 1.22 nF for the pyroelectric generator, the transformed electrical energy per thermal evolution stored in the capacitive element ($1/2\ C.V^2$) was 1.56 $nJcycle^{-1}$, which corresponds to a specific energy density of 95 $pJcm^{-3}$. When the generated alternating current (AC) was continuously discharged across a full wave bridge rectifier into a 50 pF external capacitor, the available temperature oscillations can charge the external capacitor within 40 sec. to 0.2 V (Figure 7.7 c). This rectification stage is required, since the voltage supplied by the generator is an AC, and most of the modern electronics require a direct current (DC). Since electrical energy stored in a capacitive element suffers increasing leakage with increasing voltage, the voltage at the capacitor saturates because the supplied charge from pyroelectric equals the leakage at the external capacitor; suitable selection of low leakage capacitors can improve this response. The single crystal PMN-PT used in this study has been selected as it has an outstanding pyroelectric properties but does exhibit a relatively low Curie temperature (121 °C), limiting the potentially usable temperature range. Therefore, measurements have been taken with a polycrystalline PZT material, which can operate at higher temperatures due to the higher Curie temperature of 200 °C and consequently can operate at higher temperature levels. However, the pyroelectric coefficient of PZT is lower than PMN-PT (see Table 7.1) which results in lower closed circuit current measurements under identical operation conditions compared to PMN-PT; the PZT has a pyroelectric current of 3 nA as can be seen in Figure 7.7 d. The corresponding open circuit voltage with PZT was also lower, 0.4 V compared to 0.8 V for PMN-PT. The measured current for PMN-PT and PZT is in reasonable agreement with the calculated values for current from equation 2.4 (PMN-PT = 3.3 nA and PZT = 1.7 nA). The continuous pyroelectric signals together with the harmonic temperature oscillations at the OHP wall lead to the conclusion that the system operates at steady state with the fluid-vapour bubbles oscillating symmetrically across the adiabatic zone [165]. To achieve chaotic changes in temperature, as in Figure 7.4, the OHP was tilted by 45° with respect to gravity, and the pyroelectric generator was placed in the same position as in steady state operation. Figure 7.8 a shows the generated closed circuit current for a PMN-PT single crystal along with the temperature oscillations at the OHP wall. With a peak current of 20 nA the closed circuit current and

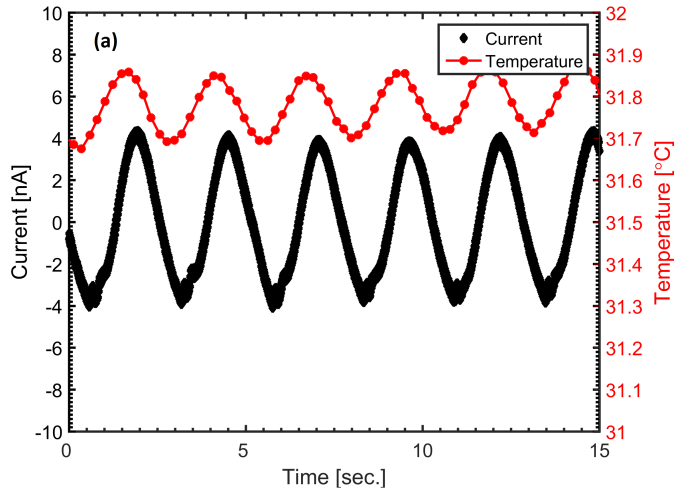
(a)
Current
Temperature
Current [nA]
Temperature [°C]
Time [sec.]
10
8
6
4
2
0
-2
-4
-6
-8
-10
32
31.9
31.8
31.7
31.6
31.5
31.4
31.3
31.2
31.1
31
0
5
10
15

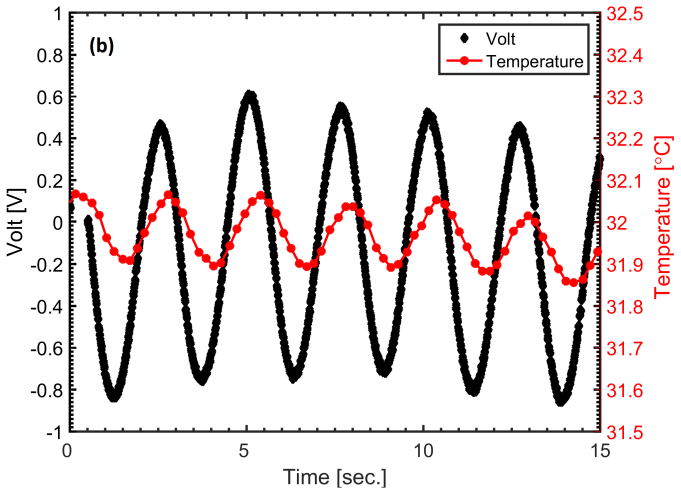
(b)
Volt
Temperature
Volt [V]
Temperature [°C]
Time [sec.]
1
0.8
0.6
0.4
0.2
0
-0.2
-0.4
-0.6
-0.8
-1
32.5
32.4
32.3
32.2
32.1
32
31.9
31.8
31.7
31.6
31.5
0
5
10
15

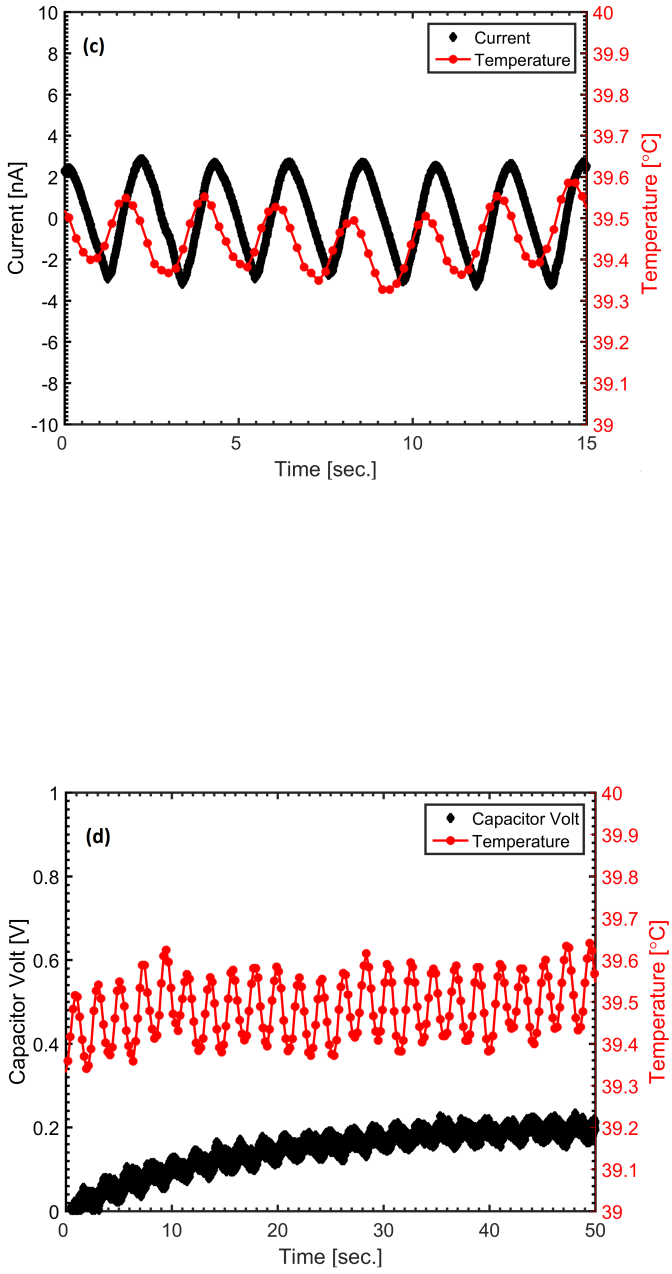

Fig. 7.7 Closed circuit pyroelectric current with PMN-PT (a), open circuit pyroelectric voltage with PMN-PT (b), closed circuit pyroelectric current with PZT (c) and capacitor voltage with PMN-PT (d) for steady-state OHP operation [165].

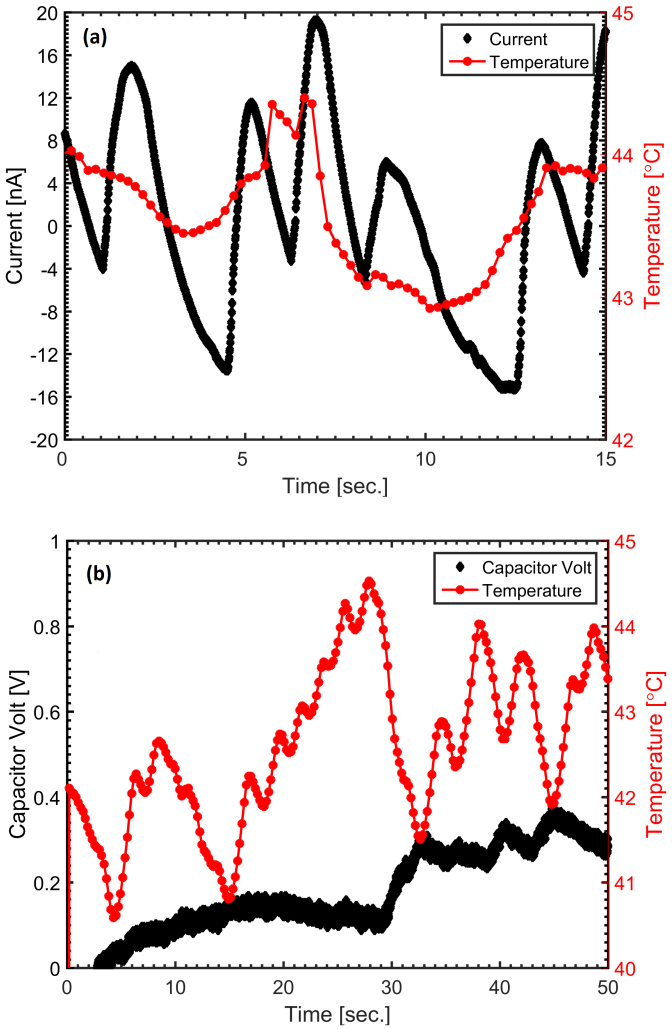

Fig. 7.8 Closed circuit pyroelectric current with PMN-PT (a), and capacitor voltage with PMN-PT (b) for unsteady OHP operation [165].

the change in temperature are significantly higher than in the steady state operation of the OHP (typically 4 nA, Figure 7.7 a). However, no continuous pyroelectric signal can be generated since the temperature fluctuations are unsteady and do not follow a particular pattern. Therefore, a direct discharge of the generated electrical energy across the full wave bridge rectifier into the external 100 nF capacitor leads to a capacitor voltage of 0.4 V at the capacitor terminals. Figure 7.8 b shows the charging profile of the capacitor powered by the pyroelectric PMN-PT with a four times higher rectified and stored energy for unsteady operation of 8 nJ, compared to 2 nJ for steady operation. The temperature fluctuations performed, in both steady and unsteady modes of operation, are highly suitable for pyroelectric thermal to electrical energy conversion, due to the high oscillation frequency of up to 0.45 Hz, providing a new type of thermal to electrical generator operating at low temperatures. Performance enhancements can be achieved by using micro heat pipes of a similar size employed in this work and filled with water-heptanol mixtures that exhibit higher temperature oscillations and larger heat flows [167]. The system conversion efficiency in this work with the POHP and rectification circuit and only one pyroelectric element attached is $\eta = 3.3x10^{-13}$ for the unsteady operation and $\eta = 1.33x10^{-12}$ for the steady operation over 50 sec., determined by the generated energy (8 nJ and 2 nJ) over the heater power input (120 W). This is lower than the theoretical Carnot efficiency of $\eta_{Carnot} = 0.09$ % (55 ºC and 25 ºC), which leads to the conclusion that there is substantial space for optimisation of the OHP-pyroelectric generator system. In addition, two distinctive modes of operation are presented, based on a constant heat input – available electrical output comparison, showing a four times higher energy generation in chaotic mode than in steady state mode. Limitations in transformed energy mainly stem from the poor contact conduction when using structurally thick copper walls which leads to a decrease and a delay in heat flow. It is worth noting that temperature oscillations of a greater amplitude have been observed in the OHP literature [170], suggesting that much larger energy recovery is expected from such systems. For constant temperature oscillations, one approach to improve performance is to introduce grooves into the OHP wall directly above the channel of the working fluid. The generator will ideally to be of equivalent dimensions to the vapour plug displacement inside the channel the fully exploit the temperature fluctuations. For chaotic temperature oscillations, the frequency and magnitude of the oscillations should be enhanced and a more thermally conductive generator geometry with a larger area and patterned electrodes will improve the interface contact conduction. On an industrial scale, integrated cooling and heat recovery units have the potential to utilise the abundantly available heat through an OHP in order to drive a pyroelectric generator and effectively cool heat-concentrated areas without mechanical motion, while also generating electricity locally from the otherwise wasted heat. In the longer term, POHP type of systems

can act as solid-state generators and thermal harvesters operating low-carbon micro-grids where the risk of mechanical wear and failure is eliminated. Therefore, POHP systems combine highly desirable solid-state electricity generation with a powerful closed packed cooling device absorbing otherwise unused heat. The thermal performance convers of the system has the potential to cover range from Watts to kWatts of heat flow, capable of eg. replacing conventional blower fans and large sized heat sinks and providing μW to mW of electrical power for eg. wireless sensor nodes, internet of things (IoT) devices or battery-less technologies [6].

7.6 Conclusions

Nowadays, waste heat recovery, thermal energy harvesting and compact cooling using smart materials is a hot topic. The here proposed pyroelectric - oscillating heat pipe (POHP) energy harvesting device contains no moving parts, except the pulsating movement of the working fluid, and continuously generates electrical energy from a temperature gradient. In addition, the difficulty of transforming widely available temperature gradients into continuous temperature oscillations was solved for the first time using a closed system and made available in this thesis.

Chapter 8

Conclusions and future work

A number of inventions in the field of pyroelectric energy harvesting have originated from this thesis. Sections of the here presented thesis were published in peer-reviewed international journals. With over 100 citations (October 2016) in the subject fields of engineering, applied physics, material science and environmental technology, this work significantly contributed to the field of thermal energy harvesting.

8.1 Micropattern on PVDF

In order to recover low grade thermal radiation energy and therefore reduce the primary energy source consumption, a micro-structure electrode on flexible PVDF for pyroelectric energy conversion technology was developed, characterised, experimentally verified and made available in an international journal publication. The low cost photo-lithography and wet etching process has been developed for producing meshed electrodes on free standing PVDF. This allowed the concept of a partially covered electrode to be readily upscalable and geometry independent. It has been demonstrated that the optimum electrode area coverage for harvesting is achieved by balancing the area fraction of electrically conductive aluminium required to collect the free charge to the area fraction of exposed PVDF to improve heat transfer. Compared to standard metallic electrodes, the meshing electrode coverage of 45 % provides up to 1050 % more electrical energy. The features size of 10 μm is the smallest reported on a flexible substrates suggesting further improvements for a nano-size structures. The use of a partially covered electrode on PVDF films provides scope to widen the range of potential energy harvesting applications due to the beneficial material properties of flexibility, toughness, and ease of fabrication as free-standing films. Compared to existing research conducted in this field, this approach is the first to be directly applicable to wearable devices,

novel flexible sensors, nanoscale devices and large scale pyroelectric energy harvesters due to its free-standing and cost effective nature.

8.2 Graphene-ink electrodes

When replacing conventional metallic electrodes on free standing PVDF with a graphene-ink electrode, the flexible pyroelectric device shows an considerable increase in energy density, peak power and costs. Improvements stem from the high radiation absorption of the graphene-ink as well as from the unconventional device architecture with thick graphene-ink electrodes. Due to ease of the thick electrode screen printing deposition technique, the unconventional multi-layere pyroelectric device utilises a combination pyroelectric and piezo-electric change in polarisation providing an extraordinary performance improvident.

8.3 Pyroelectric-Oscillating Heat Pipes

In the field of waste heat recovery and thermal energy harvesting, a novel type of generator technology was developed, characterised, experimentally verified and made available in an international journal publication. This work demonstrated for the first time a self-sustaining pyroelectric energy harvester utilising the natural and self-sustaining temperature fluctuation from oscillating heat pipes. Since the recovery of heat using oscillating heat pipes (OHPs) in conjunction with pyroelectric elements provides a new way of transforming thermal energy at low temperatures directly into electrical energy, the assembly was theoretically derived and experimentally demonstrated. It was also demonstrated that it is possible to exploit the rapid temperature oscillations of an OHP operating in both, steady state and unsteady modes, using a pyroelectric generator to effectively charge a storage capacitor and generate electrical energy while providing cooling. Since no external power supply is required to move the fluid in this solid state assembly, the self-sustaining system and the generated energy provides an additional and alternative power supply for the constantly growing number of electric and electronic devices. This new type of thermal generator uses lead magnesium niobate – lead titanate (PMN-PT) with a flat plate OHP and continuously generates an energy of 95 $pJcm^{-3}$ at 0.45 Hz without mechanical motion. In the chaotic mode of operation, the system effectively provides four times more electrical energy than in the steady state mode. With potential to further optimise the transformation performance, pyroelectric-oscillating heat pipe (POHP) generators provide a route to cool thermally concentrated areas while also provide electricity that is needed for monitoring and communication tasks or where wireless communication and self-sustaining applications operate remotely. Other

potential applications beyond compact cooling are standalone small-scale generators where the unexplored properties of liquid-vapour hysteresis will lead to a more efficient thermal cycling fluid. Due to the nature of the fluid flow, this is a solid-state, 'fit and forget' design with no moving mechanical parts and no need of maintenance while transforming abundantly available waste heat into electrical power.

8.4 Future work

8.4.1 Energy harvesting with PVDF

According to business technology specialists, piezo-, pyro- and thermo-electric technologies are considered early stage and slow progress [173]. For this reason, pyroelectric energy harvesting needs to be transformed into a device in a step by step strategy. From a material point of view, reduced parasitic losses, increased mechanical robustness and the ability to manufacture free standing thin films in the range of $\pm$ 1 μm are needed [174]. Based on the here presented experimental results for meshed electrodes and grapheme-ink electrodes on PVDF, continuous research on a device level needs to be conducted targeting particular heat source for thermal energy harvesting. If future work can focus on smaller partially covered electrode feature sizes for higher and faster radiation absorption, additional additional improvements in energy density, peak power and costs are expected. Further, the impact of partially covered and graphene -ink electrode for conduction and convection needs to be assessed to broaden the range of potential heat transfer improvements in other fields such as thermal imaging and thermal sensing.

8.4.2 Pyroelectric-Oscillating Heat Pipes (POHP)

The presented technology of pyroelectric-oscillating heat pipes (POHP) taps into the growing markets of thermal management and energy harvesting, where half of the primary consumed energy is wasted in form of low temperature heat [175]. These markets continue to grow as the number of interconnected devices for monitoring, computation, communication and maintenance, known as 'the internet of the things', and the growing number of untapped heat sources. One source of waste heat is the thermal management of consumer and industrial computer industry, which is expected to grow from \$ 65m to over \$ 142m over the next 10 years [176]. According to IDTechEX, energy harvesting was a \$ 0.7 billion market in 2012 and is expected to exceed \$5 billion by 2022; by then 250 million sensors will be powered by energy harvesting. This additional electrical energy provided by the POHP provides battery-less electronics and extended battery life, reduced base load demand, reduced landfill

and reduced peak power demand since most heat is dissipated when electronics operate at full range, and cost savings for peak load infrastructure. Using a PHOP device the ubiquitous noise levels associated with conventional forced convective blower fans and fluid pumps can be eliminated together with parasitic electrical losses using a self-arranged fluid flow while reducing the thermal pollution. With pyroelectric-oscillating heat pipes the capability to convert small quantities of thermal energy into more desirable electricity in the nW to mW range and provides an alternative to currently used batteries or centralised energy generation.

Chapter 9

References

[1] Wuester, H., Ferroukhi, R., El-Katiri, L., Saygin, D., Rinke, T., and Nagpal, D.; (2015). REthinking Energy 2015, Intenational Renewable Energy Agency.

[2] World Resources Institute; 2015. CAIT Climate Data Explorer, Washington, DC: http://cait.wri.org. (Accessed: 13.07.2016).

[3] Lang, S.B.; 2005. Pyroelectricity: from ancient curiosity to modern imaging tool. Physics Today, 58(8), pp.31-36.

[4] Chansin, G.; 2015. Printed and Flexible Sensors 2015 - 2015: Technologies, Players, Forecasts. IDTechEx: http://idtechex.com. (Accessed: 13.07.2016).

[5] Ling Bing, K., Li, T., Hng, H.H., Boey, F., Zhang, T., Li, S.; (2015) Waste Energy Harvesting, Springer Science and Business Media

[6] Somov and Giaffreda; 2015. Powering IoT Devices: Technologies and Opportunities, http://iot.ieee.org/. (Accessed: 13.07.2016).

[7] Johansson, M.T. and Söderström, M., 2014. Electricity generation from low-temperature industrial excess heat—an opportunity for the steel industry. Energy Efficiency, 7(2), pp.203-215.

[8] Spreemann, D. and Manoli, Y., 2012. Electromagnetic vibration energy harvesting devices: Architectures, design, modeling and optimization (Vol. 35). Springer Science and Business Media.

[9] Erturk, A. and Inman, D.J., 2011. Piezoelectric energy harvesting. John Wiley and Sons.

[10] Beeby, S.P., Tudor, M.J. and White, N.M., 2006. Energy harvesting vibration sources for microsystems applications. Measurement Science and Technology, 17(12), p.R175.

[11] Zhu, G., Lin, Z.H., Jing, Q., Bai, P., Pan, C., Yang, Y., Zhou, Y. and Wang, Z.L., 2013. Toward large-scale energy harvesting by a nanoparticle-enhanced triboelectric nanogenerator. Nano Letters, 13(2), pp.847-853.

[12] Mitcheson, P.D. and Green, T.C., 2012. Maximum effectiveness of electrostatic energy harvesters when coupled to interface circuits. IEEE Transactions on Circuits and Systems I: Regular Papers, 59(12), pp.3098-3111.

[13] Dresselhaus, M.S., Chen, G., Tang, M.Y., Yang, R.G., Lee, H., Wang, D.Z., Ren, Z.F., Fleurial, J.P. and Gogna, P., 2007. New Directions for Low - Dimensional Thermoelectric Materials. Advanced Materials, 19(8), pp.1043-1053.

[14] Varona, J., Tecpoyotl-Torres, M. and Hamoui, A.A., 2007, September. Modeling of MEMS Thermal Actuation with External Heat Source. In Electronics, Robotics and Automotive Mechanics Conference, 2007. CERMA 2007 (pp. 591-596). IEEE.

[15] Benard, W.L., Kahn, H., Heuer, A.H. and Huff, M.A., 1998. Thin-film shape-memory alloy actuated micropumps. Journal of Microelectromechanical Systems, 7(2), pp.245-251.

[16] Lee, J.S. and Lucyszyn, S., 2007. Design and pressure analysis for bulk-micromachined electrothermal hydraulic microactuators using a PCM. Sensors and Actuators A: Physical, 133(2), pp.294-300.

[17] Bowen, C.R., Kim, H.A., Weaver, P.M. and Dunn, S., 2014. Piezoelectric and ferroelectric materials and structures for energy harvesting applications. Energy and Environmental Science, 7(1), pp.25-44.

[18] Yin, W.J., Yang, J.H., Kang, J., Yan, Y. and Wei, S.H., 2015. Halide perovskite materials for solar cells: a theoretical review. Journal of Materials Chemistry A, 3(17), pp.8926-8942.

[19] Butler, K.T., Frost, J.M. and Walsh, A., 2015. Ferroelectric materials for solar energy conversion: photoferroics revisited. Energy and Environmental Science, 8(3), pp.838-848.

[20] Lee, A.J. and Pask, H.M., 2014, November. Pyroelectric effects in MgO: $LiNbO_3$ and its influence on THz generation in a polariton laser. In Advanced Solid State Lasers (pp. ATh2A-8). Optical Society of America.

[21] Hagerty, J.A., Helmbrecht, F.B., McCalpin, W.H., Zane, R. and Popović, Z.B., 2004. Recycling ambient microwave energy with broad-band rectenna arrays. IEEE Transactions on Microwave Theory and Techniques, 52(3), pp.1014-1024.

[22] Falk, M., Alcalde, M., Bartlett, P.N., De Lacey, A.L., Gorton, L., Gutierrez-Sanchez, C., Haddad, R., Kilburn, J., Leech, D., Ludwig, R. and Magner, E., 2014. Self-powered wireless carbohydrate/oxygen sensitive biodevice based on radio signal transmission. PloS one, 9(10), p.e109104.

[23] Wang, R.V., Fong, D.D., Jiang, F., Highland, M.J., Fuoss, P.H., Thompson, C., Kolpak, A.M., Eastman, J.A., Streiffer, S.K., Rappe, A.M. and Stephenson, G.B., 2009. Reversible chemical switching of a ferroelectric film. Physical Review Letters, 102(4), p.047601.

[24] Sodano, H.A., Park, G. and Inman, D.J., 2004. Estimation of electric charge output for piezoelectric energy harvesting. Strain, 40(2), pp.49-58.

[25] Cuadras, A., Gasulla, M. and Ferrari, V., 2010. Thermal energy harvesting through pyroelectricity. Sensors and Actuators A: Physical, 158(1), pp.132-139.

[26] Ikeda, T., Sasaki, T. and Ichimura, K., 1993. Photochemical switching of polarization in ferroelectric liquid-crystal films. Nature.

[27] Van Aken, B.B., Palstra, T.T., Filippetti, A. and Spaldin, N.A., 2004. The origin of ferroelectricity in magnetoelectric $YMnO_3$. Nature Materials, 3(3), pp.164-170.

[28] Uchino, K., 2009. Ferroelectric Devices 2^{nd} Edition. CRC press.

[29] Moulson, A.J. and Herbert, J.M., 1990. Electroceramics Chapman and Hall. New York, 41.

[30] Nye, JF., 1984. Physical Properties of Crystals: Their Representation by Tensors and Matrices: 1^{st} (first) Edition. Oxford Science Publications

[31] Lang, S.B., 1974. Sourcebook of pyroelectricity (Vol. 2). CRC Press.

[32] Moheimani, S.R., 2003. A survey of recent innovations in vibration damping and control using shunted piezoelectric transducers. IEEE Transactions on Control Systems Technology, 11(4), pp.482-494.

[33] Whatmore, R.W., 1986. Pyroelectric devices and materials. Reports on Progress in Physics, 49(12), p.1335.

[34] Suzuki, M., 1995. Review on future ferroelectric nonvolatile memory: FeRAM-from the point of view of epitaxial oxide thin films. Journal-Ceramic Society of Japan International Edition, 103, pp.1088-1099.

[35] Lang, S. B., Das-Gupta, D. K., 2001. Pyroelectricity: Fundamentals and Application, Handbook of Advanced Electronic and Photonic Materials Devices, Vol. 4

[36] Dvey-Aharon, H. and Taylor, P.L., 1981. Thermodynamics of pyroelectricity and piezoelectricity in polymers. Ferroelectrics, 33(1), pp.103-110.

[37] Bowen, C.R., Taylor, J., Le Boulbar, E., Zabek, D. and Topolov, V.Y., 2015. A modified figure of merit for pyroelectric energy harvesting. Materials Letters, 138, pp.243-246.

[38] Bowen, C.R., Taylor, J., LeBoulbar, E., Zabek, D., Chauhan, A. and Vaish, R., 2014. Pyroelectric materials and devices for energy harvesting applications. Energy and Environmental Science, 7(12), pp.3836-3856.

[39] Putley, E.H., 1980. A method for evaluating the performance of pyroelectric detectors. Infrared Physics, 20(3), pp.139-147.

[40] Sebald, G., Lefeuvre, E. and Guyomar, D., 2008. Pyroelectric energy conversion: optimization principles. Ultrasonics, IEEE Transactions on Ferroelectrics and Frequency Control, 55(3), pp.538-551.

[41] Sebald, G., Seveyrat, L., Guyomar, D., Lebrun, L., Guiffard, B. and Pruvost, S., 2006. Electrocaloric and pyroelectric properties of 0.75 Pb ($Mg_{1/3}$ $Nb_{2/3}$) O_3-0.25 $PbTiO_3$ single crystals. Journal of Applied Physics, 100(12), p.124112.

[42] Atulasimha, J., Xie, J., Richeson, M. and Mossi, K.M., 2009, January. Pyroelectric Materials: Scaling of Output Power With Dimensions and Substrate Clamping. In ASME 2009 Conference on Smart Materials, Adaptive Structures and Intelligent Systems. American Society of Mechanical Engineers. (pp. 213-219)

[43] Warlimont, H., 2005. Ceramics. In Springer Handbook of Condensed Matter and Materials Data (pp. 431-476). Springer Berlin Heidelberg.

[44] Li, X., Lu, S.G., Chen, X.Z., Gu, H., Qian, X.S. and Zhang, Q.M., 2013. Pyroelectric and electrocaloric materials. Journal of Materials Chemistry C, 1(1), pp.23-37.

[45] Liu, S.T. and Long, D., 1978. Pyroelectric detectors and materials. Proceedings of the IEEE, 66(1), pp.14-26.

[46] Damjanovic, D., 1998. Ferroelectric, dielectric and piezoelectric properties of ferroelectric thin films and ceramics. Reports on Progress in Physics, 61(9), p.1267.

[47] Scott, J.F., Morrison, F.D., Miyake, M. and Zubko, P., 2006. Nano-ferroelectric materials and devices. Ferroelectrics, 336(1), pp.237-245.

[48] Morozovska, A.N., Eliseev, E.A., Svechnikov, G.S. and Kalinin, S.V., 2010. Pyroelectric response of ferroelectric nanowires: Size effect and electric energy harvesting. Journal of Applied Physics, 108(4), p.042009.

[49] Lam, K.H. and Chan, H.L.W., 2005. Piezoelectric and pyroelectric properties of 65PMN-35PT/P (VDF-TrFE) 0–3 composites. Composites Science and Technology, 65(7), pp.1107-1111.

[50] Yang, Y., Jung, J.H., Yun, B.K., Zhang, F., Pradel, K.C., Guo, W. and Wang, Z.L., 2012. Flexible Pyroelectric Nanogenerators using a Composite Structure of Lead-Free $KNbO_3$ Nanowires. Advanced Materials, 24(39), pp.5357-5362.

[51] Crisman, E.E., Derov, J.S., Drehman, A.J. and Gregory, O.J., 2005. Large pyroelectric response from reactively sputtered aluminum nitride thin films. Electrochemical and Solid-State Letters, 8(3), pp.H31-H32.

[52] Lang, S.B., 1966. Pyroelectric effect in bone and tendon. Nature.

[53] Lubomirsky, I. and Stafsudd, O., 2012. Invited Review Article: Practical guide for pyroelectric measurements. Review of Scientific Instruments, 83(5), p.051101.

[54] Kandilian, R., Navid, A. and Pilon, L., 2011. The pyroelectric energy harvesting capabilities of PMN–PT near the morphotropic phase boundary. Smart Materials and Structures, 20(5), p.055020.

[55] Kohli, C.H., Schmid, P.E. and Levy, F., 1998. Ferro-and pyro-electric properties of lithium tantalate ($LiTaO_3$) thin films. Journal of the Korean Physical Society, 32, pp.S1454-S1456.

[56] Lee, A.J. and Pask, H.M., 2014, November. Pyroelectric effects in MgO:$LiNbO_3$ and its influence on THz generation in a polariton laser. In Advanced Solid State Lasers (pp. ATh2A-8). Optical Society of America.

[57] Roundy, C.B. and Byer, R.L., 1973. Sensitive $LiTaO_3$ pyroelectric detector. Journal of Applied Physics, 44(2), pp.929-931.

[58] Rödel, J., Webber, K.G., Dittmer, R., Jo, W., Kimura, M. and Damjanovic, D., 2015. Transferring lead-free piezoelectric ceramics into application. Journal of the European Ceramic Society, 35(6), pp.1659-1681.

[59] Xiao, D.Q., Lin, D.M., Zhu, J.G. and Yu, P., 2006. Investigation on the design and synthesis of new systems of BNT-based lead-free piezoelectric ceramics. Journal of Electroceramics, 16(4), pp.271-275.

[60] Yusof, H.M., Najamudin, S.H., Saif, A.E.A. and Poopalan, P., 2015, March. Poling effect on microstructure properties of Barium Strontium Titanate thin films. In Biomedical Engineering (ICoBE), 2015 2nd International Conference on (pp. 1-3). IEEE.

[61] Zhang, G., Jiang, S., Zeng, Y., Zhang, Y., Zhang, Q., Yu, Y. and Wang, J., 2011. Doping and grain size effects on pyroelectric properties of $Ba_{0.7}Sr_{0.3}TiO_3$ for uncooled infrared bolometer. Physica Status Solidi (A), 208(11), pp.2699-2708.

[62] Das-gupta, D.K., 1991. Pyroelectricity in polymers. Ferroelectrics, 118(1), pp.165-189.

[63] Horiuchi, S. and Tokura, Y., 2008. Organic ferroelectrics. Nature Materials, 7(5), pp.357-366.

[64] Lovinger, A.J., 1983. Ferroelectric polymers. Science, 220(4602), pp.1115-1121.

[65] Sokhanvar, S., Dargahi, J., Najarian, S. and Arbatani, S., 2012. Piezoelectric Polymers: PVDF Fundamentals. Tactile Sensing and Displays: Haptic Feedback for Minimally Invasive Surgery and Robotics, pp.37-65.

[66] Li, X., Qian, X.S., Lu, S.G., Cheng, J., Fang, Z. and Zhang, Q.M., 2011. Tunable temperature dependence of electrocaloric effect in ferroelectric relaxor poly (vinylidene fluoride-trifluoroethylene-chlorofluoroethylene) terpolymer. Applied Physics Letters, 99(5), p.052907.

[67] Solvay; 2015.Technical Data Sheet. http://solvay.com/. (Accessed: 13.07.2016).

[68] Ibos, L., Teyssedre, G., Bernes, A. and Lacabanne, C., 1999, December. Thermal aging of pyroelectricity in PVDF and P (VDF-TrFE) copolymers. In International Conference on Dielectric and Related Phenomena'98 (pp. 29-36). International Society for Optics and Photonics.

[69] Batra, A.K., Aggarwal, M.D.; 2013. Pyroelectric Materials: Infrared Detectors, Particle Accelerators, and Energy Harvester, SPIE press book.

[70] Maiwa, H., Ishizone, Y. and Sakamoto, W., 2012, July. Thermal and vibrational energy harvesting using PZT-and BT-based ceramics. In Applications of Ferroelectrics held jointly with 2012 European Conference on the Applications of Polar Dielectrics and 2012 International Symp Piezoresponse Force Microscopy and Nanoscale Phenomena in Polar Materials (ISAF/ECAPD/PFM), 2012 Intl Symp (pp. 1-4). IEEE.

[71] Xie, J., Mane, X.P., Green, C.W., Mossi, K.M. and Leang, K.K., 2010. Performance of thin piezoelectric materials for pyroelectric energy harvesting. Journal of Intelligent Material Systems and Structures, 21(3), pp.243-249.

[72] Xie, J., Mane, P.P., Green, C.W., Mossi, K.M. and Leang, K.K., 2008, January. Energy harvesting by pyroelectric effect using PZT. In ASME 2008 Conference on Smart Materials, Adaptive Structures and Intelligent Systems (pp. 273-277). American Society of Mechanical Engineers.

[73] Yang, Y., Guo, W., Pradel, K.C., Zhu, G., Zhou, Y., Zhang, Y., Hu, Y., Lin, L. and Wang, Z.L., 2012. Pyroelectric nanogenerators for harvesting thermoelectric energy. Nano Letters, 12(6), pp.2833-2838.

[74] Yang, Y., Wang, S., Zhang, Y. and Wang, Z.L., 2012. Pyroelectric nanogenerators for driving wireless sensors. Nano Letters, 12(12), pp.6408-6413.

[75] Kouchachvili, L. and Ikura, M., 2008. Improving the efficiency of pyroelectric conversion. International Journal of Energy Research, 32(4), pp.328-335.

[76] Lefeuvre, E., Badel, A., Richard, C. and Guyomar, D., 2005. Piezoelectric energy harvesting device optimization by synchronous electric charge extraction. Journal of Intelligent Material Systems and Structures, 16(10), pp.865-876.

[77] Badel, A., Guyomar, D., Lefeuvre, E. and Richard, C., 2005. Efficiency enhancement of a piezoelectric energy harvesting device in pulsed operation by synchronous charge inversion. Journal of Intelligent Material Systems and Structures, 16(10), pp.889-901.

[78] Guyomar, D., Sebald, G., Lefeuvre, E. and Khodayari, A., 2008. Toward heat energy harvesting using pyroelectric material. Journal of Intelligent Material Systems and Structures.

[79] Sebald, G., Guyomar, D. and Agbossou, A., 2009. On thermoelectric and pyroelectric energy harvesting. Smart Materials and Structures, 18(12), p.125006.

[80] Pulvari, C.F. and Garcia, F.J., 1978. Conversion of solar to electrical energy utilizing the thermodielectric effect. Ferroelectrics, 22(1), pp.769-771.

[81] Drummond, J.E., Fargo, V., Ream, J., Reed, H., Briscoe, J.M. and Brown, D., 1980. Demonstration of a high power density electro-caloric heat engine. Ferroelectrics, 27(1), pp.215-218.

[82] Hunter, S. R., Lavrik, N. V., Mostafa, S., Rajic, S., and Datskos, P. G., (2012) Review of pyroelectric thermal energy harvesting and new MEMs based resonant energy conversion techniques. Proc. SPIE 8377, Energy Harvesting and Storage: Materials, Devices, and Applications III, 83770D.

[83] Guyomar, D. and Sebald, G., 2009. Pyroelectric/electrocaloric energy scanvenging and cooling capabilities in ferroelectric materials. International Journal of Applied Electromagnetics and Mechanics, 31(1), pp.41-46.

[84] Olsen, R.B., Briscoe, J.M., Bruno, D.A. and Butler, W.F., 1981. A pyroelectric energy converter which employs regeneration. Ferroelectrics, 38(1), pp.975-978.

[85] Olsen, R.B., Bruno, D.A., Briscoe, J.M. and Jacobs, E.W., 1985. Pyroelectric conversion cycle of vinylidene fluoride-trifluoroethylene copolymer. Journal of Applied Physics, 57(11), pp.5036-5042.

[86] Clingman, W.H. and Moore Jr, R.G., 1961. Application of ferroelectricity to energy conversion processes. Journal of Applied Physics, 32(4), pp.675-681.

[87] Hoh, S.R., 1963. Conversion of thermal to electrical energy with ferroelectric materials. Proceedings of the IEEE, 51(5), pp.838-845.

[88] Harb, A., 2011. Energy harvesting: State-of-the-art. Renewable Energy, 36(10), pp.2641-2654.

[89] Lingam, D., Parikh, A.R., Huang, J., Jain, A. and Minary-Jolandan, M., 2013. Nano/microscale pyroelectric energy harvesting: challenges and opportunities. International Journal of Smart and Nano Materials, 4(4), pp.229-245.

[90] Bhattacharjee, S., Batra, A.K. and Cain, J., 2010. Carbon nano-fiber reinforced cement composite for energy harvesting road. Green Streets and Highways, pp.258-271.

[91] Batra, A.K., Bhattacharjee, S., Chilvery, A.K., Aggarwal, M.D., Edwards, M.E. and Bhalla, A., 2011. Simulation of energy harvesting from roads via pyroelectricity. Journal of Photonics for Energy, 1(1), pp.014001-014001.

[92] Mohammadi, S. and Khodayari, A., 2011. Free energy harvesting from ambient temperature variations. International Journal of Mechanical and Materials Engineering, 6(2), pp.167-170.

[93] Ravindran, S.K.T., Huesgen, T., Kroener, M. and Woias, P., 2011. A self-sustaining micro thermomechanic-pyroelectric generator. Applied Physics Letters, 99(10), p.104102.

[94] Cha, G. and Ju, Y.S., 2013. Pyroelectric energy harvesting using liquid-based switchable thermal interfaces. Sensors and Actuators A: Physical, 189, pp.100-107.

[95] Mostafa, S., Lavrik, N., Bannuru, T., Rajic, S., Islam, S.K., Datskos, P.G. and Hunter, S.R., 2011. A Finite Element Model of Self-Resonating Bimorph Microcantilever for Fast Temperature Cycling in A Pyroelectric Energy Harvester. In MRS Proceedings (Vol. 1325, pp. mrss11-1325). Cambridge University Press.

[96] Hunter, S.R., Lavrik, N.V., Bannuru, T., Mostafa, S., Rajic, S. and Datskos, P.G., 2011, May. Development of MEMS based pyroelectric thermal energy harvesters. In SPIE Defense, Security, and Sensing (pp. 80350V-80350V). International Society for Optics and Photonics.

[97] Zabek, D., Taylor, J. and Bowen, C.R., 2014. Performance of thin film polyvinylidenefluoride (PVDF) for pyroelectric energy harvesting. In 2014 Joint IEEE International Symposium on the Applications of Ferroelectric, International Workshop on Acoustic Transduction Materials and Devices and Workshop on Piezoresponse Force Microscopy, ISAF/IWATMD/PFM 2014 (pp. 1-4).

[98] Cengel, Yunus A., and Michael A. Boles. Thermodynamics: an engineering approach. Edited by Mehmet Kanoglu. McGraw-Hill Education, 2015.

[99] Bejan, A.; 1993. Heat transfer. John Wiley and Sons, Inc.

[100] Van der Ziel, A., 1973. Pyroelectric response and D* of thin pyroelectric films on a substrate. Journal of Applied Physics, 44(2), pp.546-549.

[101] Bama, G.K., Devi, P.I. and Ramachandran, K., 2009. Structural and thermal properties of PVDF/PVA blends. Journal of Materials Science, 44(5), pp.1302-1307.

[102] Krishnan, S.H., Ezhilarasi, D., Uma, G. and Umapathy, M., 2014. Pyroelectric-based solar and wind energy harvesting system. IEEE Transactions on Sustainable Energy, 5(1), pp.73-81.

[103] Lee, F.Y., Navid, A. and Pilon, L., 2012. Pyroelectric waste heat energy harvesting using heat conduction. Applied Thermal Engineering, 37, pp.30-37.

[104] Olsen, R.B., Bruno, D.A. and Briscoe, J.M., 1985. Pyroelectric conversion cycles. Journal of Applied Physics, 58(12), pp.4709-4716.

[105] Olsen, R.B. and Brown, D.D., 1982. High efficieincy direct conversion of heat to electrical energy-related pyroelectric measurements. Ferroelectrics, 40(1), pp.17-27.

[106] Olsen, R.B., Bruno, D.A., Briscoe, J.M. and Dullea, J., 1984. Cascaded pyroelectric energy converter. Ferroelectrics, 59(1), pp.205-219.

[107] Vanderpool, D., Yoon, J.H. and Pilon, L., 2008. Simulations of a prototypical device using pyroelectric materials for harvesting waste heat. International Journal of Heat and Mass Transfer, 51(21), pp.5052-5062.

[108] Yu, T., Zhang, G., Yu, Y., Zeng, Y. and Jiang, S., 2015. Pyroelectric energy harvesting devices based-on Pb $[(Mn_x\ Nb_{1-x})_{1/2}\ (Mn_x\ Sb_{1-x})_{1/2}]_{\ y}\ (Zr_z\ Ti_{1-z})_{\ 1-y}\ O_3$ ceramics. Sensors and Actuators A: Physical, 223, pp.159-166.

[109] Khanbareh, H., Schelen, J.B.J., Van der Zwaag, S. and Groen, W.A., 2015. A temperature oscillation instrument to determine pyroelectric properties of materials at low frequencies: Towards elimination of lock-in methods. Review of Scientific Instruments, 86(10), p.105111.

[110] Hsiao, C.C. and Siao, A.S., 2013. Improving pyroelectric energy harvesting using a sandblast etching technique. Sensors, 13(9), pp.12113-12131.

[111] Fang, J., Frederich, H. and Pilon, L., 2010. Harvesting nanoscale thermal radiation using pyroelectric materials. Journal of Heat Transfer, 132(9), p.092701.

[112] Erturun, U., Waxman, R., Green, C., Richeson, M.L. and Mossi, K., 2010, January. Energy scavenging combining piezoelectric and pyroelectric effects. In ASME 2010 Conference on Smart Materials, Adaptive Structures and Intelligent Systems, American Society of Mechanical Engineers, pp. 53-5).

[113] Mane, P., Xie, J., Leang, K.K. and Mossi, K., 2011. Cyclic energy harvesting from pyroelectric materials. IEEE Transactions on Ultrasonics Ferroelectrics and Frequency Control, 58(1), pp.10-17.

[114] Battista, L., Mecozzi, L., Coppola, S., Vespini, V., Grilli, S. and Ferraro, P., 2014. Graphene and carbon black nano-composite polymer absorbers for a pyro-electric solar energy harvesting device based on $LiNbO_3$ crystals. Applied Energy, 136, pp.357-362.

[115] Zabek, D., Taylor, J., Boulbar, E.L. and Bowen, C.R., 2015. Micropatterning of Flexible and Free Standing Polyvinylidene Difluoride (PVDF) Films for Enhanced Pyroelectric Energy Transformation. Advanced Energy Materials, 5(8).

[116] Incropera, F. P., DeWitt, D.; 2006. Introduction to Heat Transfer. John Wiley and Sons.

[117] Yamazaki, H., Ohwaki, J., Yamada, T. and Kitayama, T., 1981. Temperature dependence of the pyroelectric response of vinylidene fluoride trifluoroethylene copolymer and the effect of its poling conditions. Applied Physics Letters, 39(9), pp.772-773.

[118] Kim, K.J. and Kim, G.B., 1993. Curie transition and piezoelectricity of the blends of a ferroelectric VDF/TrFE copolymer and PMMA. Journal of Applied Polymer Science, 47(10), pp.1781-1789.

[119] Furukawa, T., Fujino, K. and Fukada, E., 1976. Electromechanical properties in the composites of epoxy resin and PZT ceramics. Japanese Journal of Applied Physics, 15(11), p.2119.

[120] Ploss, B., Ploss, B., Shin, F.G., Chan, H.L. and Choy, C.L., 2000. Pyroelectric or piezoelectric compensated ferroelectric composites. Applied Physics Letters, 76(19), pp.2776-2778.

[121] Dietze, M., Krause, J., Solterbeck, C.H. and Es-Souni, M., 2007. Thick film polymer-ceramic composites for pyroelectric applications. Journal of Applied Physics, 101(5), p.054113.

[122] Persano, L., Dagdeviren, C., Su, Y., Zhang, Y., Girardo, S., Pisignano, D., Huang, Y. and Rogers, J.A., 2013. High performance piezoelectric devices based on aligned arrays of nanofibers of poly (vinylidenefluoride-co-trifluoroethylene). Nature Communications, 4, p.1633.

[123] Lee, J.H., Lee, K.Y., Gupta, M.K., Kim, T.Y., Lee, D.Y., Oh, J., Ryu, C., Yoo, W.J., Kang, C.Y., Yoon, S.J. and Yoo, J.B., 2014. Highly stretchable piezoelectric-pyroelectric hybrid nanogenerator. Advanced Materials, 26(5), pp.765-769.

[124] Roscow, J., Zhang, Y., Taylor, J. and Bowen, C.R., 2015. Porous ferroelectrics for energy harvesting applications. The European Physical Journal Special Topics, 224(14-15), pp.2949-2966.

[125] Nunes-Pereira, J., Ribeiro, S., Ribeiro, C., Gombek, C.J., Gama, F.M., Gomes, A.C., Patterson, D.A. and Lanceros-Mendez, S., 2015. Poly (vinylidene fluoride) and copolymers as porous membranes for tissue engineering applications. Polymer Testing, 44, pp.234-241.

[126] Suen, M.S., Lin, D.T., Hu, Y.C. and Hsieh, J.C., 2010. A numerical study of the heat transfer phenomena on ZnO pyroelectric film sensor. In Proceedings of the International MultiConference of Engineers and Computer Scientists (Vol. 3).

[127] Weng, W., Chen, P., He, S., Sun, X. and Peng, H., 2016. Smart Electronic Textiles. Angewandte Chemie International Edition.

[128] Zhu, R., Chung, C.H., Cha, K.C., Yang, W., Zheng, Y.B., Zhou, H., Song, T.B., Chen, C.C., Weiss, P.S., Li, G. and Yang, Y., 2011. Fused silver nanowires with metal oxide nanoparticles and organic polymers for highly transparent conductors. ACS Nano, 5(12), pp.9877-9882.

[129] Kim, M.S., Jo, S.E., Ahn, H.R. and Kim, Y.J., 2015. Modeling of a honeycomb-shaped pyroelectric energy harvester for human body heat harvesting. Smart Materials and Structures, 24(6), p.065032.

[130] Hsiao, C.C., Ciou, J.C., Siao, A.S. and Lee, C.Y., 2011. Temperature field analysis for PZT pyroelectric cells for thermal energy harvesting. Sensors, 11(11), pp.10458-10473.

[131] Zabek, D., Taylor, J., Bowen, CR.; (under review). Characterisation and Modelling of Meshed Electrodes on Free Standing Polyvilylidene Difluoride (PVDF) Films for Enhanced Pyroelectric Energy Harvesting, Special issue of IEEE-TUFFC.

[132] Li, L., Zhang, L., Yao, X. and Li, B., 2004. Computer simulation of temperature field of multilayer pyroelectric thin film IR detector. Ceramics International, 30(7), pp.1847-1850.

[133] Blevin, W.R. and Geist, J., 1974. Influence of black coatings on pyroelectric detectors. Applied Optics, 13(5), pp.1171-1178.

[134] Wei, C.S., Lin, Y.Y., Hu, Y.C., Wu, C.W., Shih, C.K., Huang, C.T. and Chang, S.H., 2006. Partial-electroded ZnO pyroelectric sensors for responsivity improvement. Sensors and Actuators A: Physical, 128(1), pp.18-24.

[135] Hsiao, C.C. and Yu, S.Y., 2012. Improved response of ZnO films for pyroelectric devices. Sensors, 12(12), pp.17007-17022.

[136] Hsiao, C.C., Hu, Y.C., Chang, R.C. and Chao, C.K., 2009. Residual stresses and mechanical properties of a ZnO pyroelectric sensor. Theoretical and Applied Fracture Mechanics, 52(1), pp.1-6.

[137] Norkus, V., Schulze, A., Querner, Y. and Gerlach, G., 2010. Thermal effects to enhance the responsivity of pyroelectric infrared detectors. Procedia Engineering, 5, pp.944-947.

[138] Hsiao, C.C., Huang, S.W. and Chang, R.C., 2012. Temperature field analysis for ZnO thin-film pyroelectric devices with partially covered electrode. Sensor Materials, 24, pp.421-441.

[139] Lin, D.T., Hu, Y.C. and Cheng, C.H., 2012. The optimization of the thermal response on the ZnO flexible pyroelectric film temperature sensor. IEEE Sensors Journal, 12(2), pp.397-403.

[140] Solvay, (2015). Solef and Haylar PVDF design and processing guide. solvay.com. (Accessed: 13.07.2016).

[141] Hammes, P.C.A. and Regtien, P.P.L., 1992. An integrated infrared sensor using the pyroelectric polymer PVDF. Sensors and Actuators A: Physical, 32(1), pp.396-402.

[142] Bartl, J. and Baranek, M., 2004. Emissivity of aluminium and its importance for radiometric measurement. Measurement of Physical Quantities, 4(3), pp.31-36.

[143] Hass, G. and Waylonis, J.E., 1961. Optical Constants and Reflectance and Transmittance of Evaporated Aluminum in the Visible and Ultraviolet. JOSA, 51(7), pp.719-722.

[144] PVDF Properties and Uses (2013) http://acoustics.co.uk. (Accessed: 13.07.2016).

[145] Keles, O. and Dundar, M., 2007. Aluminum foil: Its typical quality problems and their causes. Journal of Materials Processing Technology, 186(1), pp.125-137.

[146] Cardoso, V.F., Minas, G., Costa, C.M., Tavares, C.J. and Lanceros-Mendez, S., 2011. Micro and nanofilms of poly (vinylidene fluoride) with controlled thickness, morphology and electroactive crysalline phase for sensor and actuator applications. Smart Materials and Structures, 20(8), p.087002.

[147] Kubouchi, Y., Kometani, Y., Yagi, T., Masuda, T. and Nakajima, A., 1989. Structure and dielectric properties of vinylidene fluoride copolymers. Pure and Applied Chemistry, 61(1), pp.83-90.

[148] Zabek, D., Bowen, C.R. and Taylor, J., 2015, May. Electrical capacitance with meshed electrodes for piezo-and pyro-electric energy harvesting applications. In Applications of Ferroelectric, International Symposium on Integrated Functionalities and Piezoelectric Force Microscopy Workshop (ISAF/ISIF/PFM), 2015 Joint IEEE International Symposium on the (pp. 83-86). IEEE.

[149] Varadan, V.V., Roh, Y.R., Varadan, V.K. and Tancrell, R.H., 1989, October. Measurement of all the elastic and dielectric constants of poled PVDF films. In Ultrasonics Symposium, 1989. Proceedings., IEEE 1989 (pp. 727-730). IEEE.

[150] Gregorio Jr, R. and Ueno, E.M., 1999. Effect of crystalline phase, orientation and temperature on the dielectric properties of poly (vinylidene fluoride)(PVDF). Journal of Materials Science, 34(18), pp.4489-4500.

[151] Lanceros-Mendez, S., Moreira, M.V., Mano, J.F., Schmidt, V.H. and Bohannan, G., 2002. Dielectric behavior in an oriented beta-PVDF film and chain reorientation upon transverse mechanical deformation. Ferroelectrics, 273(1), pp.15-20.

[152] Zhang, Q., Agbossou, A., Feng, Z. and Cosnier, M., 2011. Solar micro-energy harvesting with pyroelectric effect and wind flow. Sensors and Actuators A: Physical, 168(2), pp.335-342.

[153] Belhora, F., Cottinet, P.J., Guyomar, D., Petit, L., Lebrun, L., Hajjaji, A., Mazroui, M.H. and Boughaleb, Y., 2013. Optimization of energy harvesting conversion using the hybridization of electrostrictive polymers and electrets. Sensors and Actuators A: Physical, 189, pp.390-398.

[154] Yu, A., Roes, I., Davies, A. and Chen, Z., 2010. Ultrathin, transparent, and flexible graphene films for supercapacitor application. Applied Physics Letters, 96(25), p.253105.

[155] Chang, H.H.S. and Huang, Z., 2008. Substantial pyroelectric effect enhancement in laminated composites. Applied Physics Letters, 92(15), p.152903.

[156] Pop, E., Varshney, V. and Roy, A.K., 2012. Thermal properties of graphene: Fundamentals and applications. MRS bulletin, 37(12), pp.1273-1281.

[157] Heckman, F.A., 1964. Microstructure of carbon black. Rubber Chemistry and Technology, 37(5), pp.1245-1298.

[158] Chang, H.H.S., Whatmore, R.W. and Huang, Z., 2009. Pyroelectric effect enhancement in laminate composites under short circuit condition. Journal of Applied Physics, 106(11), p.114110.

[159] Federal Energy Administration, 2015. Available: www.energy.gov. (Accessed: 13.07.2016).

[160] Zabek, D., Penton, J. and Reay, D., 2013. Optimization of waste heat utilization in oil field development employing a transcritical Organic Rankine Cycle (ORC) for electricity generation. Applied Thermal Engineering, 59(1), pp.363-369.

[161] Fujitsu, 2015. Fujitsu Develops Thin Cooling Devices for Compact Electronics. Available: www.fujitsu.com. (Accessed: 13.07.2016).

[162] Ma, M., 2015. Oscillating heat pipes. Springer

[163] Cha, G. and Ju, Y.S., 2013. Pyroelectric energy harvesting using liquid-based switchable thermal interfaces. Sensors and Actuators A: Physical, 189, pp.100-107.

[164] Mochizuki, M., Saito, Y., Kiyooka, F., Nguyen, T., Nguyen, T. and Wuttijumnong, V., 2007, January. Advanced micro-channel vapor chamber for cooling high power processors. In ASME 2007 InterPACK Conference collocated with the ASME/JSME 2007 Thermal Engineering Heat Transfer Summer Conference (pp. 695-702). American Society of Mechanical Engineers.

[165] Zabek, D., Taylor, J., Ayel, V., Bertin, Y., Romestant, C., and Bowen, CR., 2016. A novel pyroelectric generator utilising naturally driven temperature fluctuations from oscillating heat pipes for waste heat recovery and thermal energy harvesting. Journal of Applied Physics, 120, 024505.

[166] Lips, S., Bensalem, A., Bertin, Y., Ayel, V., Romestant, C. and Bonjour, J., 2010. Experimental evidences of distinct heat transfer regimes in pulsating heat pipes (PHP). Applied Thermal Engineering, 30(8), pp.900-907.

[167] Tong, B.Y., Wong, T.N. and Ooi, K.T., 2001. Closed-loop pulsating heat pipe. Applied thermal engineering, 21(18), pp.1845-1862.

[168] Akachi, H., Actronics Kabushiki Kaisha, 1990. Structure of a heat pipe. U.S. Patent 4,921,041.

[169] Reay, D., McGlen, R. and Kew, P., 2013. Heat pipes: theory, design and applications. Butterworth-Heinemann.

[170] Ayel, V., Araneo, L., Scalambra, A., Mameli, M., Romestant, C., Piteau, A., Marengo, M., Filippeschi, S. and Bertin, Y., 2015. Experimental study of a closed loop flat plate pulsating heat pipe under a varying gravity force. International Journal of Thermal Sciences, 96, pp.23-34.

[171] Gorski, G., Litak, G., Mosdorf, R. and Rysak, A., 2015. Two phase flow bifurcation due to turbulence: transition from slugs to bubbles. The European Physical Journal B, 88(9), pp.1-6.

[172] Hu, Y., Liu, T., Li, X. and Wang, S., 2014. Heat transfer enhancement of micro oscillating heat pipes with self-rewetting fluid. International Journal of Heat and Mass Transfer, 70, pp.496-503.

[173] IDTechEx private email from 21. Oct 2015 - 19:55

[174] Alpay, S.P., Mantese, J., Trolier-McKinstry, S., Zhang, Q. and Whatmore, R.W., 2014. Next-generation electrocaloric and pyroelectric materials for solid-state electrothermal energy interconversion. MRS Bulletin, 39(12), pp.1099-1111.

[175] Lee, F.Y., Goljahi, S., McKinley, I.M., Lynch, C.S. and Pilon, L., 2012. Pyroelectric waste heat energy harvesting using relaxor ferroelectric 8/65/35 PLZT and the Olsen cycle. Smart Materials and Structures, 21(2), p.025021.

[176] IDTechEX (2015) Thermal Interface Materials, 2015 – 2015 Status, Opportunities, Market Forecast.

[177] Chin, T.K., Lee, F.Y., McKinley, I.M., Goljahi, S., Lynch, C.S. and Pilon, L., 2012. Direct thermal to electrical energy conversion using 9.5/65/35 PLZT ceramics in the ergodic relaxor phase. IEEE Transactions on Ultrasonics Ferroelectrics and Frequency Control, 59(11), pp.2373-2385.

[178] McKinley, I.M., Kandilian, R. and Pilon, L., 2012. Waste heat energy harvesting using the Olsen cycle on 0.945 Pb $(Zn_{1/3}Nb_{2/3})$ O_3–0.055 $PbTiO_3$ single crystals. Smart Materials and Structures, 21(3), p.035015.

[179] Khodayari, A., Pruvost, S., Sebald, G., Guyomar, D. and Mohammadi, S., 2009. Nonlinear pyroelectric energy harvesting from relaxor single crystals. IEEE Transactions in Ultrasonics Ferroelectrics and Frequency Control, 56(4), pp.693-699.

[180] Cha, G., Jia, Y. and Ju, Y.S., 2012, January. High-power density pyroelectric energy harvesters incorporating switchable liquid-based thermal interfaces. In Micro Electro Mechanical Systems (MEMS), 2012 IEEE 25th International Conference on (pp. 1241-1244). IEEE.

[181] Sebald, G., Pruvost, S. and Guyomar, D., 2007. Energy harvesting based on Ericsson pyroelectric cycles in a relaxor ferroelectric ceramic. Smart Materials and Structures, 17(1), p.015012.

[182] Olsen, R.B. and Evans, D., 1983. Pyroelectric energy conversion: hysteresis loss and temperature sensitivity of a ferroelectric material. Journal of Applied Physics, 54(10), pp.5941-5944.

[183] Navid, A., Vanderpool, D., Bah, A. and Pilon, L., 2010. Towards optimization of a pyroelectric energy converter for harvesting waste heat. International Journal of Heat and Mass Transfer, 53(19), pp.4060-4070.

[184] Olsen, R.B., 1982. Ferroelectric conversion of heat to electrical Energy: A demonstration. Journal of Energy, 6(2), pp.91-95.

[185] Nguyen, H., Navid, A. and Pilon, L., 2010. Pyroelectric energy converter using co-polymer P (VDF-TrFE) and Olsen cycle for waste heat energy harvesting. Applied Thermal Engineering, 30(14), pp.2127-2137.

[186] Yu, P., Tang, Y. and Luo, H., 2010. Fabrication, property and application of novel pyroelectric single crystals—PMN–PT. Journal of Electroceramics, 24(1), pp.1-4.

[187] Peng, C., Li, J.F. and Gong, W., 2005. Preparation and properties of ($Bi_{1/2}$ $Na_{1/2}$) TiO_3–Ba (Ti, Zr) O_3 lead-free piezoelectric ceramics. Materials Letters, 59(12), pp.1576-1580.

[188] Lukasiewicz, T., Swirkowicz, M.A., Dec, J., Hofman, W. and Szyrski, W., 2008. Strontium–barium niobate single crystals, growth and ferroelectric properties. Journal of Crystal Growth, 310(7), pp.1464-1469.

[189] Webster, J.G. and Eren, H. eds., 2014. Measurement, Instrumentation, and Sensors Handbook: Spatial, Mechanical, Thermal, and Radiation Measurement (Vol. 1). CRC press.

[190] Sun, R., Wang, J., Wang, F., Feng, T., Li, Y., Chi, Z., Zhao, X. and Luo, H., 2014. Pyroelectric properties of Mn-doped 94.6 $Na_{1/2}Bi_{1/2}TiO_3$-5.4 $BaTiO_3$ lead-free single crystals. Journal of Applied Physics, 115(7), p.074101.

[191] Zhang, J., Dong, X., Cao, F., Guo, S. and Wang, G., 2013. Enhanced pyroelectric properties of Cax ($Sr_{0.5}$ $Ba_{0.5}$) $_{1-x}Nb_2O_6$ lead-free ceramics. Applied Physics Letters, 102(10), p.102908.

[192] Lang, S.B. and Muensit, S., 2006. Review of some lesser-known applications of piezoelectric and pyroelectric polymers. Applied Physics A, 85(2), pp.125-134.

[193] Lau, S.T., Cheng, C.H., Choy, S.H., Lin, D., Kwok, K.W. and Chan, H.L., 2008. Lead-free ceramics for pyroelectric applications. Journal of Applied Physics.

[194] Borisenok, V.A., Koshelev, A.S. and Novitsky, E.Z., 1996. Pyroelectric materials for converters of pulsed ionizing radiation energy into electric power. Bulletin of the Russian Academy of Sciences-Physics, 60(10), pp.1660-1662.

[194] Esayan, S., Scheinbeim, J.I. and Newman, B.A., 1995. Pyroelectricity in Nylon 7 and Nylon 11 ferroelectric polymers. Applied Physics Letters, 67(5), pp.623-625.

Appendix A

Author's complete list of communications

A.1 Patent

1. **Zabek, D.**, Bowen, CR., Ayel, V., Romestant, C., Bertin, Y.; (2016) *Apparatus and Method for Generating Electrical Energy*, UK Patent Application: GB1603373.

A.2 Peer-reviewed international journal articles

8. **Zabek, D.**, Seunarine, K., Spacie, C., Bowen, CR.; (writing) *Pyroelectric Graphene-Ink Laminate Structures on Polyvinylidene Difluoride (PVDF) for Thermal Energy Harvesting and Waste Heat Recovery*, ACS Materials and Interfaces. **IF: 7.1**.

7. Xie, M., **Zabek, D.**, Bowen, CR., Abdelmageed, M., Arafa , M.; (2016) *Wind-Driven Pyroelectric Energy Harvesting Device*, Smart Materials and Structures. In Press. **IF: 2.5**.

6. **Zabek, D.**, Taylor, J., Ayel, V., Bertin, Y., Romestant, C., Bowen, CR.; (2016) *A novel pyroelectric generator utilising naturally driven temperature fluctuation from oscillating heatr pipes*, Journal of Applied Physics. 120(2), p.024505. **IF: 2.2**.

5. **Zabek, D.**, Taylor, J., Bowen, CR.; (2016) *Characterisation and Modelling of Meshed Electrodes on Free Standing Polyvilylidene Difluoride (PVDF) Films for Enhanced Pyroelectric Energy Harvesting*, IEEE Transactions on Ultrasonics, Ferroelectrics, and Frequency Control. 63(10), p.1681. **IF: 1.5, (INVITED)**.

4. **Zabek, D.**, Taylor, J., Le Boulbar, E., Bowen, CR.; (2015) *Micro-patterning of flexible and free standing polyvilylidenfluirode (PVDF) films for enhanced pyroelectric energy transformation*, Advanced Energy Materials. 5(8). pp. 1-6. **IF: 16.1**.

3. Bowen, CR., Taylor, J., Le Boulbar, E., **Zabek, D.**, Topolov, V. Yu.; (2014) *A modified figure of merit for pyrlelectric energy harvesting,*, Material Letters. Materials Letters, 138, pp.243-246. **IF: 2.5**.

2. Bowen, CR., Taylor, J., Le Boulbar, E., **Zabek, D.**, Chauhan, A., Vaish, R.; (2014) *Pyroelectric materials and devices for energy harvesting applications*, Energy and Environmental Science. 7(12), pp.3836-3856. **IF: 20.5**.

1. **Zabek, D.**, Penton, J. and Reay, D., 2013. Optimization of waste heat utilization in oil field development employing a transcritical Organic Rankine Cycle (ORC) for electricity generation. Applied Thermal Engineering, 59(1), pp.363-369. **IF: 2.7**.

A.3 Conference proceedings

2. **Zabek, D.**, Taylor, J., Bowen, CR.; (2015) *Electrical capacitance with meshed electrodes for piezo- and pyro-electric enegry harvesting applications*, In 2015 Joint IEEE International Symposium on the Applications of Ferroelectric (ISAF), International Symposium on Integrated Functionalities (ISIF), and Piezoelectric Force Microscopy Workshop (PFM), IEEE. pp. 83-86. Singapore.

1. **Zabek, D.**, Taylor, J., Bowen, CR.; (2014) *Performance of thin film Polyvylilidenfluorid (PVDF) for pyroelectric energy harvesting*, Joint IEEE International Symposium on the Applications of Ferroelectric, International Workshop on Acoustic Transduction Materials and Devices and Workshop on Piezoresponse Force Microscopy, ISAF/IWATMD/PFM. pp. 1-4. Pennsylvania State University.

Appendix B

Manufacturing of meshed electrodes on PVDF

B.1 Recipe for meshed electrodes on PVDF

Recipe for a pattern Al electrode on a flexible 52 micron pyroelectric PVDF film with wet etching:

SPINNER
1. Attach PVDF to a glass substrate.
2. Cover with liquid positive photo resist (Microchemicals – AS1512HS).
3. Spin for 30 sec. at 3000 min^{-1} (recipe 1) (1.2 μm).
4. Annealing on hot plate for 45 min at 55 C (soft bake) for polymerisation.

LASER WRITER
5. Expose sample with 15 mW , 30 % and filter ON, Energy factor 1x1.

PATTERN
6. Develop in solution the exposed photoresist for 20 to 30 sec. (AZ developer).
7. Wash off with DI water.
8. Blow dry with nitrogen.

POSTBAKE
9. Hard bake the photoresists at 55 C for 30 min.

ETCHING
10. Etch in H3PO4:HNO3:CH3OOH:H2O (“Al wet etch 1”) for 3:20 min
11. Wash off acid with DI water for 30 sec.
12. Blow dry with nitrogen.

CLOSING PROCESS
13. Wash off the remaining photo resist in moving Acetone for 10 sec.
14. Pull the sample gently off the substrate.
15. Blow dry with nitrogen.

B.2 SEM manufactured meshed square on PVDF

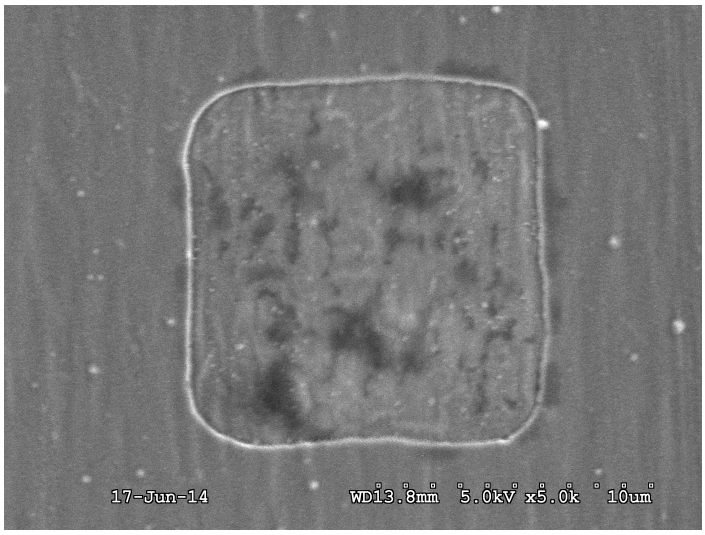

Fig. B.1 SEM x 5000 magnification of meshed square on PVDF

Appendix C

ANSYS source code

C.1 Code

```
FINISH
/CLEAR,START
/prep7
et, 1, solid227, 1001
tb, dper, 1, , , 1
tbdata,1, 11, 11, 11
tb,anel, 1, , , 1
tbdata, 1 , 3.61e-10 , 1.61e-10 , 1.42e-10
tbdata, 7 , 3.13e-10 , 1.31e-10 ,
tbdata, 12 , 1.63e-10 , ,
tbdata, 16 , 0.55e-10 , ,
tbdata, 19 , 0.55e-10 , ,
tbdata, 21 , 0.69e-10 , ,
tb,piez, 1, , , 1
tbdata, 3, 22e-12
tbdata, 6, 3e-12
tbdata, 9, -30e-12
tbdata, 14, -27e-12
tbdata, 16, -23e-12
tblist,all
BLOCK,0,100e-6,0, 100e-6,0, 52e-6
type, 1
mat, 1
vmesh, 1
da, 6, ux
da, 6, uy
da, 4, ux
```

```
da, 4, uy
da, 3, ux
da, 3, uy
da, 5, ux
da, 5, uy
da, 1, all
!da, all, symm
asel,s,area,,2
nsla,s,1
cp,next,volt,all
cm,A,node
*get,B, node, , num, min
d,B,volt,10000
allsel,all
asel,s,area,,1
nsla,s,1
cp,next,volt,all
cm,C,node
*get,D, node, , num, min
d,D,volt,0
allsel,all
/SOLU
antype, static
SOLVE
fini
/POST1
!PRRSOL,AMPS
PRRSOL,CHRG
PRNSOL,U,Z
```

C.2 Material parameter and matrix transformation

Table C.2 Piezoelectric Matrix *d*-Table For Material.

	X	Y	Z
X			0.22000E-10
Y			0.03000E-10
Z			-0.30000E-10
XY			
YZ		-0.27000E-10	
XZ	-0.23000E-10		

Table C.3 Piezoelectric stress matrix *e* computed from the piezoelectric strain matrix *d*.

	X	Y	Z
X			0.18533
Y			0.08869
Z			-0.41678
XY			
YZ		-0.49091	
XZ	-0.33333		

Table C.4 Relative permittivity at constant strain computed from piezoelectric strain and stress matrices.

	X	Y	Z
X	10.134		
Y		9.5030	
Z			9.0973